Chapter 2: Archaean metamorphic evolution of metapelites and metagreywackes of the Archaean Basement Complex in the core of the Vredefort Dome

2.1 Introduction

The Archaean Basement Complex exposed in the core of the Vredefort Dome includes numerous NW-SE trending, metapelitic, metagreywacke, metamafic and lesser meta-ironstone granulites enclosed within 3120 - 3100 Ma tonalitic and trondhjemitic gneisses (Willemse, 1937; Schreyer and Abraham, 1978; Schreyer, 1983; Stepto 1979, 1990; Stevens et al., 1997b; Gibson et al., 1998; Gibson, 2002; Perchuk et al., 2002; Lana et al., 2004; Armstrong et al., 2006). They have been interpreted as dismembered greenstone remnants (Stepto, 1990). These rocks have undergone a unique polymetamorphic history comprising three discrete events introduced in Chapter 1. A mid- to deep crustal granulite event (M_1) at 3.1 Ga has produced coarse-grained texturally well-equilibrated restitic assemblages in the metasedimentary granulites. Overprinting the coarse-grained M_1 assemblage in the Dome are shock deformation and other impact-related features formed at 2.02 Ga (M_2). Subsequent post-shock heating with decay of the shock wave, following instantaneous non-adiabatic loading of the crust, induced diffusion-controlled corona growth around M_1 garnet (M_3).

The metasedimentary granulites comprise stromatic and locally massive garnet-biotite-cordierite/orthopyroxene restites occurring as isolated, discontinuous outcrops on the farms Jagers Vrede and Steynskraal between 5 and 8 km from the centre of the Dome (the Steynskraal traverse in Figure 2.1). The Steynskraal metasedimentary granulites range from pelitic to greywacke bulk compositions (Stevens et al., 1997b, Gibson, 2002). Stromatic pelitic granulites are characterized by garnet-biotite-cordierite mesosomes alternating with thinner garnet-plagioclase-K-feldspar leucosomes (Figure 2.2a). Less aluminous and less potassic greywacke bulk compositions comprise garnet-biotite-orthopyroxene mesosomes with garnet-plagioclase leucosomes (Figure 2.2b). Less commonly, granulites appear massive, with no discrete leucosomes, and are markedly restitic. The range in textures and

bulk composition make these rocks ideal for constraining peak metamorphic conditions attained during the M_1 granulite event at an expansive scale of equilibration on the order of metres to tens of metres.

Evidence for two discrete deformation events is preserved in the Steynskraal granulites (Lana et al., 2003a). Stromatic, migmatitic layering in the granulites defines S2 and S3 fabrics (Lana et al., 2003a). S2 has been transposed by the dominant northwest-trending subvertical S3 fabric and deformed into moderately steeply NW- or SE-plunging folds (Lana et al., 2003a). Accordingly, melting must have begun during the D2 event with peak conditions attained during D3. The D2 and D3 events are intimately associated with the emplacement of distinct suites of TTGs during terrane accretion and tectonic and magmatic crustal thickening from 3100 – 3080 Ma (Armstrong et al., 2006). Recent geochronological work has yielded an Archaean age of 3.10 - 3.08 Ga for the pre-impact granulite event in the core of the Dome (Hart et al., 1999; Armstrong et al., 2006). Since the peak event occurred within only 10 – 25 Ma prior to the outpouring of the 3074 ± 6 Ma (Armstrong et al., 1991) Dominion Group lavas that unconformably overlie the Archaean Basement Complex, extremely rapid exhumation rates were invoked by Lana et al. (2006). A major problem for these authors was the anti-clockwise *P-T* path with isobaric cooling inferred by Stevens et al. (1997b) for these rocks from petrological evidence. Lana et al. (2006) proposed that rapid extensional unroofing and collapse of the thickened crust occurred during D4 at 3068 ± 6 Ma along a major subhorizontal to shallowly northwest-dipping shear zone now exposed in the southeastern core of the Dome (Broodkop shear zone, Figure 1.5; Lana et al., 2006; Armstrong et al., 2006). However, without significant overthickening of the crust implied by the isobaric cooling path of Stevens et al. (1997), rapid exhumation of the terrane through unroofing and isostatic rebound appears untenable.

In this chapter, the Steynskraal metasedimentary rocks are revisited and their pre-impact textural and mineralogical evolution modelled through a series of calculated pseudosections in THERMOCALC V3.25 (April 2007). Two metapelitic samples (SK6C and SK9-CLM) and a metagreywacke sample (SK4A), containing appropriate low-variance peak assemblages allow new peak *P-T* constraints to be estimated for the M_1 anatectic event. Pseudosections constructed for

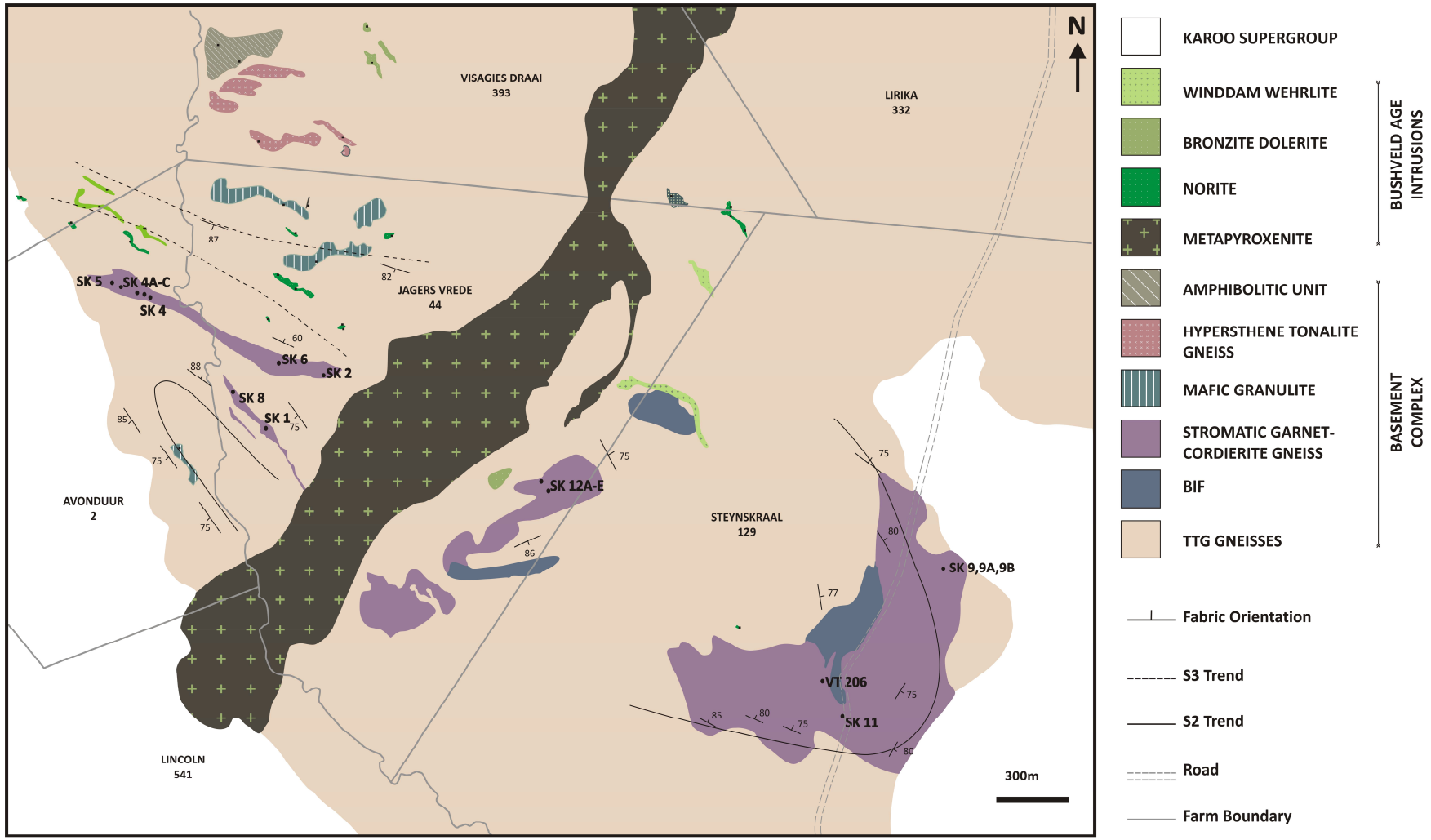

Figure 2.1: Geological map of the Jagers Vrede and Steynskraal farms, i.e., the Steynskraal traverse (modified after Stepto, 1979), showing sample localities from this study and structural data from Simpson (1977) and Lana et al. (2003a).

melt-reintegrated compositions for all samples are coupled with observed inclusion relationships in garnet to constrain the prograde *P-T* path. Published tectonic models for the evolution of the Vredefort terrane are reappraised given the new quantitative petrological constraints on peak, prograde and retrograde conditions.

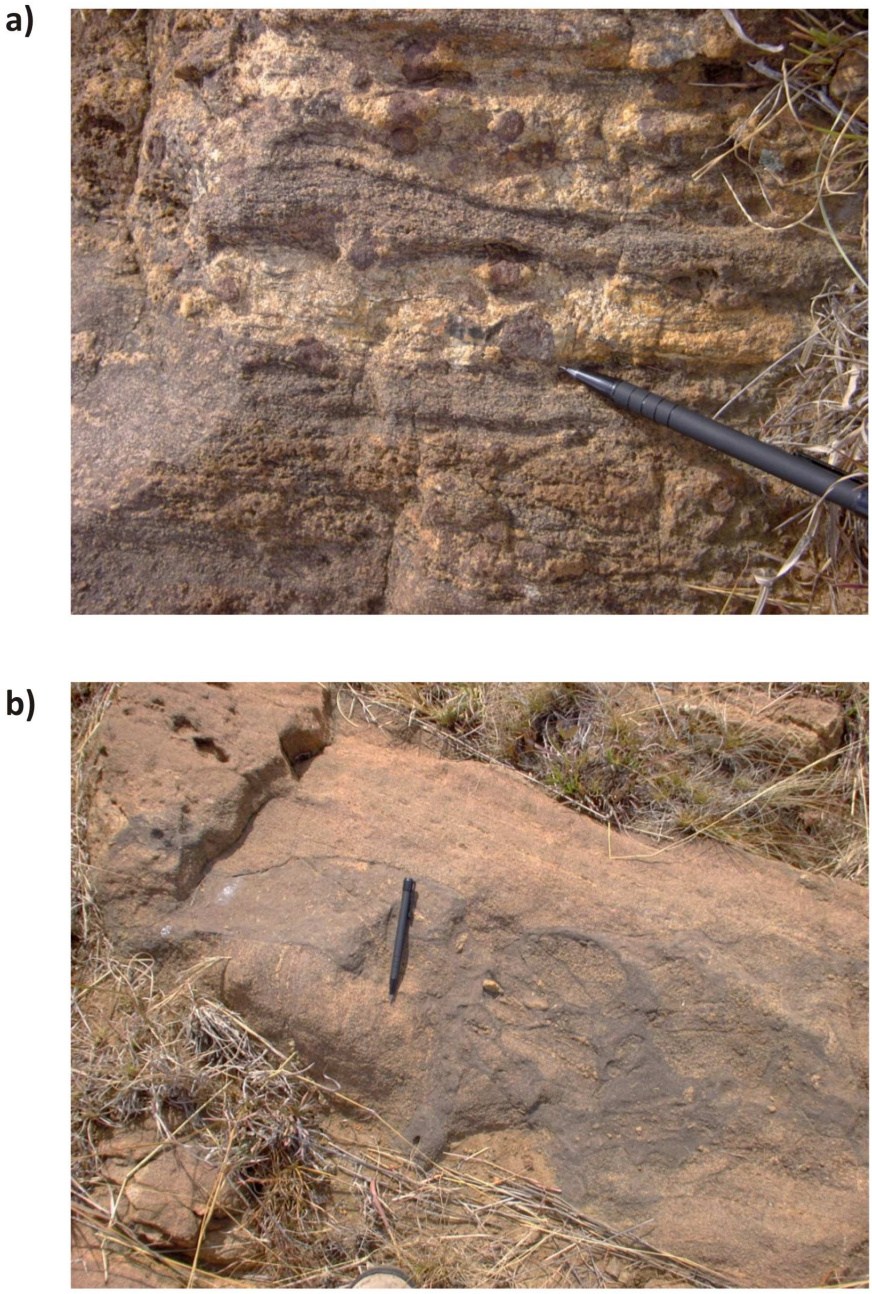

Figure 2.2: Metasedimentary garnet granulites from Steynskraal and Jagers Vrede. (a) SK6C: Stromatic metapelitic migmatite showing large garnets in the leucosome, partially replaced by a symplectite rim. (b) SK4A: Fine-grained, orthopyroxene-bearing metagreywacke cross-cut by pseudotachylitic breccia. Localities are shown in Figure 2.1.

2.2 Mesoscopic sample description

A total of 25 samples were collected across the Steynskraal traverse (Figure 2.1) encompassing both pelitic and greywacke bulk compositions. Three samples exhibiting lowest variance peak assemblages were chosen for the purpose of detailed phase equilibria modelling in this study. They include two pelitic samples (SK6C and SK9-CLM) and a metagreywacke (SK4A).

2.2.1 Metapelites (SK6C, SK9-CLM)

Metapelites may be distinguished at the mesoscopic scale from interlayered metagreywackes by the absence of orthopyroxene in the mesosomes and by the presence of cordierite-rich lamellae in more aluminous bulk compositions. Cordierite-rich lamellae are characterized by a milky-white pseudomorph enveloping included biotite. In general, the metapelites are stromatic and are characterized by garnet-cordierite-spinel-biotite-bearing mesosomes and discrete garnet-K-feldspar-plagioclase-bearing leucosomes (Figure 2.3). The terms mesosome and leucosome are used here as descriptive terms: the leucosome refers to the garnet- and feldspar-rich segregations and the mesosome refers to the cordierite-, orthopyroxene- and biotite-rich host.

SK6C

In hand specimen, SK6C is characterized by coarse (> 1.5 cm), subhedral garnet porphyroblasts in the leucosomes (Figure 2.3a, b) and finer-grained (0.1 - 1.5 cm) subhedral to anhedral garnet porphyroblasts in the mesosomes (Figure 2.3a, c). These stromatic migmatites lack melanosomes separating leucosome from mesosome. The leucosomes occur parallel to the dominant fabric, S3. Leucosomes that cross-cut the dominant layering are less common, and appear to connect the layer-parallel leucosomes, forming a network. Within the mesosomes, idioblastic faces are better preserved where garnet is adjacent to quartz or feldspar (Figure 2.3d). The greater tendency toward idioblastic boundaries where garnet is enclosed

by leucocratic phases suggests growth in the presence of a melt (Sawyer, 1999). Biotite and cordierite form distinct bands or seams in the mesosomes that appear to deflect or wrap around garnet (Figure 2.3b). Biotite associated with cordierite in the mesosomes appears to be partially replaced by a fine-grained, cream-coloured aggregate in hand specimen (Figure 2.3e).

SK9-CLM

Sample SK9-CLM is massive with no discrete leucocratic layers but rather patchy, leucocratic segregations (Figure 2.4). Coarse-grained (0.2 - 2.0 cm), inclusion-rich, subidioblastic garnet porphyroblasts are nearly entirely replaced by symplectite reaction products via a system of intersecting shock-induced fractures (Figure 2.4). Biotite-rich mantles enclose garnet and define the foliation. Locally, a fine-grained aggregate replacing biotite and, potentially, sillimanite enclosed by cordierite, is observed, identical to the one in SK6C.

2.2.2 Metagreywackes (SK4A)

The Steynskraal metagreywackes (e.g., SK4A) are typically finer-grained than the metapelites (Figure 2.5). Average garnet grain size is 0.3 cm. These rocks are stromatic with thin, diffuse, indistinct leucosomes present locally. A sub-vertical S3 fabric is defined by garnet-orthopyroxene-biotite mesosomes alternating with more feldspathic leucocratic segregations. SK4A is cut by pseudotachylitic breccias (Figures 2.2b and 2.5).

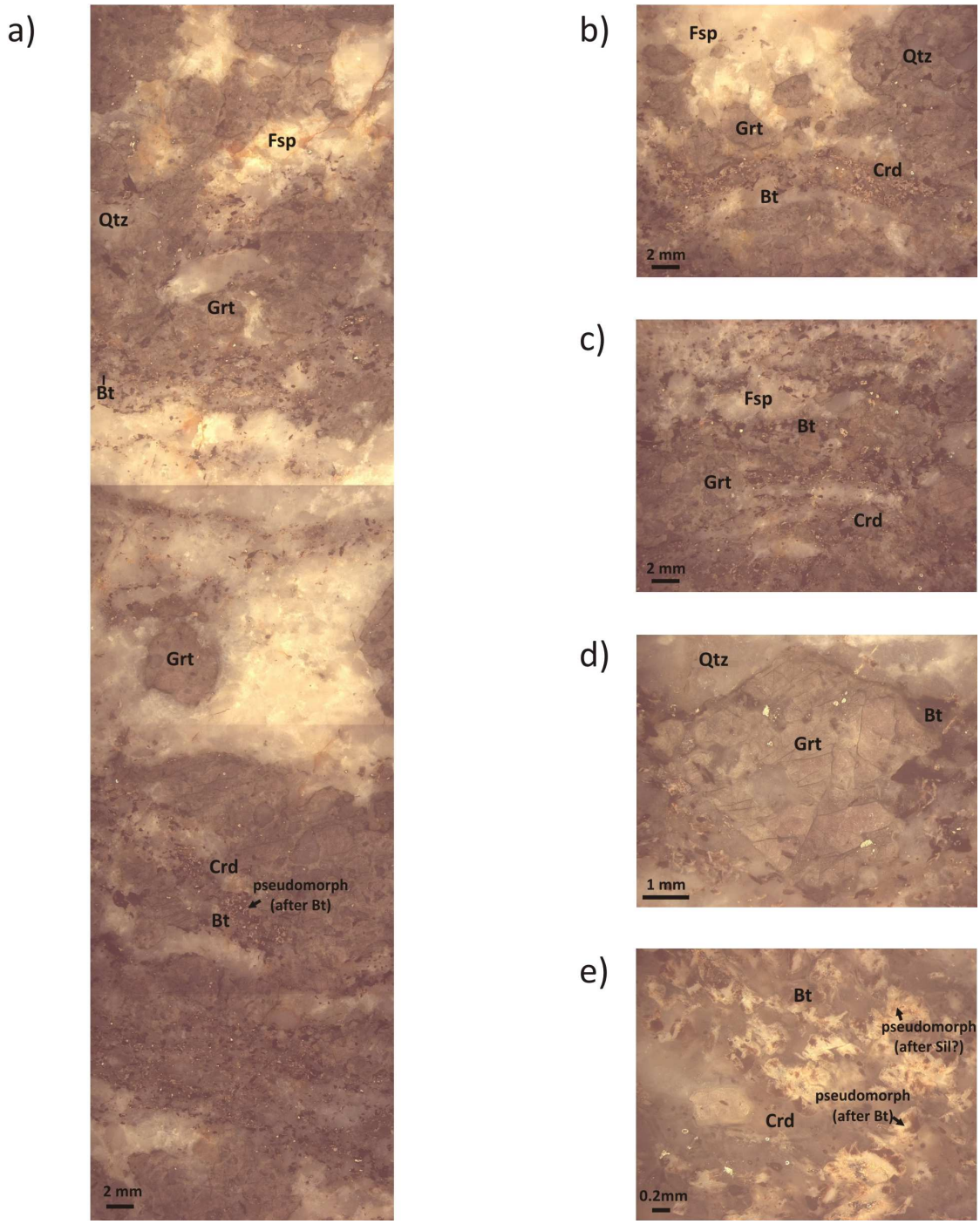

Figure 2.3: SK6C (polished hand specimen). (a) A garnet-cordierite-biotite-bearing stromatic metapelite from the farm Jagers Vrede. (b) Coarse, subhedral garnet porphyroblasts (> 1.5 cm) occur in the leucosome adjacent to finer subhedral to anhedral garnet porphyroblasts (0.1 - 1.5 cm) in the mesosome. A biotite and cordierite seam in the mesosome wraps around garnet aggregates in the mesosome. (c) Subhedral to anhedral garnet porphyroblasts (0.1 - 1.5 cm) occur in the mesosomes. (d) Garnet straddling a mesosome-leucosome boundary - garnet exhibits idioblastic boundaries adjacent to quartz and feldspar in the leucosomes. (e) A biotite and cordierite seam in the mesosome, in which biotite is partially to completely replaced by a cream-coloured, cryptocrystalline pseudomorph shown to be an intergrowth of cordierite, biotite and spinel from thin section petrographic investigation (Chapter 4).

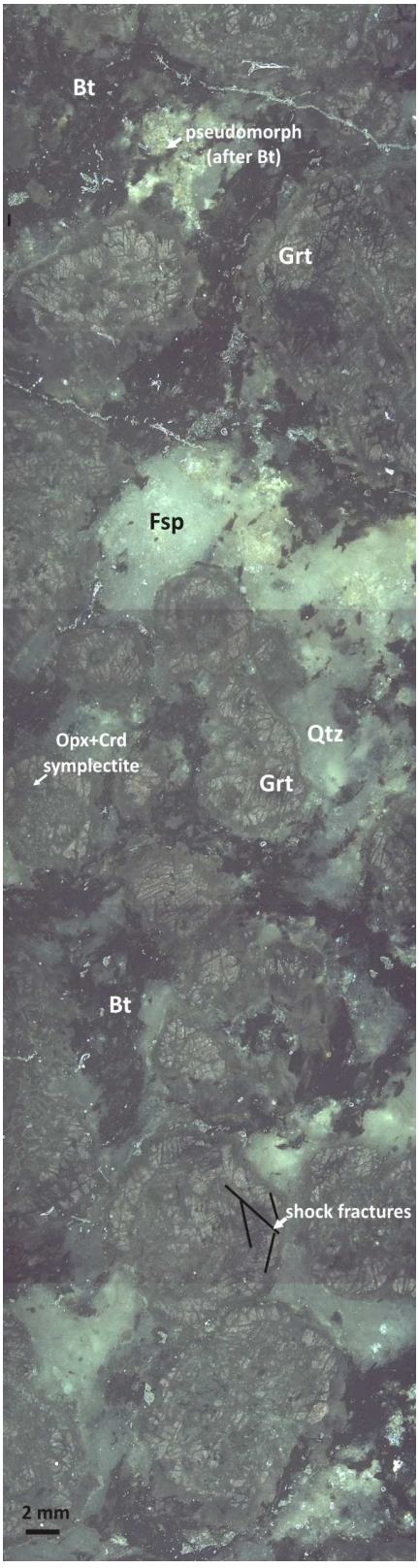

Figure 2.4: SK9-CLM. Massive garnet-cordierite-biotite-bearing metapelite from the farm Steynskraal. Leucocratic patches enclosing peritectic garnet characterise this rock, rather than the stromatic, leucocratic layers typical of SK6C. Garnets are highly fractured and almost completely replaced by a cordierite-orthopyroxene symplectite.

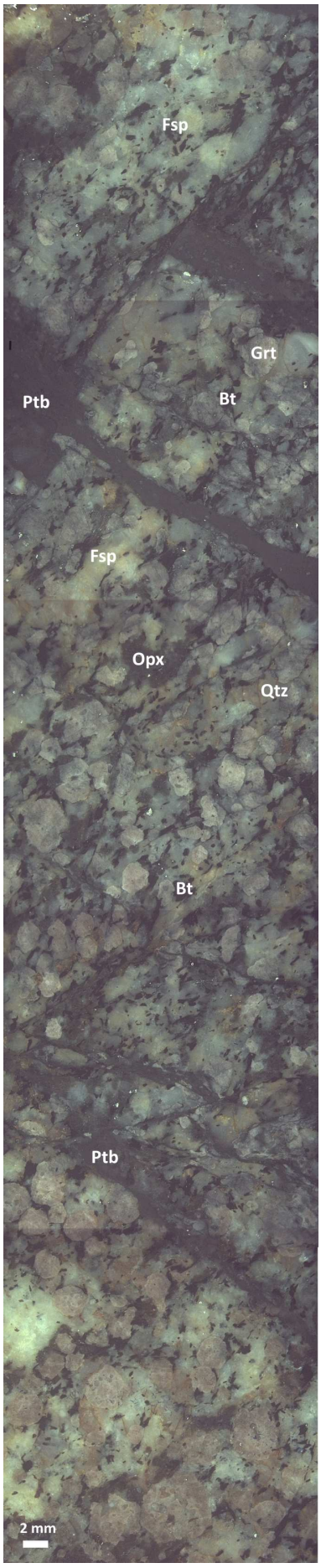

Figure 2.5: SK4A. Garnet-orthopyroxene-biotite-bearing stromatic metagreywacke from the farm Jagers Vrede. Dark-grey, cryptocrystalline pseudotachylitic breccias (Ptb) crosscut the sample forming a fine, interwoven mesh in places.

2.3 Petrography

2.3.1 Metapelites

The lowest-variance peak assemblages (garnet, cordierite, biotite, K-feldspar, plagioclase, quartz, ilmenite ± spinel ± rutile) are found in the metapelites (SK6C and SK9-CLM), making them ideal for constraining peak *P-T* regimes.

SK6C

Sample SK6C contains a medium- to coarse-grained assemblage of garnet, cordierite, spinel, biotite, plagioclase, K-feldspar, quartz, ilmenite and rutile. Garnet constitutes 25 - 35 vol%, biotite 10 - 15 vol% and cordierite < 5 vol% of the peak assemblage. The absence of magnetite and presence of rutile suggests low oxygen fugacity during peak metamorphism (White et al., 2000). Anhedral, elongate garnets in the mesosomes are mantled by biotite-cordierite-spinel seams, which define a foliation (Figure 2.6). Garnet porphyroblasts contain inclusions of quartz, biotite, sillimanite, cordierite and hercynitic spinel (within cordierite) (Figure 2.7a-d). Notably, the association of quartz and spinel as inclusions in garnet that was reported by Stevens et al. (1997b) is not observed in these samples. Planar fractures cutting garnets contain a fine-grained cordierite-orthopyroxene-spinel symplectite (Figure 2.7b). The margins of the garnets have been replaced by cordierite-orthopyroxene±spinel symplectite, grading into either plagioclase-, K-feldspar-, or biotite-dominated symplectite or blocky orthopyroxene, depending on the matrix mineral with which garnet is reacting. Corona mineralogy and textures are described more fully in Chapter 4. Where matrix biotite is included in cordierite, it is partially replaced by a pseudomorphous aggregate of orthopyroxene, biotite and cordierite (Figure 2.7e, f). In places, a monomineralic cordierite moat encloses fine-grained cordierite-spinel pseudomorphs after what appears to have been euhedral sillimanite (Figure 2.7e, f).

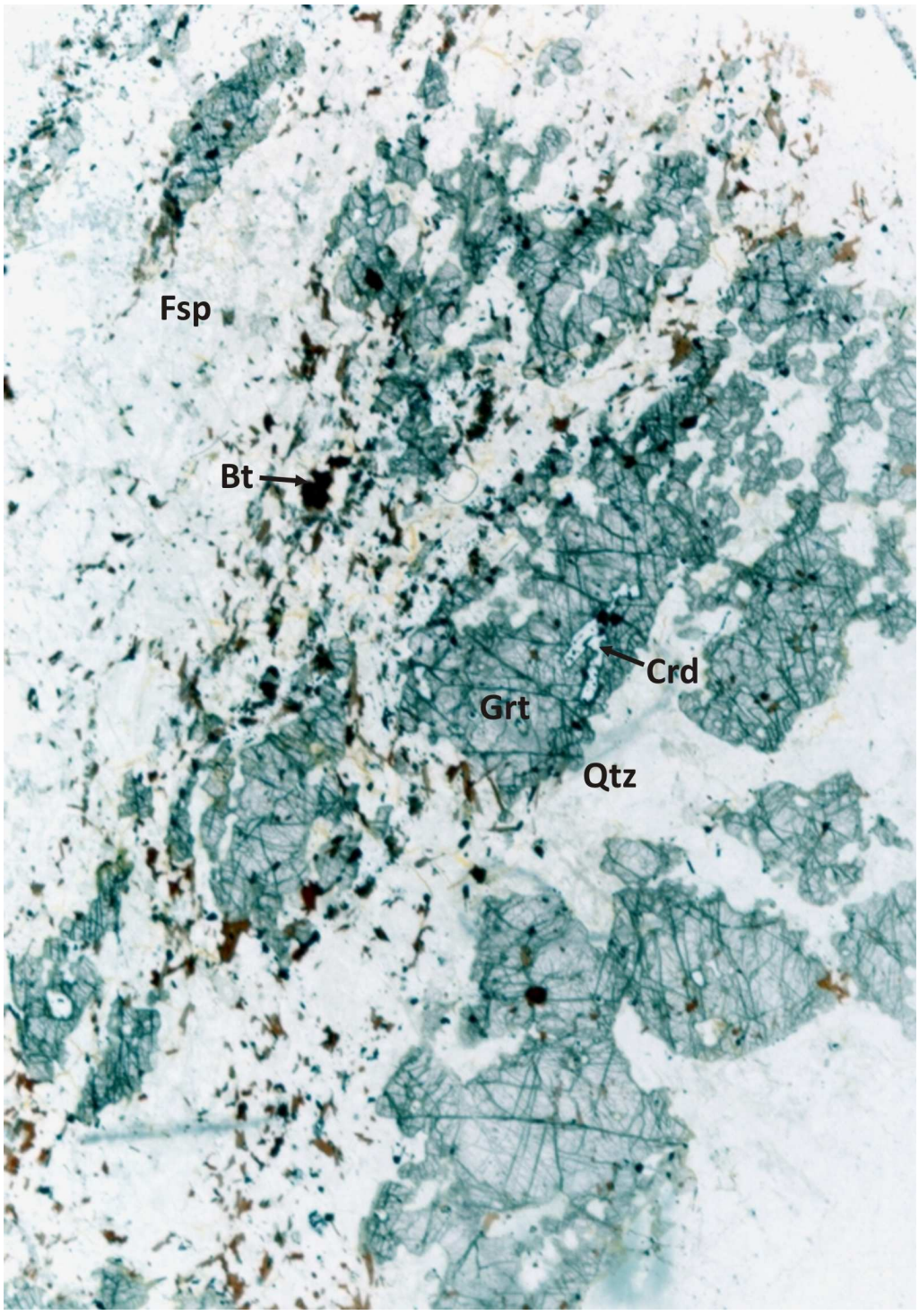

Figure 2.6: Scanned thin section from SK6C mesosome. Anhedral, inclusion-rich syntectonic garnets deflect a fabric defined by biotite-cordierite seams. Field of view is 4 cm in height.

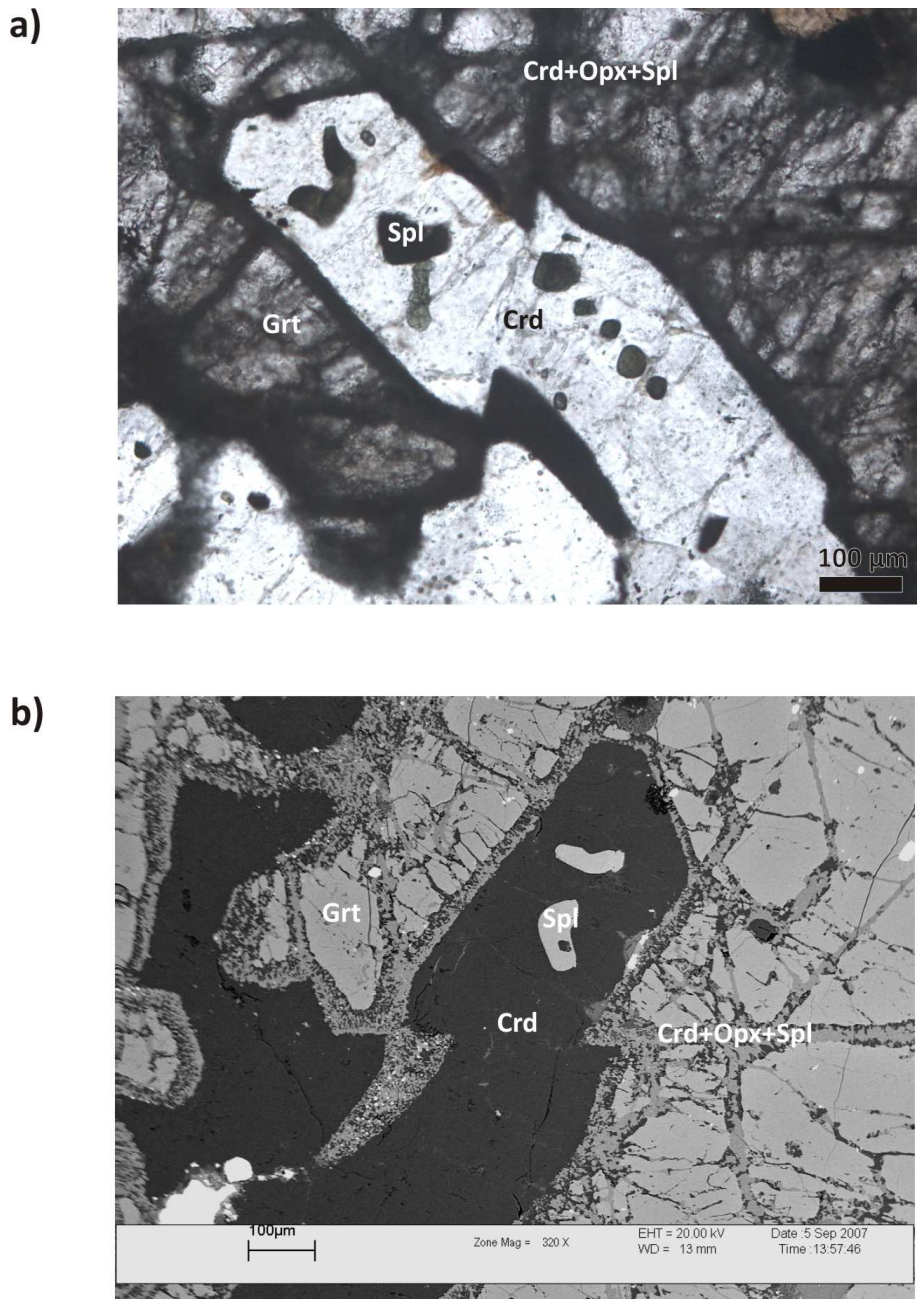

Figure 2.7: SK6C. (a) Transmitted light photomicrograph of cordierite enclosing spinel included within garnet (plane-polarised light, PPL). (b) Back-scattered scanning electron (BSE) image of a cordierite inclusion in garnet. Hercynitic spinel is in turn included within cordierite. Note the horizontal impact-induced fracture displacing garnet and cordierite in a sinistral sense, annealed by symplectite.

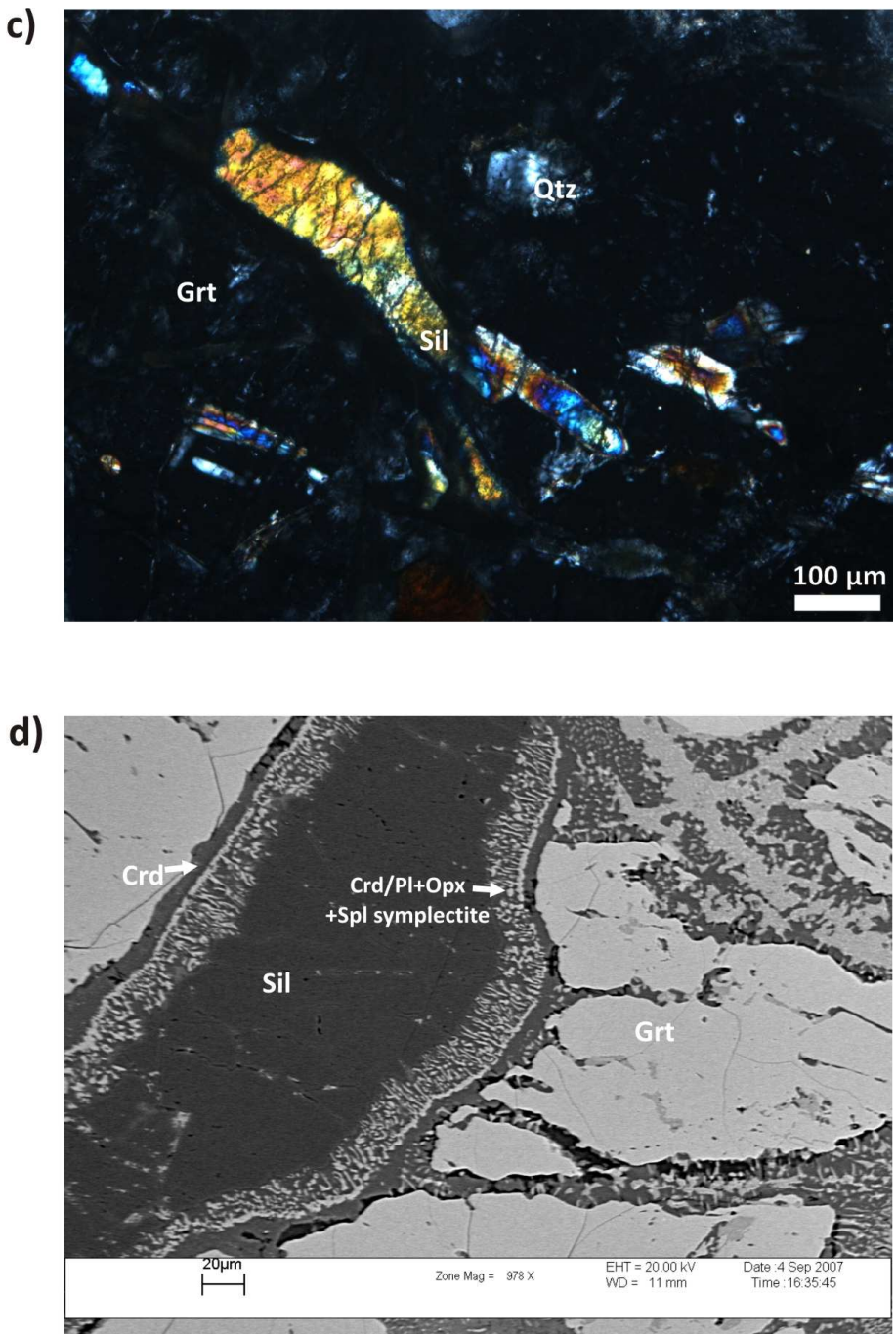

Figure 2.7 continued: SK6C. (c) Transmitted light photomicrograph of sillimanite and quartz inclusions in garnet (crossed-polarised light, CPL). (d) BSE image of a sillimanite inclusion in garnet in (c). Sillimanite has been replaced by a multi-layer corona comprising monomineralic cordierite adjacent to garnet, followed sharply by a vermicular symplectite of orthopyroxene, spinel and plagioclase adjacent to sillimanite. Garnet is replaced (top and bottom right) by cordierite-orthopyroxene-spinel symplectite.

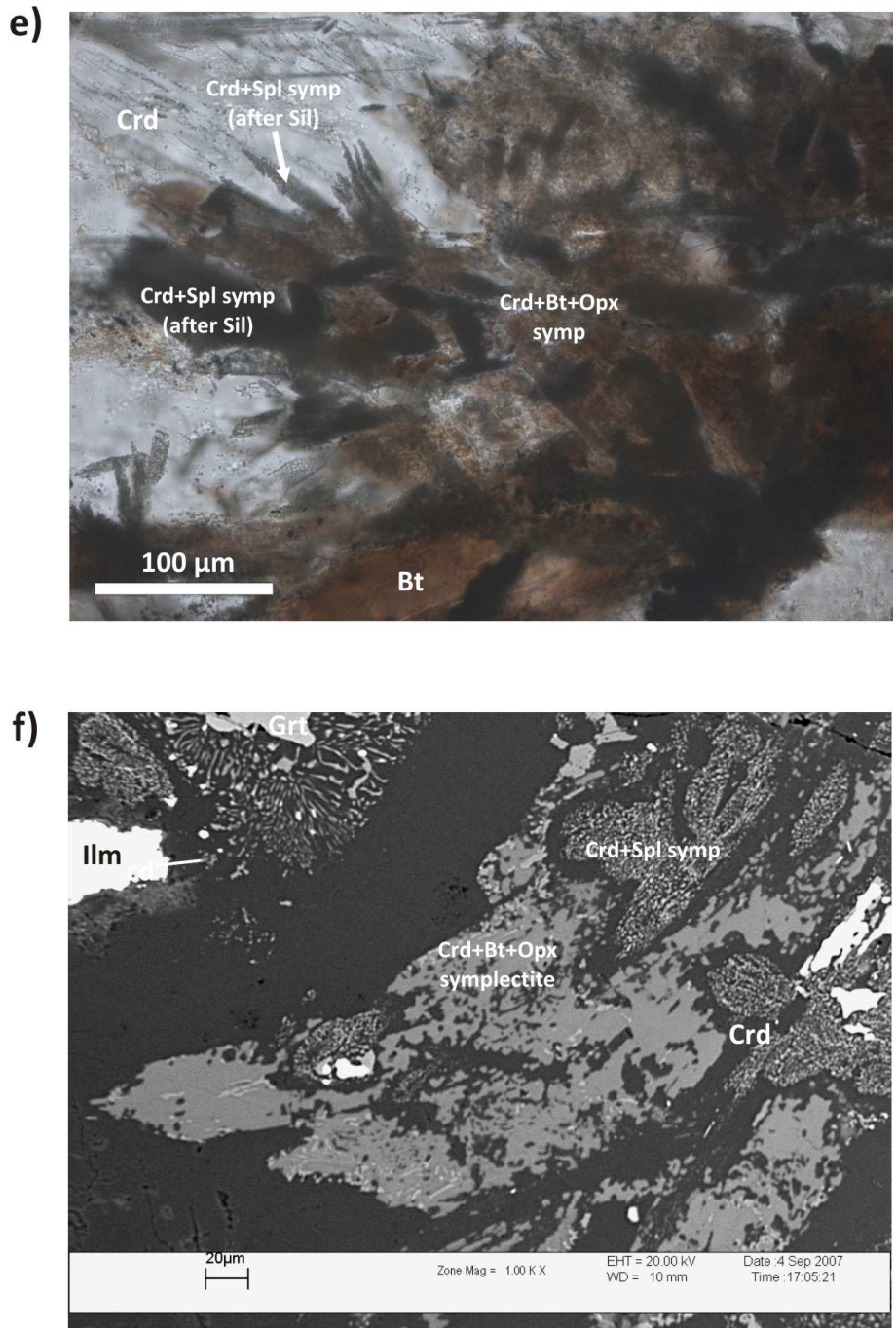

Figure 2.7 continued: SK6C. (e) Transmitted light photomicrograph of spinel-cordierite symplectite after sillimanite enclosed in peak cordierite and biotite (PPL). The latter has been partially to completely replaced by a younger generation of biotite, cordierite and orthopyroxene. (f) BSE image of the spinel-cordierite pseudomorph after sillimanite. Peak biotite has reacted with sillimanite and peak cordierite to form an intricate symplectitic intergrowth of biotite, orthopyroxene and cordierite A cordierite moat separates the biotite-rich symplectite from the cordierite-spinel symplectite after sillimanite.

SK9-CLM

Sample SK9-CLM comprises a coarse-grained, leucocratic assemblage of garnet, biotite, cordierite, plagioclase, K-feldspar, quartz, spinel and ilmenite (Figure 2.8). Subidioblastic garnet porphyroblasts occur irregularly scattered throughout the rock (Figure 2.8), in contrast to SK6C where anhedral, inclusion-rich garnets characterize the mesosome. Garnet is almost completely replaced by cordierite-orthopyroxene±spinel symplectite, grading into biotite-, K-feldspar-, plagioclase- or orthopyroxene-dominated corona layers (Figure 2.9a, b), depending on the matrix reactant mineral immediately adjacent to garnet (see Chapter 4). Relict garnet fragments are cut by shock fractures with a black trace (Figure 2.8). The black colour of the shock fracture assemblage is imparted by the presence of dark-green hercynitic spinel. Biotite is fairly common in the matrix and defines a weak foliation (S3). Garnet comprises 30 - 40 vol%, biotite 10 - 15 vol% and cordierite < 5 vol% of the SK9-CLM peak assemblage.

Garnet includes sillimanite, quartz, biotite, K-feldspar, and plagioclase. Sillimanite inclusions are completely pseudomorphed by a cordierite-spinel symplectite. Cordierite includes biotite, sillimanite (cordierite-spinel pseudomorph) and spinel. Biotite included within cordierite has been replaced by symplectitic biotite-cordierite±orthopyroxene pseudomorphs (Figure 2.9c, d). Separated from the biotite aggregates by a cordierite moat are cordierite-spinel symplectites pseudomorphing bladed sillimanite inclusions in cordierite (Figure 2.9d). A similar texture involving cordierite-spinel symplectite and an associated cordierite moat partially replacing andalusite was observed by Johnson et al. (2004) in the contact aureole of the Bushveld Complex, which they attributed to upper amphibolite facies decompression caused by rise of footwall pelites in diapiric floor structures. Locally, peak cordierite also encloses a Zn-rich (Section 2.5; Table 2.4d) spinel which is partly pseudomorphed by a younger generation of spinel + cordierite (Figure 2.9e, f).

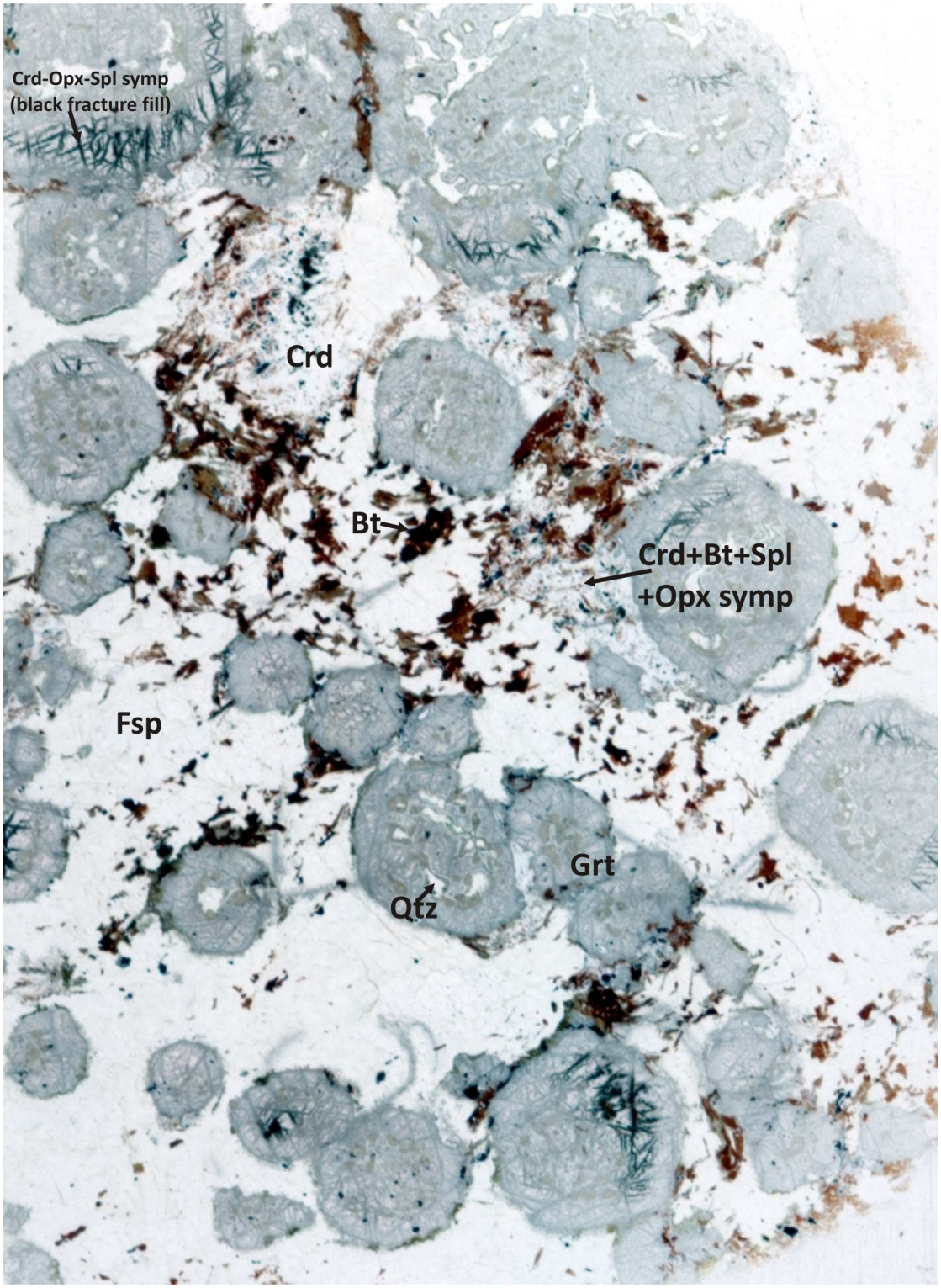

Figure 2.8: SK9-CLM scanned thin section. Idiomorphic garnet porphyroblasts (now almost entirely replaced by cordierite-orthopyroxene-spinel symplectite) are irregularly scattered throughout a matrix of plagioclase, K-feldspar, cordierite and biotite. Biotite and sillimanite enclosed in cordierite are almost entirely replaced by biotite-cordierite-spinel-orthopyroxene symplectite products. Vertical dimension 4 cm.

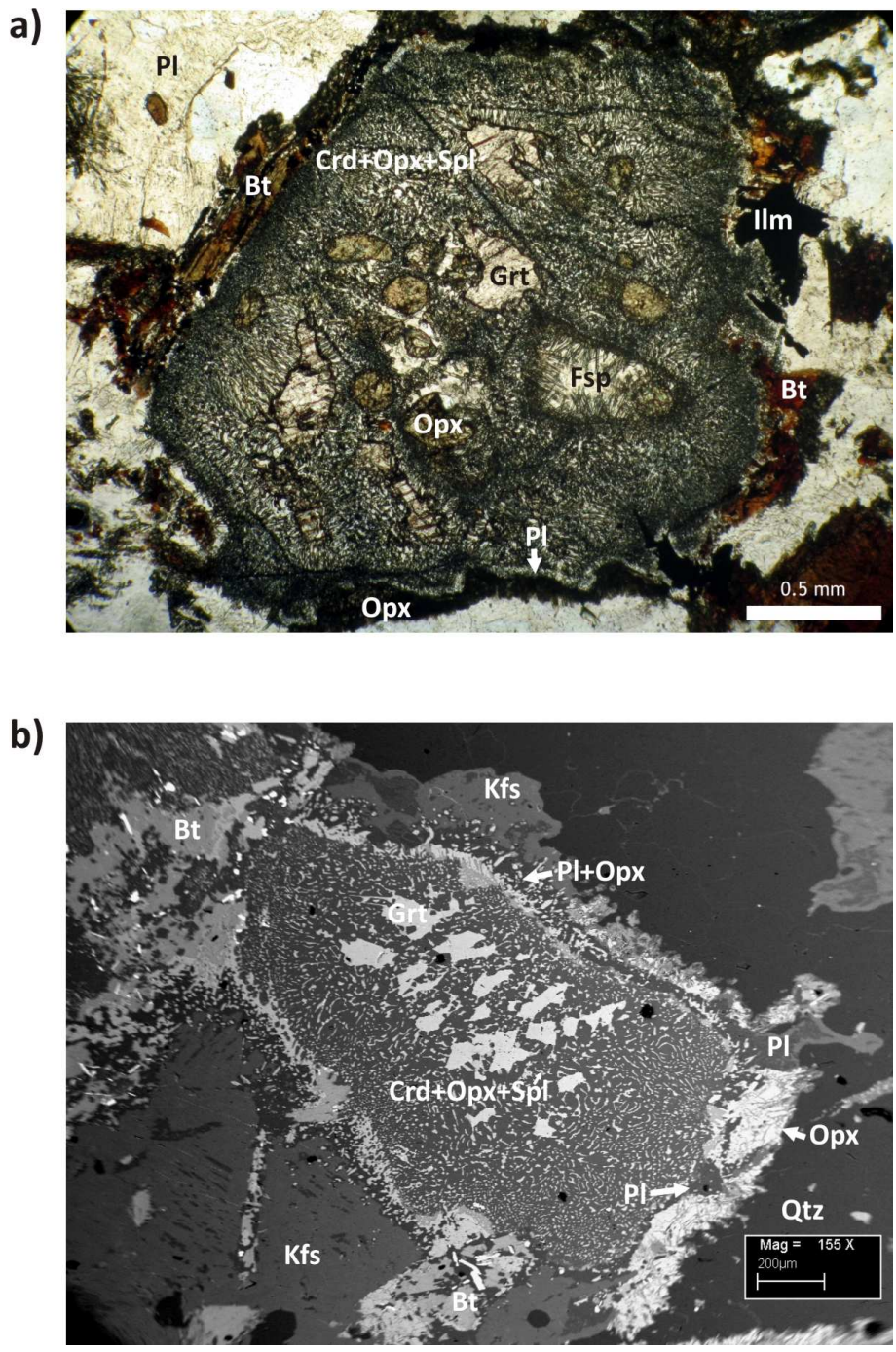

Figure 2.9: SK9-CLM. (a) Transmitted light photomicrograph of a garnet porphyroblast, now almost entirely pseudomorphed by cordierite-orthopyroxene-spinel symplectite, grading into plagioclase ± biotite ± monomineralic blocky orthopyroxene rind depending on local domainal bulk composition dictated by reactant immediately adjacent to garnet (PPL). (b) BSE image of a garnet porphyroblast enclosed by quartz, perthitic K-feldspar, and minor biotite. Garnet is almost completely replaced by cordierite-orthopyroxene-spinel symplectite. The modes and morphology of symplectite products vary depending on which matrix mineral reacted with garnet. Corona mineralogy is discussed more comprehensively in Chapter 4.

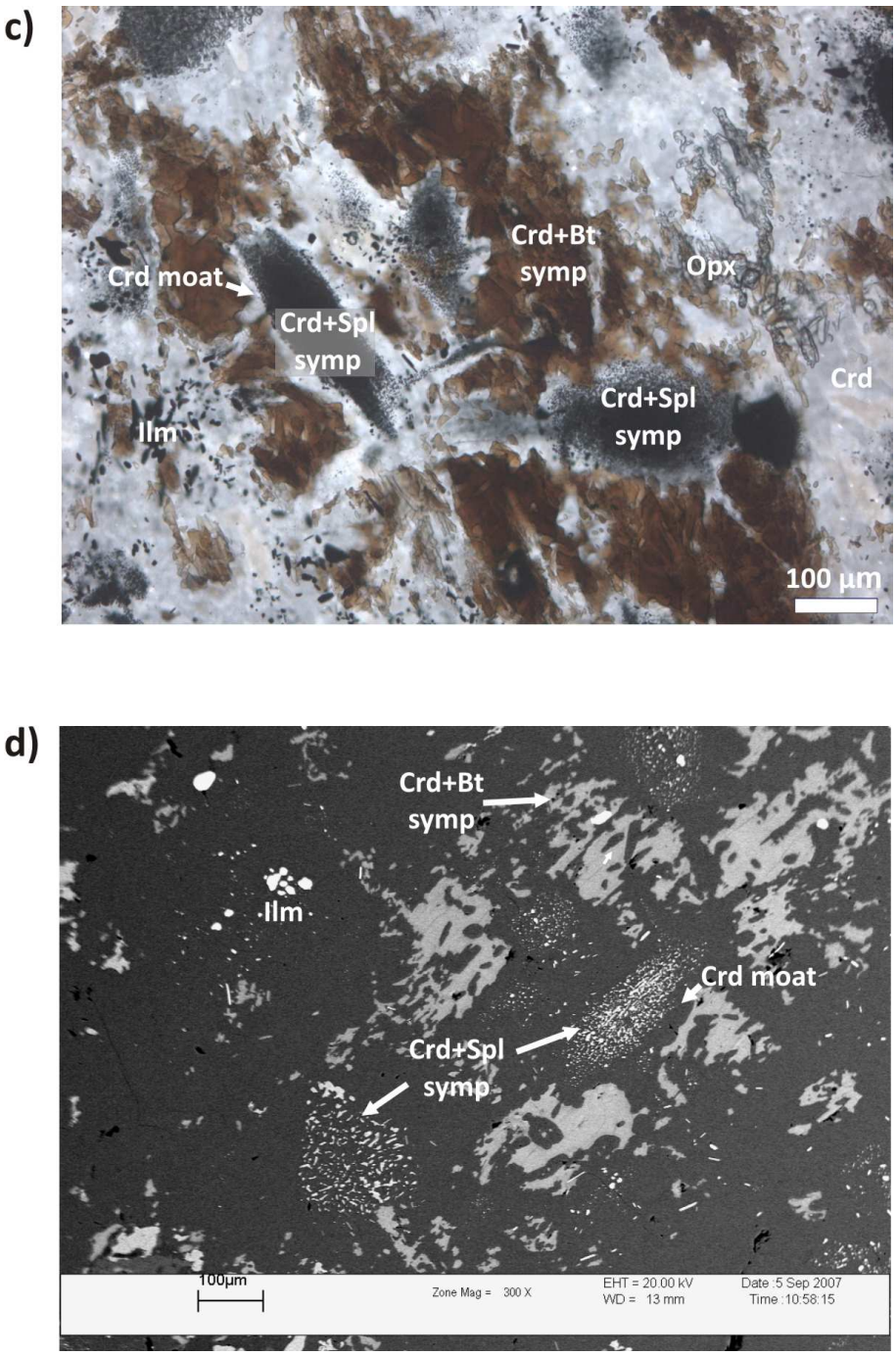

Figure 2.9 continued: SK9-CLM. (c) Transmitted light photomicrograph of symplectite development after peak sillimanite and biotite included in cordierite (PPL). Pseudomorphed sillimanite blades are characterized by a dense aggregate of spinel and cordierite enclosed by a monomineralic cordierite moat, which grades into a cordierite-orthopyroxene-biotite symplectite replacing peak biotite. (d) BSE image of cordierite-spinel symplectite after sillimanite adjacent to a cordierite-biotite symplectite after peak biotite included in cordierite, separated by a monomineralic cordierite moat.

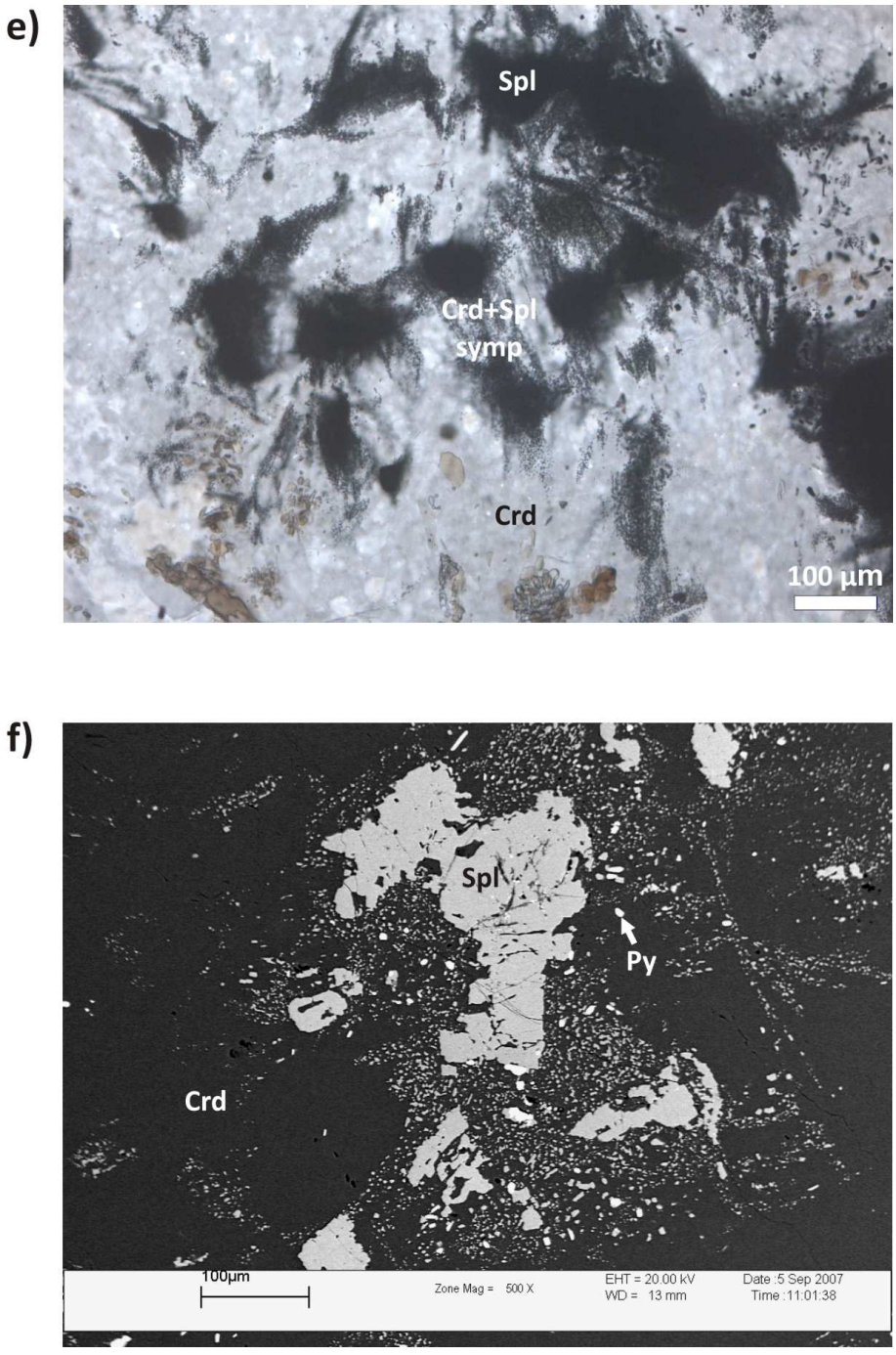

Figure 2.9 continued: SK9-CLM: (e) Transmitted light photomicrograph of spinel-cordierite-pyrite symplectite after peak spinel included in peak cordierite (PPL). (f) BSE image of spinel-cordierite-pyrite symplectite after peak spinel included within cordierite.

2.3.2 Metagreywackes

Orthopyroxene-bearing metagreywackes (SK4A) contain a fine- to medium-grained assemblage comprising garnet (20 - 30 vol %), orthopyroxene (10 - 20 vol %), biotite (5 - 10 vol %), quartz, plagioclase, K feldspar and ilmenite (Figure 2.10). An intricate pseudotachylitic breccia vein network ranging from microns to millimetres is present. The finest pseudotachylitic breccias are highly tortuous and appear preferentially developed in biotite-rich portions of the matrix adjacent to garnet (black arrows, Figure 2.10). A planar fabric is defined by leucocratic, quartzofeldspathic segregations alternating with garnet-orthopyroxene-rich mesosomes. Garnet is partially mantled by orthopyroxene (Figure 2.11a, b). Biotite, quartz, K-feldspar and plagioclase occur as inclusions in both orthopyroxene and garnet. Notably, orthopyroxene is not included in garnet. Matrix biotite occurs commonly adjacent to orthopyroxene and appears to be replacing orthopyroxene (Figure 2.11b).

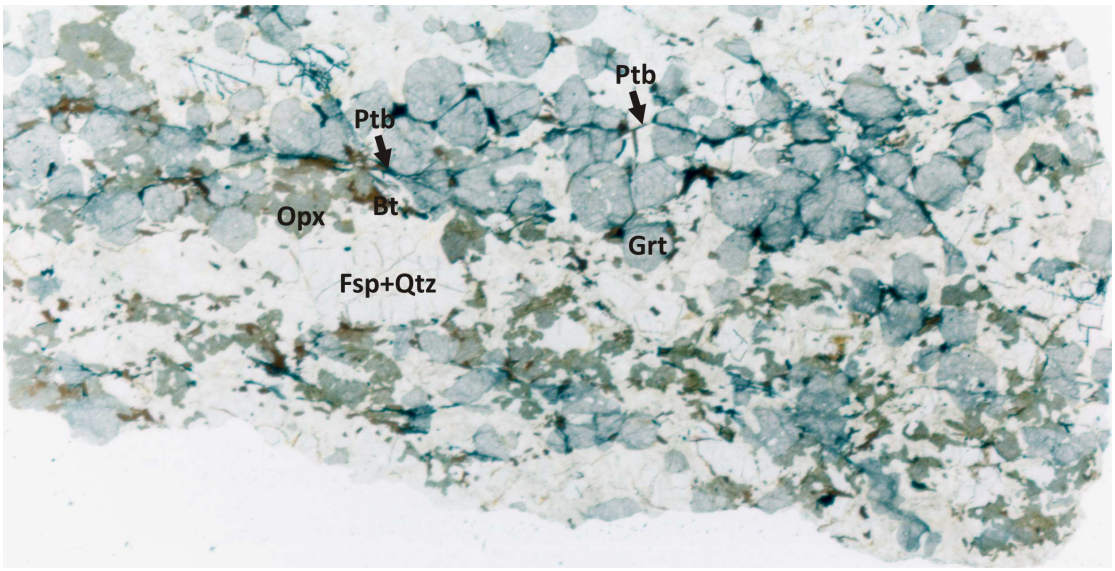

Figure 2.10: SK4A - scanned thin section (Width of field of view is 4 cm) showing garnet- and orthopyroxene-rich layers alternating with leucocratic, quartzofeldspathic layers. The pseudotachylitic breccias (Ptb) are constrained to the margins and fractures within garnet, forming a fine, anastomosing network.

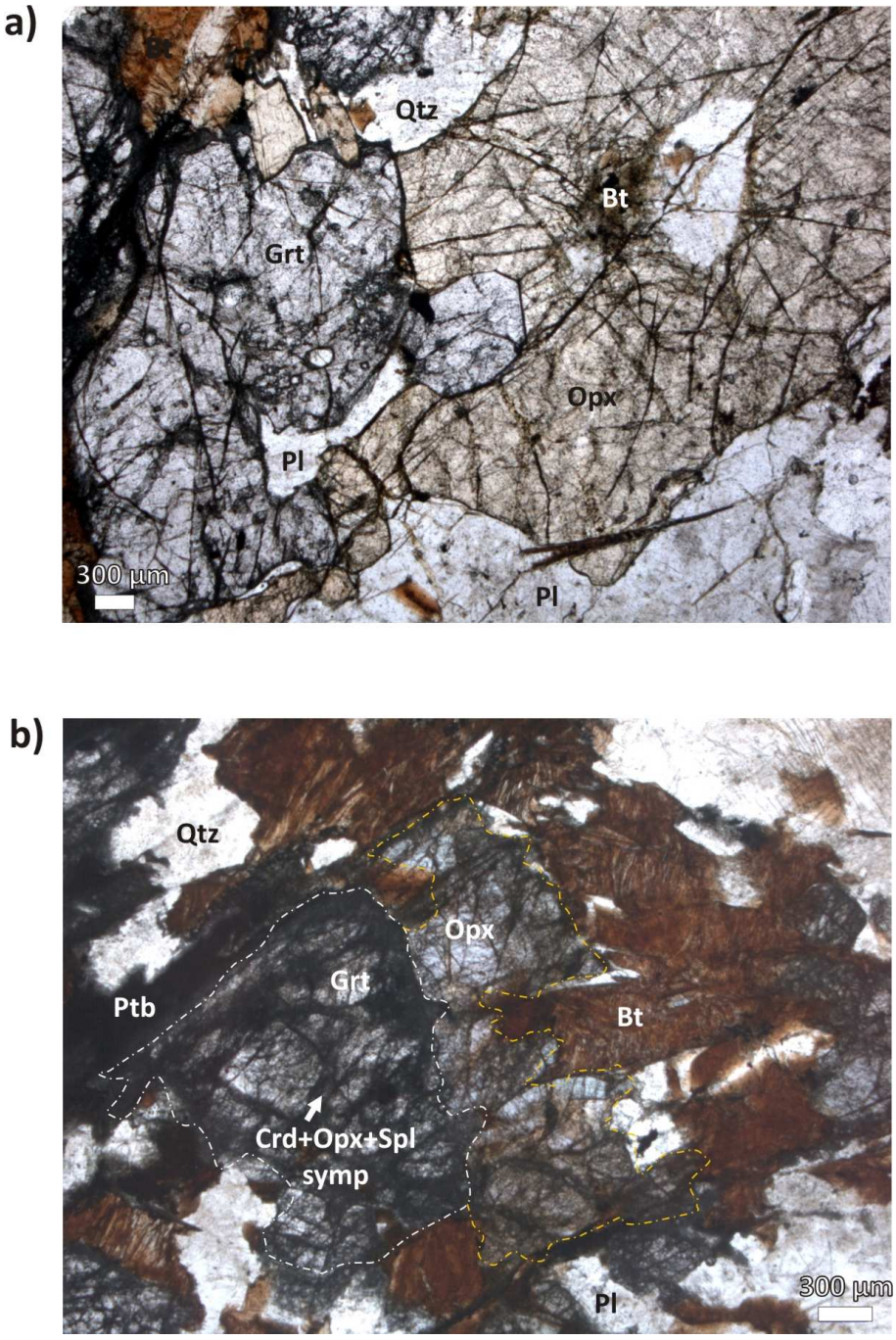

Figure 2.11: SK4A. (a) Transmitted light photomicrograph of peak orthopyroxene partially mantling garnet (PPL). Plagioclase, quartz and K-feldspar are commonly included in garnet and orthopyroxene; however orthopyroxene inclusions in garnet are conspicuously absent. (b) Transmitted light photomicrograph of peak orthopyroxene partially mantling garnet (PPL). Biotite appears to be replacing both garnet and orthopyroxene. The white border indicates the garnet grain boundary and the orange border delineates the orthopyroxene boundary. Pseudotachylitic breccia (Ptb) occurs immediately adjacent to intensely shock fractured garnet. Biotite is intensely kink-banded.

2.4 Bulk-rock compositions

Whole-rock major element compositions were determined by XRF spectrometry on a Philips 1404 Wavelength Dispersive spectrometer at the University of Stellenbosch. The spectrometer is fitted with a Rh tube and six analysing crystals, namely: LIF200, LIF220, LIF420, PE, TLAP and PX1. The detectors are a gas-flow proportional counter, scintillation detector or a combination of the two. The gas-flow proportional counter uses P10 gas, which is a mixture of 90% Argon and 10% Methane. Major elements were analysed on a fused glass bead at 50 kV and 50 mA tube operating conditions. Matrix effects in the samples were corrected for by applying theoretical alpha factors and measured line overlap factors to the raw intensities measured with the SuperQ Philips software.

Whole-rock XRF analysis was performed on 25 samples to constrain appropriate bulk compositions for phase equilibria modelling and tentative provenance determination. Compositionally and mineralogically, samples may be divided into 2 clusters, namely, orthopyroxene-bearing, subaluminous metagreywackes (Table 2.1) and more aluminous and potassic cordierite-bearing metapelites (Table 2.2). In Tables 2.1 and 2.2, X_{Mg} = molar Mg/(Fe + Mg). Figure 2.12 demonstrates compositional heterogeneity on an AFM projection from quartz, K-feldspar and plagioclase.

In Figure 2.13, FeO+MgO is plotted against $K_2O/(K_2O+Na_2O)$, facilitating comparison of samples in this study with metasediments from the Barberton Greenstone Belt (Dziggel et al., 2006), the average Archaean and Proterozoic shale (McLennan, 1982), and the average Post-Archaean shale (Taylor and McLennan, 1985). All samples in this study are more ferromagnesian than the average Archaean shale (AA), Proterozoic shale (AP), Average Post-Archaean shale (PAAS) and average greywacke and arkosic compositional fields of Chacko et al. (1992) and Pettijohn et al. (1987). Likewise, most of the Barberton greywackes reported by Dziggel et al. (2006) are less potassic and ferromagnesian than the samples from the Steynskraal traverse.

Table 2.1: XRF Bulk rock compositions: Metagreywackes (wt%)

Peak assemblage: garnet-biotite-orthopyroxene (Pl, ±Kfs, Ilm)

Sample	*SK9 (SLM)*	*SK1 (CM-SLM)*	*SK5*	*SK8F*	*SK8C*	*SK9A (SLM)*	*SK2 (i)-(2)*	*SK1F*	*SK6F-(i)*	*SK 12A*	*SK 12C PT*	*SK 12E*	*SK 9B' (3)*	*SK 4C(i) 1*	*SK 4C(i) 2*	*VT 206*	*SK 2(i) (1)*	*SK 4A ADJ*
TAG	*1*	*2*	*3*	*4*	*5*	*6*	*7*	*8*	*9*	*10*	*11*	*12*	*13*	*14*	*15*	*16*	*17*	*C*
SiO_2	59.14	60.93	58.77	57.43	60.56	62.59	56.37	58.74	59.48	54.33	57.66	57.54	61.2	58.94	59.38	54.67	57.56	58.29
TiO_2	0.77	0.58	0.64	0.64	0.7	0.71	0.66	0.61	0.69	0.71	0.65	0.72	0.59	0.68	0.68	0.56	0.77	0.72
Al_2O_3	14.04	14.57	14.06	14.58	14.42	14.17	14.38	14.07	15.42	14.3	14.44	13.96	15.4	14.12	14.19	12.58	15.59	14.49
Fe_2O_3	12.54	12.79	14.67	15.6	12.39	9.8	18.06	15.76	10.64	19.71	15.76	14.71	10.5	15.49	14.12	22.19	12.93	14.24
MnO	0.36	0.22	0.42	0.25	0.25	0.84	0.26	0.29	0.31	0.3	0.23	0.69	2.24	0.30	0.30	0.51	0.18	0.28
MgO	6.44	5.46	6.09	6.16	6.04	6.16	7.04	6.44	6.59	6.88	6.14	6.92	5.12	6.29	5.96	6.44	5.44	5.84
CaO	1.35	1.17	1.11	0.95	1.02	1.46	0.9	0.93	1.6	0.66	1.08	0.92	1.78	1.11	1.23	1.29	1.34	1.27
Na_2O	2.13	1.97	1.63	1.55	2.05	1.99	1.17	1.48	2.55	1.46	1.54	1.77	1.68	1.47	2.31	0.62	2.42	2.15
K_2O	2.12	1.58	0.85	1.18	1.41	1.7	0.62	1.08	1.42	1.08	1.03	1.08	0.78	0.56	0.84	0.3	1.94	2.08
Cr_2O_3	0.01	0.01	0.01	0.01	0.01	0.01	0.01	0.01	0.01	0.01	0.01	0.01	0.01	0.01	0.01	0.01	0.01	0.01
NiO	0.05	0.04	0.04	0.04	0.05	0.05	0.05	0.04	0.07	0.06	0.06	0.04	0.03	0.04	0.04	0.05	0.05	0.05
P_2O_5	0.08	0.07	0.07	0.07	0.06	0.07	0.06	0.08	0.09	0.07	0.06	0.06	0.11	0.06	0.07	0.28	0.07	0.07
LOI	1.44	1.45	1.46	1.47	1.41	1.37	1.34	1.42	1.48	1.32	1.39	1.41	0.3	1.49	1.47	1.38	1.51	1.43
Total	100.46	100.82	99.8	99.93	100.36	100.92	100.92	100.93	100.34	100.87	100.03	99.82	99.74	100.56	100.61	100.86	99.8	100.92
X_{Mg}	0.50	0.46	0.45	0.44	0.49	0.55	0.44	0.45	0.55	0.41	0.44	0.48	0.49	0.45	0.46	0.37	0.45	0.45

All Measure Fe is assumed to be Fe_2O_3. X_{Mg} = molar Mg/(Fe + Mg)

Table 2.2: XRF Bulk rock compositions: Metapelites (wt%)

Peak assemblage: garnet-cordierite-biotite (Pl, ±Kfs, Ilm, ±Ru)

Sample	***SK6***	***SK11***	***SK1-CA(i)***	***SK1CA(i)C***	***SK9-CLM***	***SK6C-(1)***
TAG	***18***	***19***	***20***	***21***	***A***	***B***
SiO_2	59.74	55.84	61.13	60.03	59.83	59.89
TiO_2	0.84	0.93	0.72	0.70	0.75	0.62
Al_2O_3	17.56	19.25	15.11	14.22	15.44	16.86
Fe_2O_3	8.61	8.88	10.72	12.76	11.76	9.52
MnO	0.18	0.12	0.21	0.25	0.22	0.26
MgO	6.52	6.93	5.64	6.64	6.35	5.77
CaO	1.12	1.52	1.17	0.85	0.78	1.27
Na_2O	2.00	2.41	2.37	1.63	1.41	2.25
K_2O	2.26	2.27	2.13	1.78	2.21	2.18
Cr_2O_3	0.01	0.01	0.01	0.01	0.01	0.01
NiO	0.06	0.09	0.05	0.05	0.04	0.05
P_2O_5	0.07	0.09	0.07	0.07	0.06	0.09
LOI	1.52	1.62	1.51	1.51	1.54	1.57
Total	100.48	99.95	100.84	100.48	100.4	100.36
X_{Mg}	0.60	0.61	0.51	0.51	0.52	0.55

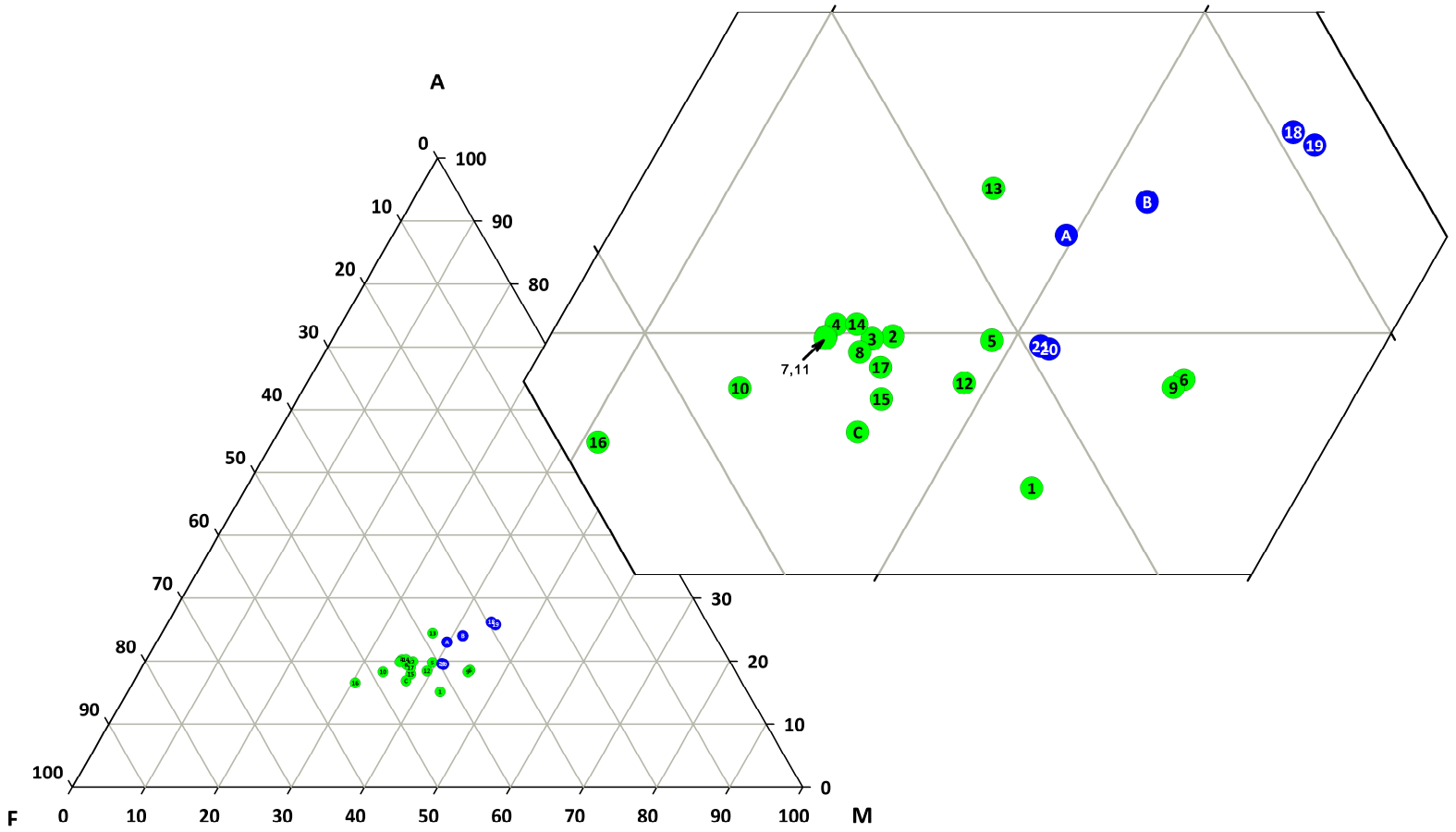

Figure 2.12: AFM projection from quartz, plagioclase and K-feldspar of bulk rock samples from the Steynskraal-Jagers Vrede area. Metagreywackes = green circles; Metapelites = blue circles. Numbers refer to Tags in Tables 2.1 and 2.2. A, B and C are the samples investigated petrographically and modelled in THERMOCALC (A = SK9-CLM; B = SK6C; C = SK4A).

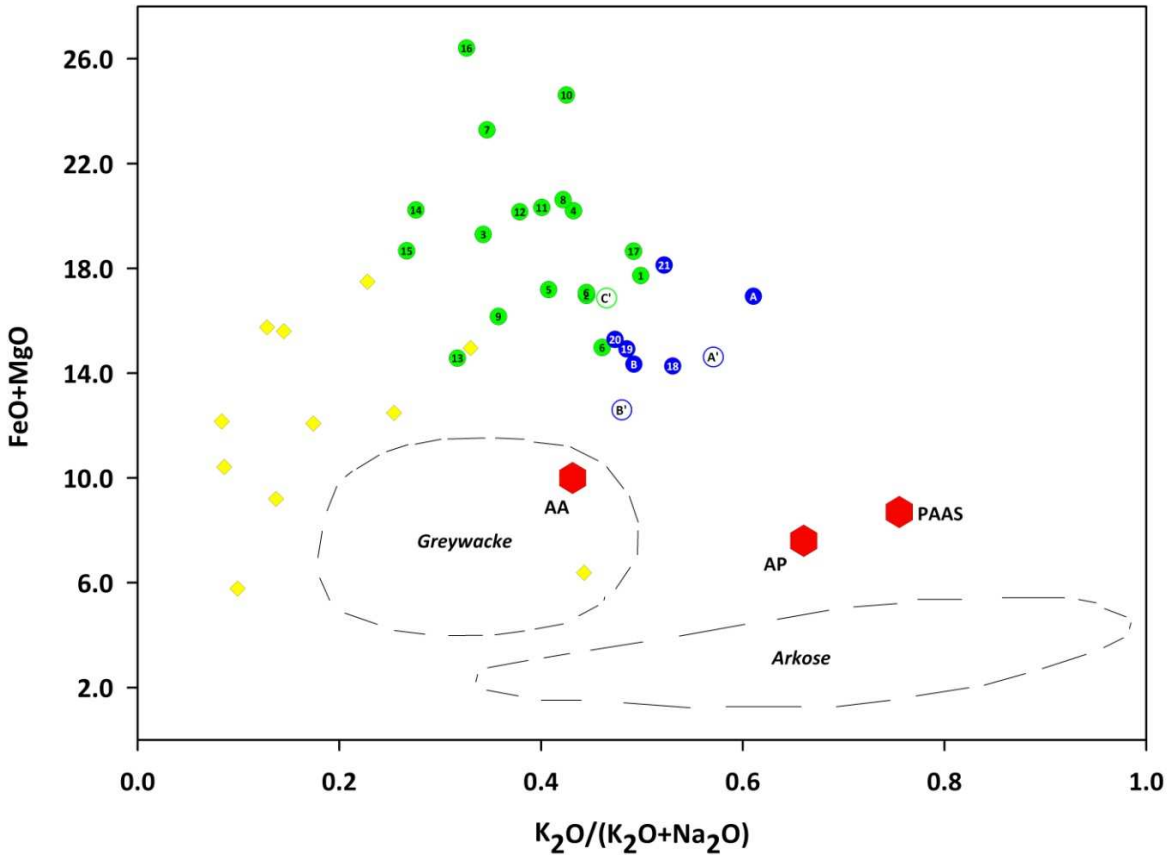

Figure 2.13: Plot of FeO+MgO vs. $K_2O/(K_2O+Na_2O)$ (wt%) comparing Steynskraal metapelites (blue circles) and metagreywackes (green circles) with typical greywackes and arkoses (Chako et al., 1992; McLennan and Taylor, 1985; Pettijohn et al., 1987). The Archaean (AA) and Proterozoic (AP) shale averages are taken from McLennan (1982) and the average post-Archaean shale (PAAS) from Taylor and McLennan (1985). Mafic sediments from the Barberton greenstone belt are included for comparison (yellow diamonds, Dziggel et al., 2006). Melt-reintegrated protolith compositions for SK9-CLM (open blue circle-A'), SK6C (open blue circle-B') and SK4A (open green circle-C') are included (see Section 2.6.2 for procedure).

A comparative isocon plot of the average Steynskraal metapelite and metagreywacke against PAAS (Taylor and McLennan, 1985; Figure 2.14a) indicates relative enrichment in MgO, FeO and Na_2O and relative depletion in K_2O, TiO_2 Al_2O_3 and, to a lesser extent, CaO. K_2O depletion and FeO enrichment is most marked in the metagreywacke. The Steynskraal metapelites and metagreywackes are relatively enriched in MgO, FeO and TiO_2, with depletion in Na_2O and CaO compared to the average Archaean shale (McLennan, 1982), (Figure 2.14b). Only the Steynskraal metagreywackes are less potassic than AA. In Figure 2.14c, the average Steynskraal metapelite and metagreywacke show depletion in K_2O and CaO and enrichment in MgO and FeO relative to the average Proterozoic shale (McLennan, 1982).

Given the evidence of melting and melt extraction in the Steynskraal granulites, disparity between average shale analyses reported by McLennan (1982), Taylor and McLennan (1985), Chako (1992) and Pettijohn et al. (1987) and the samples in this study may in part be attributed to melt loss and a markedly more restitic character of the Steynskraal granulites. Melt-reintegrated bulk compositions (Section 2.6.2; White et al., 2004) from phase equilibria modelling for SK9-CLM (A'), SK6C (B') and SK4A (C'), approach the Average Archaean Shale analysis of McLennan (1982), but are still more enriched in FeO and MgO (Figure 2.15). Moreover, melt reintegration appears to enhance depletion in CaO relative to AA, AP and PAAS. High NiO and MgO contents suggest a primitive, CaO-poor, ultramafic provenance for the Steynskraal sediments.

Mafic and ultramafic xenoliths (Table 2.3) in close proximity to the metapelites and metagreywackes of the Steynskraal traverse are classified as magnesian komatiites according to the MgO-CaO-Al_2O_3 classification diagram of Viljoen et al. (1982) (Figure 2.16a). In Figure 2.16b, the mafic granulites from the Steynskraal area and the oldest TTG sialic crust exposed in the core of the Vredefort Dome (Lana et al., 2004), are compared with the Steynskraal metasedimentary rocks on an Al_2O_3-($CaO+Na_2O$)-K_2O diagram (Nesbitt and Young, 1984). On this diagram, sediments and potential provenance sources may be evaluated. The Chemical Index of Alteration ($CIA = [Al_2O_3/(Al_2O_3 + CaO+Na_2O+K_2O)]*100$) defines the magnitude of the compositional vector trending parallel to the $CaO+Na_2O$-Al_2O_3 axis in Figure

2.16b, which accounts for the loss in mobile CaO and Na_2O from sediments derived from source rocks during weathering. A simple mixing between TTGs and the mafic granulites accounts for the compositional variation within the Steynskraal metasediments. Metagreywackes are characterized by mafic provenance predominantly, with a limited contribution of TTG detritus. In contrast, more sialic, evolved granodiorites are a likely provenance source for the Steynskraal metapelites. The high CIA values for the Steynskraal metasediments, and deviation from a linear mixing line between sialic TTG crust and mafic granulites, attests to marked loss of Na_2O and CaO with weathering as is typical of Archaean metapelites (e.g., Fedo et al., 1995). Fedo et al. (1995) ascribe aggressive chemical weathering in the Archaean to high CO_2 contents in the Archaean atmosphere.

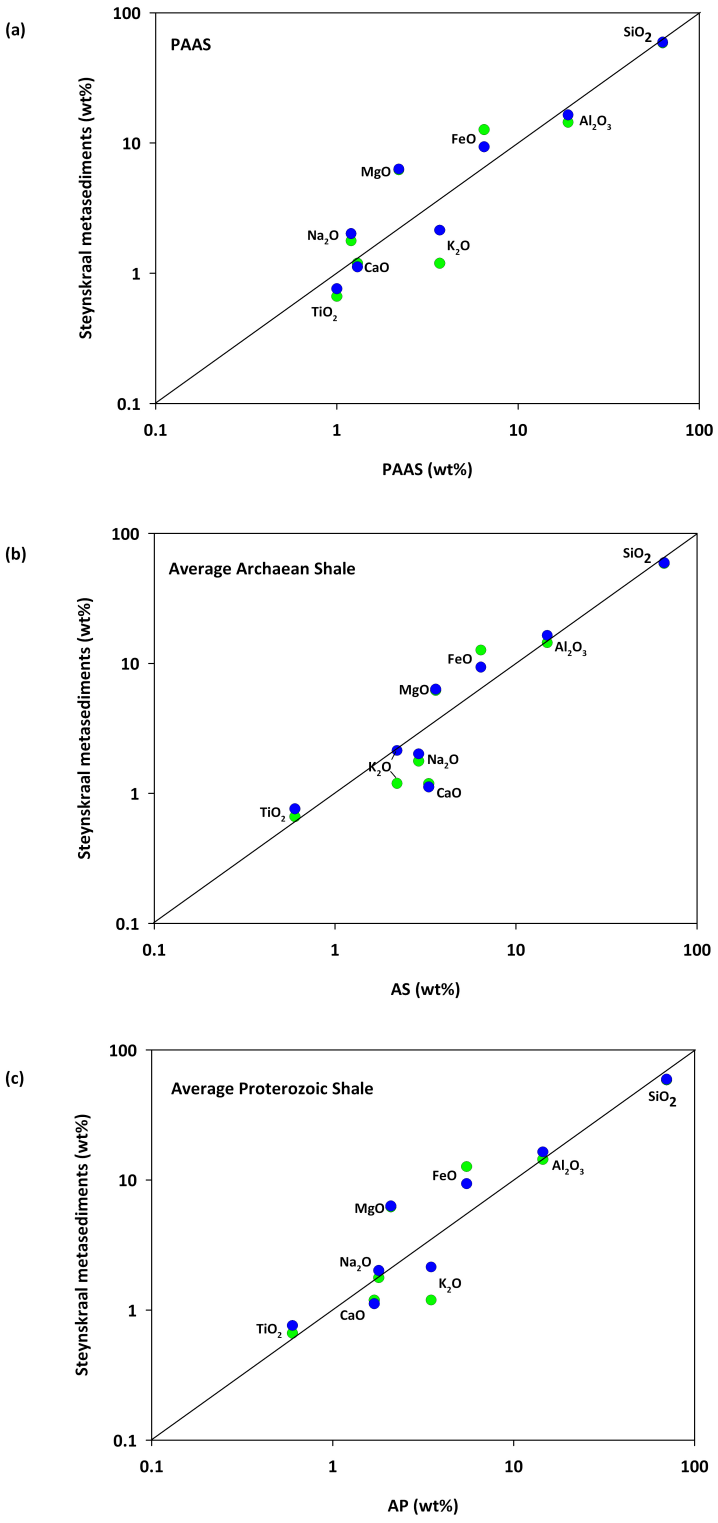

Figure 2.14: Isocon plots comparing elemental abundances in Steynskraal metagreywackes (green circles) and metapelites (blue circles) with the (a) average post-Archaean shale (PAAS) from Taylor and McLennan (1985) (b) average Archaean shale (AA) and (c) average Proterozoic (AP) shale from McLennan (1982).

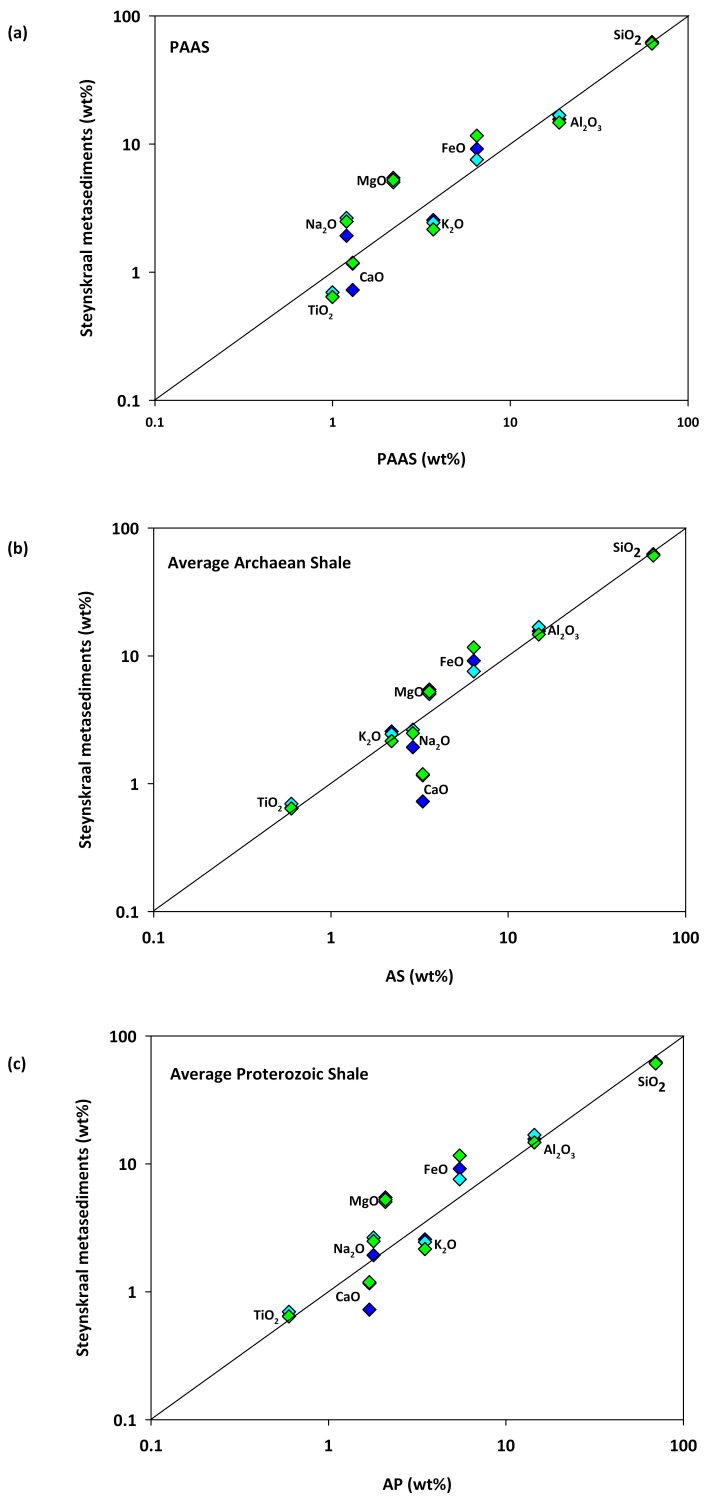

Figure 2.15: Isocon plots comparing elemental abundances in a melt-reintegrated Steynskraal metagreywacke composition (SK4A, green diamond) and two metapelites (SK6C and SK9-CLM cyan and blue diamonds, respectively) with the (a) average post-Archaean shale (PAAS) from Taylor and McLennan (1985) (b) average Archaean shale (AA) and (c) average Proterozoic (AP) shale taken from McLennan (1982).

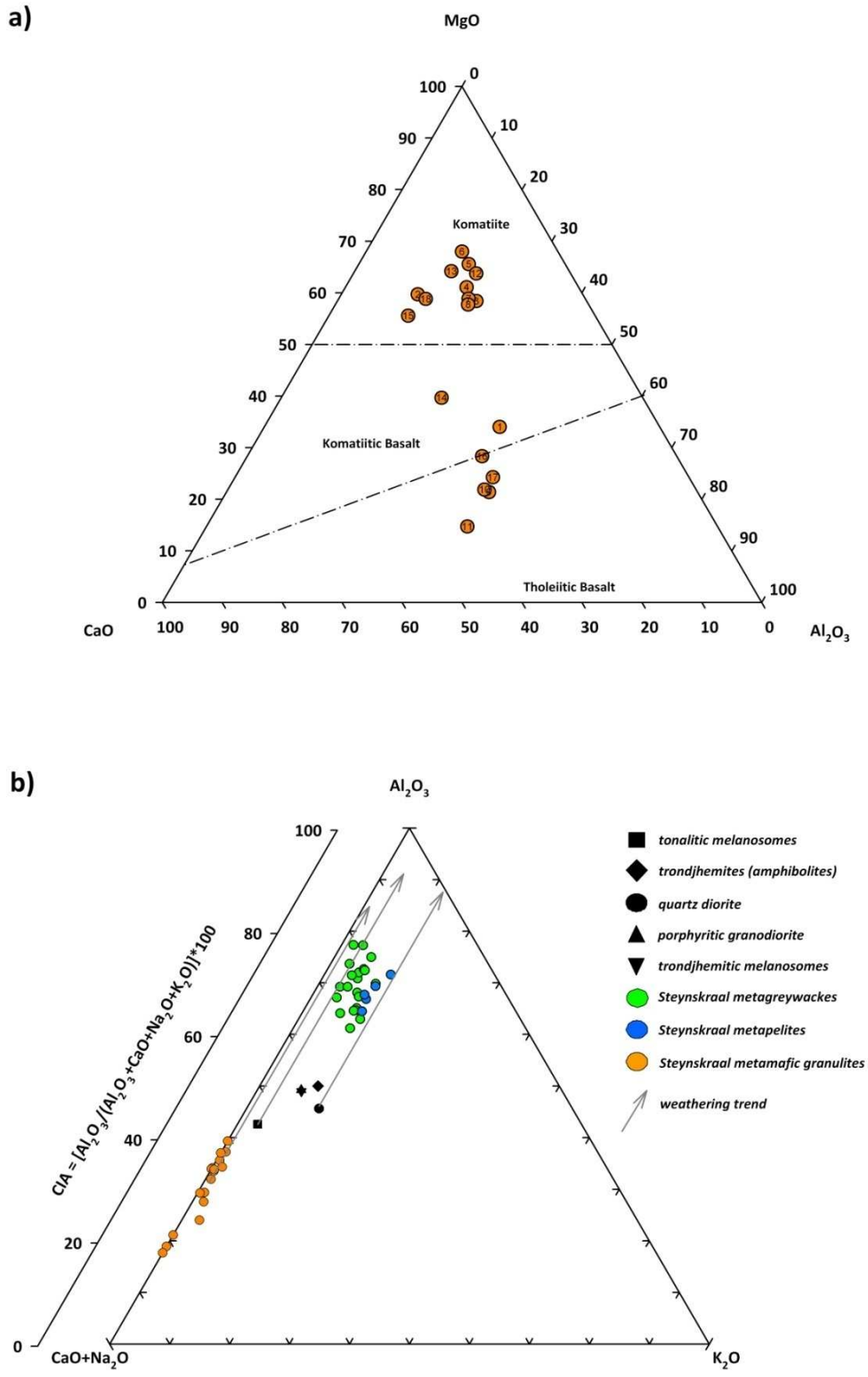

Figure 2.16: Bulk chemical compositions of ultramafic and mafic granulites associated with metapelites and metagreywackes of the Steynskraal traverse. (a) CaO-MgO-Al_2O_3 geochemical classification diagram of Viljoen et al. (1982). Orange circles: ultramafic and mafic granulites from the Steynskraal traverse. Numbers in the metamafic data points are the tags for each analysis in Table 2.3. (b) Al_2O_3-($CaO+Na_2O$)-K_2O diagram for metapelites, metagreywackes, mafic granulites and TTG gneisses from the Steynskraal area (Nesbitt and Young, 1984). Average TTG and granodiorite data are from Lana et al. (2004).

Table 2.3: XRF Bulk rock compositions: Mafic granulites (wt%)

Sample	***VT351***	***VT354***	***VT435***	***VT451***	***VT455***	***VT508***	***VT534***	***VT538***	***VT565***	***VT580***	***VT591***	***VT592***	***VT603***	***VT606***	***VT619***	***VT649***	***VT651***	***VT704***
TAG	***1***	***2***	***3***	***4***	***5***	***6***	***7***	***8***	***9***	***10***	***11***	***12***	***13***	***14***	***15***	***16***	***17***	***18***
SiO_2	56.16	48.94	47.42	48.29	49.47	49.56	46.80	48.83	48.21	48.79	55.59	47.72	49.66	43.62	50.29	47.73	48.47	48.87
TiO_2	0.36	0.53	0.42	0.38	0.64	0.62	0.48	0.42	1.78	1.82	1.11	0.18	0.66	0.77	0.43	0.42	1.11	0.24
Al_2O_3	10.99	4.57	8.55	7.79	6.43	5.46	8.35	7.99	11.95	11.71	11.05	8.01	5.19	10.53	4.76	13.50	13.97	5.35
Fe_2O_3	10.06	13.70	12.01	11.55	12.80	12.42	12.04	11.23	17.10	17.72	11.24	9.56	13.96	11.30	9.92	10.92	13.76	10.25
MnO	0.19	0.22	0.21	0.18	0.19	0.18	0.18	0.17	0.21	0.22	0.24	0.16	0.20	0.20	0.19	0.18	0.20	0.18
MgO	9.51	21.35	21.51	23.51	22.99	23.18	22.65	20.82	5.84	5.98	3.73	24.91	20.61	15.62	19.98	9.75	7.88	21.62
CaO	7.47	9.84	6.78	7.20	5.65	5.46	7.50	7.26	9.50	9.66	10.60	6.17	6.32	13.22	11.22	11.19	10.63	9.80
Na_2O	3.73	1.03	1.16	1.25	1.97	1.82	1.52	1.44	3.79	3.15	4.42	0.69	2.62	1.77	1.08	2.97	2.69	1.30
K_2O	0.16	0.00	0.16	0.00	0.17	0.19	0.01	0.00	0.20	0.16	0.15	0.00	0.59	0.67	0.00	0.58	0.00	0.00
P_2O_5	0.03	0.01	0.03	0.02	0.07	0.06	0.04	0.03	0.25	0.24	0.12	0.00	0.07	0.43	0.00	0.09	0.10	0.02
LOI	-0.17	-0.35	0.19	0.31	-0.16	0	0.24	0.57	0.21	0.25	-0.04	0.63	-0.08	0.61	0.27	0.78	-0.3	0.57
Total	98.49	99.84	98.44	100.48	100.22	98.95	99.81	98.76	99.04	99.7	98.21	98.03	99.8	98.74	98.14	98.11	98.51	98.2

2.5 Mineral chemistry

Compositional data were obtained using the CAMECA SX 100 Electron Probe Micro Analyser at the University of Pretoria. Analysis was conducted using wavelength dispersive spectrometers with an accelerating voltage of 20 kV, a current of 20 nA and a beam diameter of 1 to 3 µm. Natural materials were used as standards. Representative analyses are given in Tables 2.4 - 2.7. Garnet, biotite and orthopyroxene analyses were recalculated using the software AX (T.J.B. Holland, unpublished, December 2007; http://www.esc.cam.ac.uk/astaff/holland/ax.html). Spinel analyses were recalculated using the method of Barnes and Roeder (2001, updated 2004).

Three samples (SK6C, SK4A and SK9-CLM) were analysed in detail, with proportionally more data in SK6C and SK4A where impact-related corona development is less extensive and, consequently, more compositional information of peak Archaean conditions is preserved. All mineral analyses for SK6C, SK9-CLM and SK4A and the respective bulk rock compositions are plotted on an AFM projection from quartz, plagioclase and K-feldspar (Figure 2.17). The ubiquitous presence of plagioclase in the peak assemblage requires projection from excess plagioclase to allow bulk compositions and mineral compositions to be plotted on the same diagram (e.g., Stevens et al., 1997b).

In both the metapelites (SK9-CLM and SK6C) and the metagreywacke (SK4A), garnet is almandine-rich with negligible grossular and spessartine components. Garnet in SK9-CLM (Table 2.4a, Figure 2.17) is the most iron-rich and X_{Alm} (=Fe/(Fe+Mg+Mn+Ca)) ranges from 0.65 to 0.77. Garnets in SK9-CLM exhibit asymmetric zonation profiles ranging from the most magnesian compositions in relict sectors of garnet where replacement by symplectite is limited, grading into more Fe-rich compositions toward the garnet margin adjacent to biotite where symplectite is best developed (Figure 2.18). Garnet from SK6C is more magnesian, with X_{Alm} ranging from 0.51 to 0.63 (Table 2.5a, Figure 2.19). Garnet zonation profiles in SK6C are highly irregular, reflecting variable re-equilibration to higher X_{Fe} [= molar Fe/(Fe + Mg)] adjacent to inclusions and symplectite developed in fractures under post-impact conditions. In SK4A, garnets are Fe-rich with X_{Alm} values between 0.60 and 0.67 (Table 2.6a, Figure 2.20). Garnet zonation profiles for

SK4A are flat with no systematic zonation. The absence of marked zonation in SK4A is consistent with limited corona development and lowest post-shock temperatures modelled in the northwest of the traverse farthest from the centre of the Dome (see Chapters 4 and 6).

In SK9-CLM, cordierite core compositions range in X_{Fe} value from 0.19 to 0.31 (Table 2.4b; Figure 2.21). The most Fe-rich compositions occur closest to included biotite (Figure 2.21a, d) and orthopyroxene (Figure 2.21b, e). In SK6C, cordierite X_{Fe} values vary from 0.11 to 0.17 (Table 2.5b; Figure 2.22), with the most Mg-rich compositions occurring as inclusions in garnet. Cordierites in SK6C exhibit both asymmetric and symmetric profiles. In Figure 2.22, cordierite is zoned asymmetrically with respect to X_{Fe}, i.e., X_{Fe} in cordierite grades to more Fe-rich compositions toward adjacent biotite, reflecting local domainal post-peak re-equilibration (Figure 2.22b, d). Cordierite inclusions in garnet (Figure 2.22c, e) are typically symmetrically zoned, with the most Fe-rich compositions adjacent to the symplectite after cordierite and enclosing garnet. No cordierite is present in the peak assemblage of SK4A.

Orthopyroxene is only found in the metagreywacke (SK4A). No systematic zonation in orthopyroxene composition is observed. Core and rim analyses fall in an X_{Fe} range between 0.38 and 0.42 (Table 2.6b; Figure 2.23). Two methods are commonly applied when formulating the amount of Al in the M1 site (Pattison et al., 2003): $y(\mathrm{Opx})_1 = c_{Al,total}(\mathrm{Opx}) / 2$ and $y(\mathrm{Opx})_2 = c_{Si,total}(\mathrm{Opx}) + c_{Al,total}(\mathrm{Opx}) - 2$, where c_i is cations of component i. Accordingly, $y(\mathrm{Opx})_1$ varies between 0.09 and 0.13 and $y(\mathrm{Opx})_2$ ranges from 0.04 and 0.08 (Table 2.6b; Figure 2.23).

Biotites in SK9-CLM are Fe-rich, with X_{Fe} ranging from 0.38 to 0.54 (Table 2.4c). Ti values are tightly constrained between 0.33 and 0.38 cations per formula unit. The X_{Fe} for biotite in SK6C ranges between 0.24 and 0.32, with more Fe-rich compositions at the rim (Table 2.5c). Ti constitutes between 0.25 to 0.35 cations per formula unit. The most Fe-rich compositions occur in green biotite mantling dark brown-red peak biotite. In the metagreywacke, SK4A, X_{Fe} for biotite ranges between 0.33 and 0.40 and Ti values fall between 0.29 and 0.32 cations per formula unit based on 11 oxygens (Table 2.6c).

Coarse spinel (largely pseudomorphed by cordierite-spinel-pyrite symplectite) is enclosed in cordierite in both SK9-CLM (Table 2.4d) and SK6C (Table 2.5d). Recalculated Fe^{3+} (based on stoichiometric constraints) values are low, implying low oxygen fugacities during the peak event, consistent with the absence of magnetite and presence of only ilmenite in these rocks (White et al., 2000). In SK6C, X_{hrc} [=molar $Fe^{2+}/(Fe^{2+}+Zn+Mg)$] values range between 0.39 and 0.48 (average: 0.44); X_{sp} [=molar $Mg/(Fe^{2+}+Zn+Mg)$] values range from 0.23 to 0.36 (average: 0.29) and X_{gah} [=molar $Zn/(Fe^{2+}+Zn+Mg)$] ranges from 0.03 to 0.11 (average: 0.08). In SK9-CLM, spinel compositions are less variable; X_{hrc} values range between 0.46 and 0.56 (average: 0.52); X_{sp} values range from 0.25 to 0.27 (average: 0.26) and X_{gah} ranges from 0.06 to 0.07 (average: 0.07).

Compositional differences for a particular phase between samples may be attributed in part to bulk rock compositional differences. Bulk rock X_{Mg} for SK6C is 0.55 whilst SK9-CLM is more ferruginous with a bulk rock X_{Mg} of 0.52 (Table 2.2). SK4A has the most Fe-rich bulk rock composition with a bulk rock X_{Mg} of 0.45 (Table 2.1). The magnesian garnet and biotite compositions in SK6C and Fe-rich compositions in SK4A accord with bulk rock X_{Mg} for these samples; however, SK9-CLM phase compositions are markedly more Fe-rich than is predicted by the bulk rock composition, indeed garnet and biotite compositions are more Fe-rich than SK4A. The most Fe-rich garnet compositions in SK9-CLM occur where symplectite is best developed, suggesting re-equilibration to more Fe-rich compositions is intimately linked with the event which induced symplectite formation, i.e., post-shock heating related to impact at 2.02 Ga. Anomalously Fe-rich phase compositions for SK9-CLM may, thus, be attributed to more extensive post-impact re-equilibration at higher post-shock temperatures closer toward the centre of the Dome to more Fe-rich post-impact equilibrium compositions (Section 5.2.1; Chapter 6). In comparison, post-impact replacement of garnet is limited in SK6C, manifesting as only minor perturbation in the Archaean garnet zonation along fractures in SK6C to more Fe-rich compositions. Post-impact symplectite development in SK4A is not sufficient to perturb the Archaean garnet zonation at the resolution analysed.

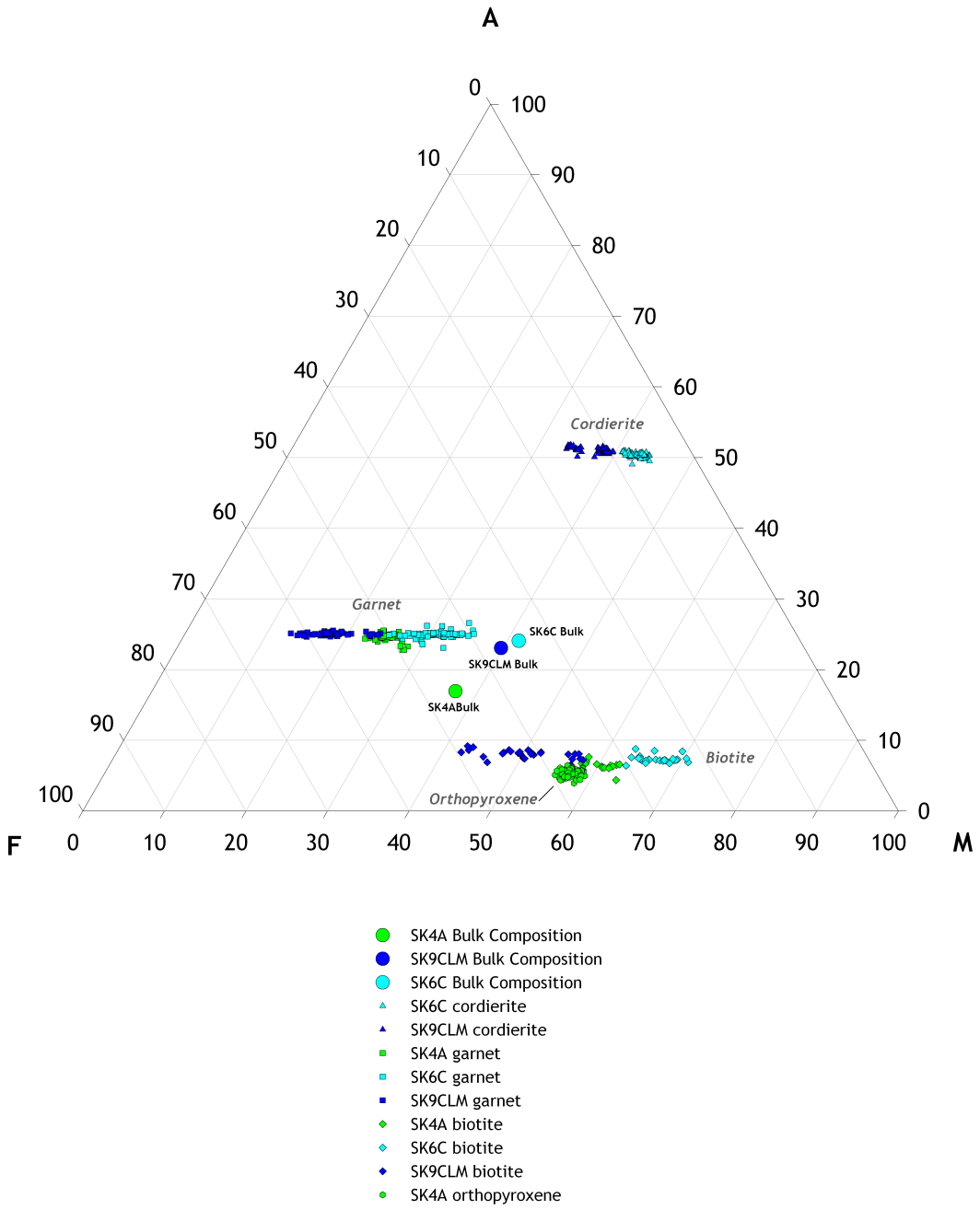

Figure 2.17: AFM projection of all measured mineral compositions and respective bulk rock compositions from quartz, plagioclase and K feldspar (Tables 2.1-2.6). Mineral compositions in SK9-CLM are more Fe-rich than the difference in bulk composition relative to SK6C would appear to accommodate. This is attributed to a greater extent of re-equilibration under post-impact compositions to more Fe-rich compositions in SK9-CLM.

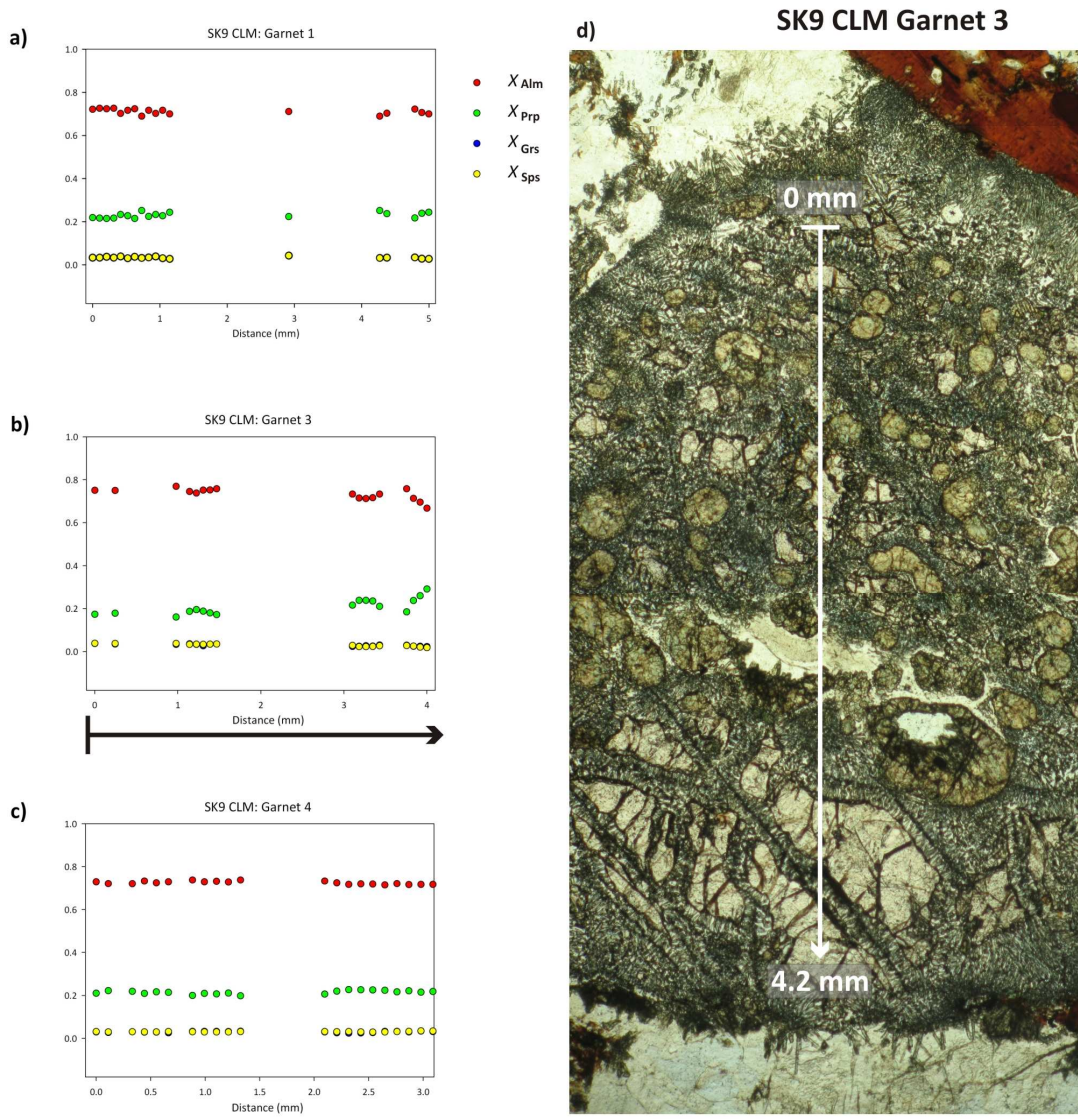

Figure 2.18: Garnet profiles for sample SK9-CLM from rim to rim. (a) SK9-CLM Garnet 1. (b) SK9-CLM Garnet 3. (c) SK9-CLM Garnet 4. (d) PPL image showing the traverse for SK9-CLM Garnet 3 from 0 to 4.2 mm. Lowest X_{Alm} compositions occur in the largest relict garnet fragments from 3.5 to 4.2 mm. Garnet 'islands' from 0-3.5 mm have partially re-equilibrated to more Fe-rich compositions during post-impact symplectite formation.

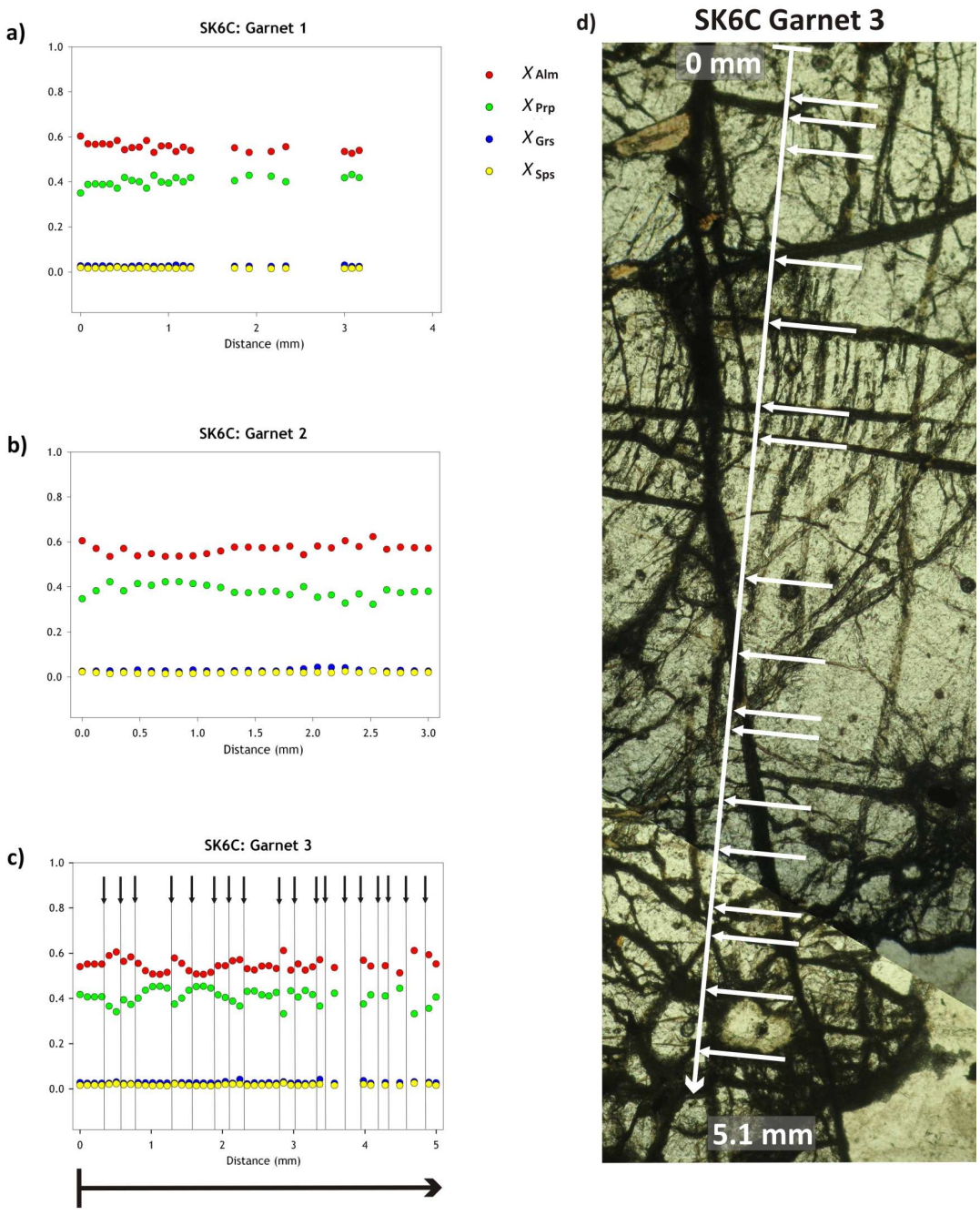

Figure 2.19: Garnet profiles for sample SK6C from rim to rim. (a) SK6C Garnet 1. (b) SK6C Garnet 2. (c) SK6C Garnet 3. Perturbations to higher X_{Alm} contents occur immediately adjacent to fractures (black arrows). (d) PPL image showing the traverse for SK6C Garnet 3 from 0 to 5.1 mm. X_{Alm} increases immediately adjacent to fractures in which post-impact symplectite is developed (white arrows). The unfractured core of garnet is characterized by lowest X_{Alm} compositions.

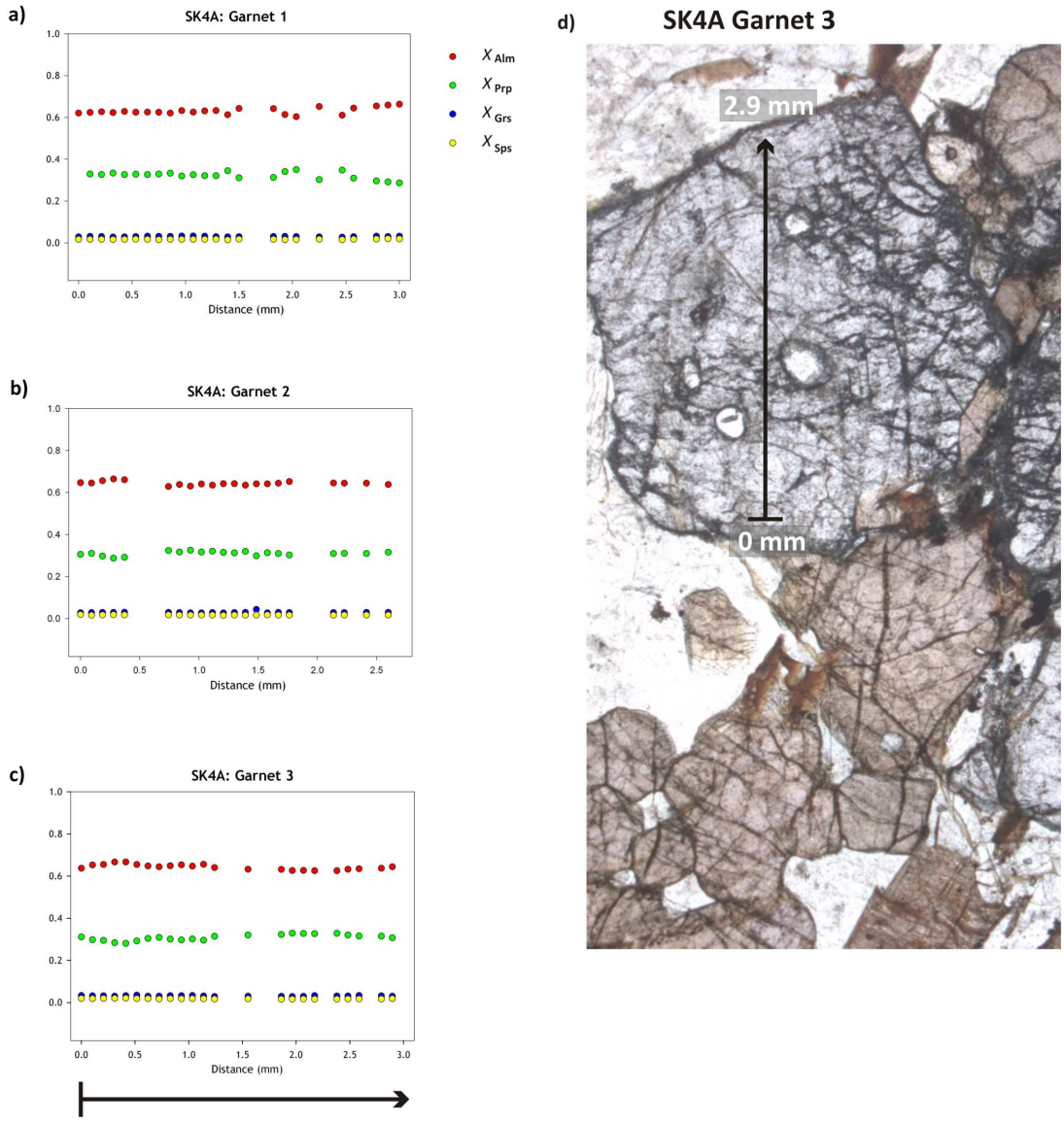

Figure 2.20: Garnet profiles for sample SK4A from rim to rim. (a) SK4A Garnet 1. (b) SK4A Garnet 2. (c) SK4A Garnet 3. (d) PPL image showing the traverse for SK4A Garnet 3 from 0 to 2.9 mm. X_{Alm} remains remarkably constant across the garnet in comparison with SK6C and SK9-CLM.

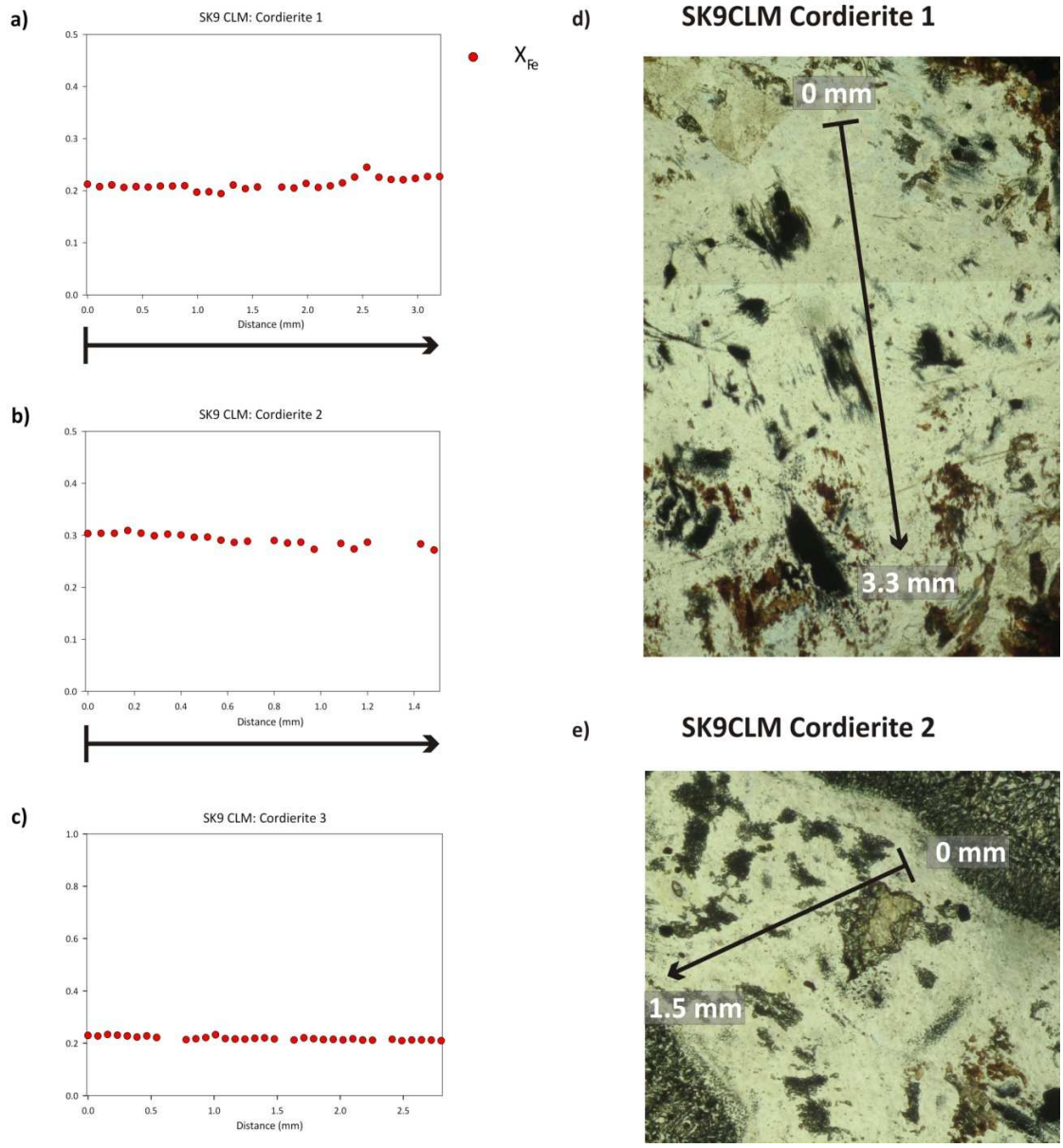

Figure 2.21: Cordierite profiles for sample SK9-CLM from rim to rim. (a) SK9-CLM Cordierite 1. (b) SK9-CLM Cordierite 2. (c) SK9-CLM Cordierite 3. (d) PPL image showing the traverse for SK9-CLM Cordierite 1 from 0 to 3.3 mm. (e) PPL image showing the traverse for SK9-CLM Cordierite 2 from 0 to 1.5 mm. The most Fe-rich compositions occur adjacent to biotite inclusions (toward 3.3 mm in SK9-CLM Cordierite 1) and orthopyroxene inclusions (at 0 mm SK9-CLM Cordierite 2).

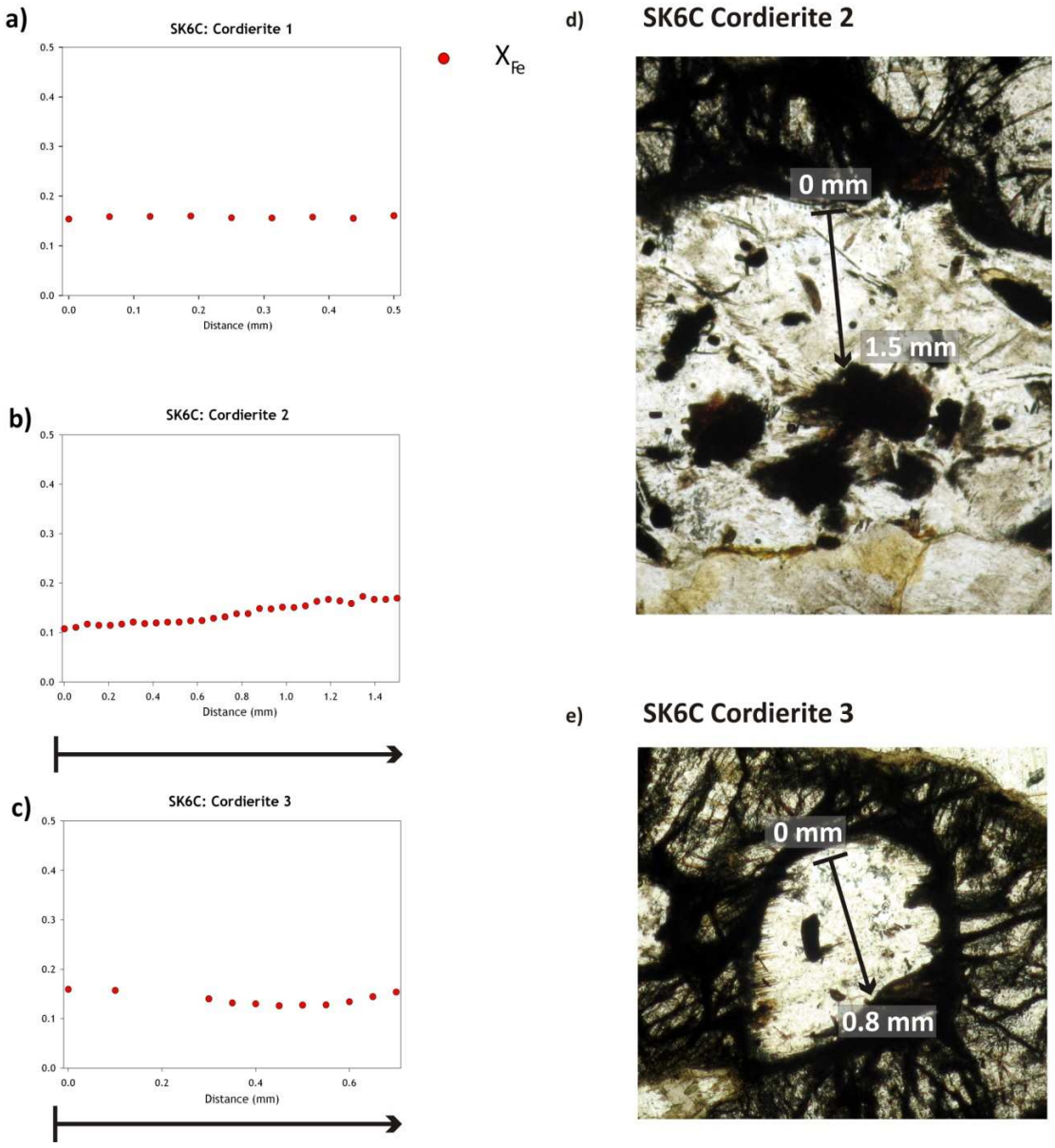

Figure 2.22: Cordierite profiles for sample SK6C from rim to rim. (a) SK6C Cordierite 1. (b) SK6C Cordierite 2. (c) SK6C Cordierite 3. (d) PPL image showing the traverse for SK6C Cordierite 2 from 0 to 1.5 mm. The most Fe-rich compositions occur adjacent to biotite inclusions. (e) PPL image showing the traverse for SK6C Cordierite 3 from 0 to 0.8 mm. Rim compositions are more Fe-rich.

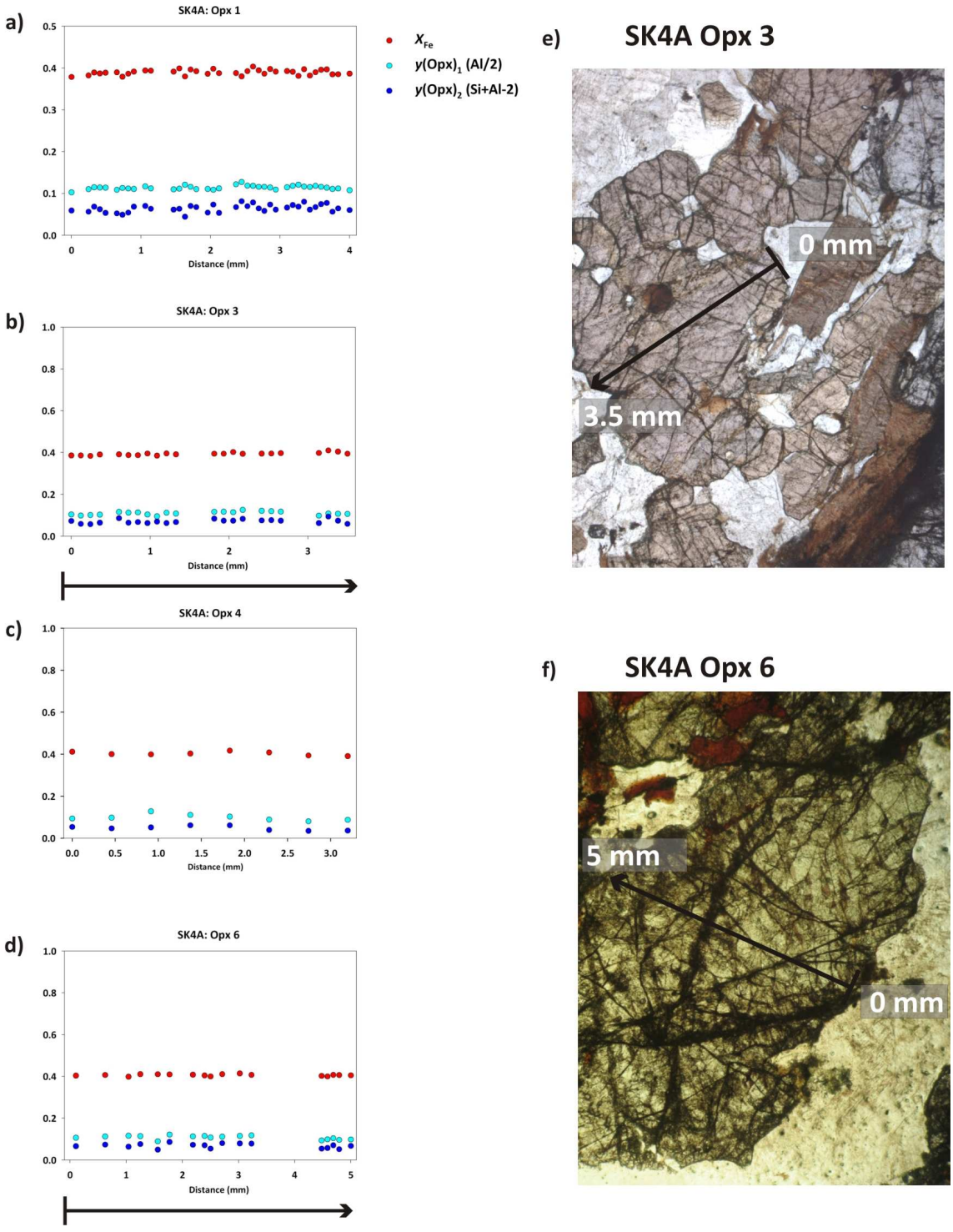

Figure 2.23: SK4A orthopyroxene compositions from rim to rim. (a) SK4A Opx 1. (b) SK4A Opx 3. (c) SK4A Opx 4. (d) SK4A Opx 6. (e) PPL image showing the traverse for SK4A Opx 3 from 0 to 3.5 mm. (f) PPL image showing the traverse for SK4A Opx 6 from 0 to 5.0 mm. No systematic zonation in orthopyroxene composition is observed.

Table 2.4a: Representative mineral analyses SK9-CLM

	Garnet											
Spot	#366	#282	#283	#414	#387	#366	#281	#319	#421	#322	#369	#370
Mineral	Grt (core)	Grt (int)	Grt (int)	Grt (int)	Grt (int)	Grt (int)	Grt (rim)	Grt (rim)	Grt (rim)	Grt (rim)	Grt (rim)	Grt (rim)
SiO_2	37.40	37.00	37.42	37.65	37.12	37.40	36.86	37.39	38.07	37.81	37.06	37.37
TiO_2	0.03	0.03	0.04	0.03	0.00	0.03	0.01	0.01	0.04	0.05	0.05	0.00
Al_2O_3	21.82	21.80	21.82	21.83	21.63	21.82	21.63	22.07	21.88	22.39	21.85	21.96
Cr_2O_3	0.12	0.12	0.11	0.10	0.14	0.12	0.12	0.11	0.09	0.13	0.09	0.10
Fe_2O_3	1.39	2.11	1.17	0.71	1.57	1.39	2.02	0.60	1.45	1.41	1.90	1.42
FeO	31.92	31.04	32.02	33.04	32.70	31.92	31.55	32.25	30.32	29.44	31.71	31.96
MnO	1.33	1.13	1.15	1.18	1.49	1.33	1.12	1.22	0.80	0.64	1.52	1.49
MgO	5.59	5.78	5.70	5.31	4.85	5.59	5.53	5.43	7.43	7.77	5.32	5.45
CaO	1.11	1.32	1.05	1.05	1.16	1.11	1.17	1.18	0.82	0.96	1.16	1.10
Na_2O	0.02	0.02	0.02	0.00	0.01	0.02	0.01	0.01	0.03	0.02	0.03	0.02
K_2O	0.00	0.00	0.00	0.00	0.00	0.00	0.00	0.00	0.00	0.00	0.00	0.00
Total	100.59	100.14	100.38	100.83	100.51	100.59	99.82	100.21	100.78	100.48	100.50	100.73
Oxygens	12.00	12.00	12.00	12.00	12.00	12.00	12.00	12.00	12.00	12.00	12.00	12.00
Si	2.94	2.92	2.95	2.96	2.94	2.94	2.92	2.95	2.95	2.93	2.92	2.94
Ti	0.00	0.00	0.00	0.00	0.00	0.00	0.00	0.00	0.00	0.00	0.00	0.00
Al	2.02	2.03	2.03	2.03	2.02	2.02	2.02	2.05	2.00	2.05	2.03	2.04
Cr	0.01	0.01	0.01	0.01	0.01	0.01	0.01	0.01	0.01	0.01	0.01	0.01
Fe^{3+}	0.08	0.13	0.07	0.04	0.09	0.08	0.12	0.04	0.09	0.08	0.11	0.08
Fe^{2+}	2.10	2.05	2.11	2.17	2.17	2.10	2.09	2.13	1.97	1.91	2.09	2.10
Mn	0.09	0.08	0.08	0.08	0.10	0.09	0.08	0.08	0.05	0.04	0.10	0.10
Mg	0.66	0.68	0.67	0.62	0.57	0.66	0.65	0.64	0.86	0.90	0.63	0.64
Ca	0.09	0.11	0.09	0.09	0.10	0.09	0.10	0.10	0.07	0.08	0.10	0.09
Na	0.00	0.00	0.00	0.00	0.00	0.00	0.00	0.00	0.01	0.00	0.01	0.00
K	0.00	0.00	0.00	0.00	0.00	0.00	0.00	0.00	0.00	0.00	0.00	0.00
Total	8.00	8.00	8.00	8.00	8.00	8.00	8.00	8.00	8.00	8.00	8.00	8.00
X_{Fe}	0.76	0.75	0.76	0.78	0.79	0.76	0.76	0.77	0.70	0.68	0.77	0.77
X_{Alm}	0.71	0.70	0.72	0.73	0.74	0.71	0.72	0.72	0.67	0.65	0.72	0.72
X_{Grs}	0.03	0.04	0.03	0.03	0.03	0.03	0.03	0.03	0.02	0.03	0.03	0.03
X_{Prp}	0.22	0.23	0.23	0.21	0.19	0.22	0.22	0.22	0.29	0.31	0.21	0.22
X_{Sps}	0.03	0.03	0.03	0.03	0.03	0.03	0.03	0.03	0.02	0.01	0.03	0.03

Table 2.4b: Representative mineral analyses SK9-CLM

	Cordierite											
Spot	#197	#134	#145	#207	#147	#148	#151	#188	#213	#164	#172	#183
Mineral	Crd (core)	Crd (core)	Crd (core)	Crd (int)	Crd (int)	Crd (int)	Crd (int)	Crd (rim)	Crd (rim)	Crd (rim)	Crd (rim)	Crd (rim)
SiO_2	48.38	48.43	48.63	48.14	48.70	48.42	48.54	48.48	48.38	47.63	47.90	48.08
TiO_2	0.00	0.01	0.02	0.03	0.00	0.02	0.00	0.00	0.02	0.03	0.03	0.03
Al_2O_3	33.82	33.92	33.99	33.30	33.78	33.63	33.85	33.65	33.22	33.64	33.16	33.44
Cr_2O_3	0.02	0.01	0.01	0.00	0.00	0.01	0.00	0.04	0.00	0.00	0.00	0.00
Fe_2O_3	1.24	1.34	1.35	1.34	1.33	1.34	1.31	1.33	1.40	1.81	1.77	1.67
FeO	4.46	4.83	4.87	4.82	4.79	4.81	4.72	4.78	5.06	6.51	6.38	6.02
MnO	0.06	0.07	0.05	0.06	0.11	0.08	0.07	0.08	0.06	0.13	0.11	0.13
MgO	10.38	9.85	10.13	9.91	10.01	10.08	10.01	10.05	9.87	8.69	8.92	9.06
CaO	0.00	0.00	0.03	0.02	0.03	0.00	0.00	0.02	0.02	0.01	0.01	0.01
Na_2O	0.07	0.05	0.07	0.15	0.03	0.07	0.08	0.09	0.09	0.05	0.10	0.07
K_2O	0.00	0.00	0.00	0.00	0.00	0.00	0.01	0.00	0.00	0.00	0.00	0.00
Total	98.42	98.51	99.16	97.76	98.78	98.45	98.59	98.51	98.12	98.50	98.38	98.52
Oxygens	18.00	18.00	18.00	18.00	18.00	18.00	18.00	18.00	18.00	18.00	18.00	18.00
Si	4.91	4.92	4.91	4.93	4.93	4.92	4.92	4.93	4.94	4.89	4.92	4.92
Ti	0.00	0.00	0.00	0.00	0.00	0.00	0.00	0.00	0.00	0.00	0.00	0.00
Al	4.05	4.06	4.05	4.02	4.03	4.03	4.05	4.03	4.00	4.07	4.01	4.03
Cr	0.00	0.00	0.00	0.00	0.00	0.00	0.00	0.00	0.00	0.00	0.00	0.00
Fe^{3+}	0.10	0.10	0.10	0.10	0.10	0.10	0.10	0.10	0.11	0.14	0.14	0.13
Fe^{2+}	0.38	0.41	0.41	0.41	0.41	0.41	0.40	0.41	0.43	0.56	0.55	0.52
Mn	0.01	0.01	0.00	0.01	0.01	0.01	0.01	0.01	0.01	0.01	0.01	0.01
Mg	1.57	1.49	1.53	1.51	1.51	1.53	1.51	1.52	1.50	1.33	1.37	1.38
Ca	0.00	0.00	0.00	0.00	0.00	0.00	0.00	0.00	0.00	0.00	0.00	0.00
Na	0.01	0.01	0.01	0.03	0.01	0.01	0.02	0.02	0.02	0.01	0.02	0.01
K	0.00	0.00	0.00	0.00	0.00	0.00	0.00	0.00	0.00	0.00	0.00	0.00
Total	11.02	11.00	11.02	11.02	11.00	11.02	11.01	11.02	11.01	11.01	11.01	11.01
X_{Fe}	0.19	0.22	0.21	0.21	0.21	0.21	0.21	0.21	0.22	0.30	0.29	0.27

Table 2.4c: Representative mineral analyses SK9-CLM

	Biotite											
Spot	#129	#130	#131	#122	#118	#141	#117	#119	#137	#116	#111	#112
Mineral	Bt (core)	Bt (core)	Bt (core)	Bt (core)	Bt (core)	Bt (int)	Bt (int)	Bt (int)	Bt (rim)	Bt (rim)	Bt (rim)	Bt (rim)
SiO_2	36.05	35.32	36.84	35.09	35.58	35.39	35.83	35.74	35.45	35.27	34.59	34.64
TiO_2	6.02	6.16	6.09	6.02	6.33	6.34	5.99	6.25	6.69	6.35	6.17	6.13
Al_2O_3	14.75	14.35	15.20	14.60	15.59	14.71	15.10	15.27	14.74	14.71	15.18	15.35
Cr_2O_3	0.68	0.70	0.66	0.77	0.79	0.74	0.82	0.77	0.87	0.78	0.62	0.57
Fe_2O_3	0.00	0.00	0.00	0.00	0.00	0.00	0.00	0.00	0.00	0.00	0.00	0.00
FeO	14.28	14.64	14.50	15.59	17.00	16.99	16.67	16.98	18.69	16.80	19.99	19.67
MnO	0.06	0.09	0.07	0.06	0.00	0.02	0.05	0.08	0.07	0.08	0.04	0.05
MgO	12.99	12.59	13.15	11.48	11.68	11.35	11.59	11.86	10.09	11.29	9.58	9.81
CaO	0.00	0.00	0.02	0.00	0.02	0.00	0.00	0.00	0.00	0.00	0.00	0.00
Na_2O	0.16	0.14	0.16	0.12	0.22	0.20	0.21	0.21	0.18	0.23	0.21	0.17
K_2O	9.46	9.66	9.40	9.02	9.37	9.32	9.16	9.37	9.34	9.36	9.30	9.33
Total	94.46	93.66	96.10	92.76	96.59	95.07	95.43	96.54	96.13	94.88	95.69	95.73
Oxygens	11.00	11.00	11.00	11.00	11.00	11.00	11.00	11.00	11.00	11.00	11.00	11.00
Si	2.72	2.71	2.73	2.72	2.66	2.69	2.71	2.68	2.69	2.69	2.66	2.65
Ti	0.34	0.36	0.34	0.35	0.36	0.36	0.34	0.35	0.38	0.36	0.36	0.35
Al	1.31	1.30	1.33	1.33	1.38	1.32	1.34	1.35	1.32	1.32	1.38	1.39
Cr	0.04	0.04	0.04	0.05	0.05	0.05	0.05	0.05	0.05	0.05	0.04	0.04
Fe^{3+}	0.00	0.00	0.00	0.00	0.00	0.00	0.00	0.00	0.00	0.00	0.00	0.00
Fe^{2+}	0.90	0.94	0.90	1.01	1.06	1.08	1.05	1.06	1.19	1.07	1.28	1.26
Mn	0.00	0.01	0.00	0.00	0.00	0.00	0.00	0.01	0.01	0.01	0.00	0.00
Mg	1.46	1.44	1.45	1.33	1.30	1.29	1.31	1.32	1.14	1.28	1.10	1.12
Ca	0.00	0.00	0.00	0.00	0.00	0.00	0.00	0.00	0.00	0.00	0.00	0.00
Na	0.02	0.02	0.02	0.02	0.03	0.03	0.03	0.03	0.03	0.03	0.03	0.03
K	0.91	0.95	0.89	0.89	0.89	0.91	0.88	0.90	0.90	0.91	0.91	0.91
Total	7.73	7.75	7.70	7.70	7.74	7.73	7.71	7.74	7.71	7.73	7.75	7.75
X_{Fe}	0.38	0.40	0.38	0.43	0.45	0.46	0.45	0.45	0.51	0.46	0.54	0.53

Table 2.4d: Representative mineral analyses SK9-CLM

	Spinel			
Spot	spinel 1	spinel 2	spinel 3	spinel 4
Mineral	Spl (core)	Spl (core)	Spl (core)	Spl (core)
SiO_2	0.25	0.00	0.05	0.00
TiO_2	0.03	0.06	0.11	0.13
V2O5	0.00	0.00	0.00	0.00
Al_2O_3	52.96	53.26	52.94	53.18
Cr_2O_3	5.09	5.05	5.47	4.57
Fe2O3	2.76	3.35	3.42	4.42
FeO	27.99	27.79	28.01	27.63
MnO	0.15	0.13	0.14	0.20
MgO	5.71	6.08	6.00	6.43
ZnO	3.07	3.16	3.16	2.92
CaO	0.00	0.00	0.00	0.00
Na_2O	0.00	0.00	0.00	0.00
K_2O	0.00	0.00	0.00	0.00
Total	98.02	98.88	99.30	99.48
Oxygens	4.00	4.00	4.00	4.00
Si	0.00	0.00	0.00	0.00
Ti	0.00	0.00	0.00	0.00
V	0.00	0.00	0.00	0.00
Al	1.82	1.81	1.80	1.80
Cr	0.12	0.12	0.12	0.10
Fe^{3+}	0.06	0.07	0.07	0.10
Fe^{2+}	0.68	0.67	0.67	0.66
Mn	0.00	0.00	0.00	0.00
Mg	0.25	0.26	0.26	0.27
Zn	0.07	0.07	0.07	0.06
Ca	0.00	0.00	0.00	0.00
Na	0.00	0.00	0.00	0.00
K	0.00	0.00	0.00	0.00
Total	3.00	3.00	3.00	3.00

Table 2.5a: Representative mineral analyses SK6C

	Garnet											
Spot	#138	#150	#192	#228	#136	#182	#209	#230	#243	#167	#175	#221
Mineral	Grt (core)	Grt (core)	Grt (core)	Grt (core)	Grt (int)	Grt (int)	Grt (int)	Grt (int)	Grt (int)	Grt (rim)	Grt (rim)	Grt (rim)
SiO_2	39.32	38.90	39.00	38.97	38.92	39.15	39.25	38.86	38.70	38.10	38.78	38.25
TiO_2	0.03	0.04	0.02	0.00	0.00	0.03	0.02	0.00	0.00	0.01	0.02	0.02
Al_2O_3	23.11	22.84	22.88	22.73	22.84	22.67	22.86	22.70	22.62	22.17	22.68	22.45
Cr_2O_3	0.13	0.16	0.16	0.20	0.15	0.15	0.15	0.18	0.17	0.32	0.20	0.18
Fe_2O_3	0.74	1.43	0.49	1.15	1.09	0.20	0.42	1.07	1.06	0.91	1.11	1.20
FeO	23.78	24.34	24.70	25.00	24.29	26.17	25.29	25.41	26.25	27.80	26.24	27.64
MnO	0.69	0.78	0.68	0.72	0.71	0.80	0.81	0.81	0.90	1.12	0.77	1.01
MgO	11.96	11.29	11.21	11.05	11.37	10.49	11.02	10.60	10.05	8.48	10.16	8.91
CaO	0.94	0.91	0.93	0.88	0.95	0.87	0.90	0.98	0.94	1.11	0.95	0.91
Na_2O	0.01	0.03	0.02	0.01	0.01	0.01	0.01	0.02	0.00	0.02	0.01	0.01
K_2O	0.00	0.00	0.00	0.00	0.00	0.00	0.00	0.00	0.00	0.00	0.00	0.00
Total	100.64	100.57	100.04	100.60	100.22	100.52	100.69	100.52	100.58	99.95	100.81	100.46
Oxygens	12.00	12.00	12.00	12.00	12.00	12.00	12.00	12.00	12.00	12.00	12.00	12.00
Si	2.95	2.94	2.96	2.95	2.95	2.97	2.97	2.95	2.95	2.95	2.95	2.94
Ti	0.00	0.00	0.00	0.00	0.00	0.00	0.00	0.00	0.00	0.00	0.00	0.00
Al	2.05	2.03	2.05	2.03	2.04	2.03	2.04	2.03	2.03	2.03	2.03	2.04
Cr	0.01	0.01	0.01	0.01	0.01	0.01	0.01	0.01	0.01	0.02	0.01	0.01
Fe^{3+}	0.04	0.08	0.03	0.07	0.06	0.01	0.02	0.06	0.06	0.05	0.06	0.07
Fe^{2+}	1.49	1.54	1.57	1.58	1.54	1.66	1.60	1.61	1.67	1.80	1.67	1.78
Mn	0.04	0.05	0.04	0.05	0.05	0.05	0.05	0.05	0.06	0.07	0.05	0.07
Mg	1.34	1.27	1.27	1.25	1.28	1.19	1.24	1.20	1.14	0.98	1.15	1.02
Ca	0.08	0.07	0.08	0.07	0.08	0.07	0.07	0.08	0.08	0.09	0.08	0.08
Na	0.00	0.00	0.00	0.00	0.00	0.00	0.00	0.00	0.00	0.00	0.00	0.00
K	0.00	0.00	0.00	0.00	0.00	0.00	0.00	0.00	0.00	0.00	0.00	0.00
Total	8.00	8.00	8.00	8.00	8.00	8.00	8.00	8.00	8.00	8.00	8.00	8.00
X_{Fe}	0.53	0.55	0.55	0.56	0.55	0.58	0.56	0.57	0.59	0.65	0.59	0.64
X_{Alm}	0.51	0.52	0.53	0.54	0.52	0.56	0.54	0.55	0.57	0.61	0.57	0.60
X_{Grs}	0.03	0.03	0.03	0.02	0.03	0.02	0.02	0.03	0.03	0.03	0.03	0.03
X_{Prp}	0.45	0.43	0.43	0.42	0.44	0.40	0.42	0.41	0.39	0.33	0.39	0.35
X_{Sps}	0.01	0.02	0.01	0.02	0.02	0.02	0.02	0.02	0.02	0.03	0.02	0.02

Table 2.5b: Representative mineral analyses SK6C

	Cordierite											
Spot	#222	#185	#165	#122	#173	4#208	#225	#190	#180	#210	#141	#151
Mineral	Crd (core)	Crd (core)	Crd (core)	Crd (core)	Crd (int)	Crd (int)	Crd (rim)	Crd (rim)	Crd (rim)	Crd (rim)	Crd (rim)	Crd (rim) adj grt
SiO_2	48.73	48.51	48.75	48.76	48.75	48.70	48.68	48.84	48.48	48.82	49.15	49.10
TiO_2	0.00	0.01	0.00	0.02	0.02	0.02	0.00	0.01	0.00	0.00	0.03	0.00
Al_2O_3	33.82	33.86	34.13	34.05	34.24	34.05	33.75	33.83	34.23	34.00	34.23	34.35
Cr_2O_3	0.02	0.00	0.02	0.00	0.00	0.00	0.02	0.00	0.00	0.03	0.01	0.03
Fe_2O_3	0.85	1.03	0.86	0.92	1.05	1.01	1.00	1.04	1.09	1.09	0.79	0.71
FeO	3.05	3.70	3.09	3.30	3.77	3.65	3.58	3.75	3.94	3.93	2.86	2.56
MnO	0.04	0.06	0.09	0.05	0.06	0.04	0.04	0.06	0.10	0.06	0.07	0.04
MgO	11.66	10.89	11.42	11.31	10.85	11.10	11.05	11.02	10.83	10.97	11.54	11.91
CaO	0.01	0.01	0.00	0.00	0.02	0.03	0.00	0.01	0.00	0.03	0.00	0.02
Na_2O	0.09	0.11	0.11	0.10	0.08	0.07	0.10	0.09	0.07	0.13	0.04	0.07
K_2O	0.00	0.02	0.00	0.01	0.00	0.00	0.01	0.01	0.01	0.00	0.00	0.00
Total	98.26	98.19	98.47	98.51	98.83	98.67	98.23	98.66	98.75	99.06	98.72	98.79
Oxygens	18.00	18.00	18.00	18.00	18.00	18.00	18.00	18.00	18.00	18.00	18.00	18.00
Si	4.92	4.92	4.91	4.92	4.91	4.91	4.93	4.93	4.89	4.91	4.93	4.92
Ti	0.00	0.00	0.00	0.00	0.00	0.00	0.00	0.00	0.00	0.00	0.00	0.00
Al	4.03	4.05	4.05	4.05	4.07	4.05	4.03	4.02	4.07	4.03	4.05	4.05
Cr	0.00	0.00	0.00	0.00	0.00	0.00	0.00	0.00	0.00	0.00	0.00	0.00
Fe^{3+}	0.06	0.08	0.07	0.07	0.08	0.08	0.08	0.08	0.08	0.08	0.06	0.05
Fe^{2+}	0.26	0.31	0.26	0.28	0.32	0.31	0.30	0.32	0.33	0.33	0.24	0.21
Mn	0.00	0.01	0.01	0.00	0.01	0.00	0.00	0.01	0.01	0.01	0.01	0.00
Mg	1.75	1.65	1.72	1.70	1.63	1.67	1.67	1.66	1.63	1.65	1.73	1.78
Ca	0.00	0.00	0.00	0.00	0.00	0.00	0.00	0.00	0.00	0.00	0.00	0.00
Na	0.02	0.02	0.02	0.02	0.02	0.01	0.02	0.02	0.01	0.03	0.01	0.01
K	0.00	0.00	0.00	0.00	0.00	0.00	0.00	0.00	0.00	0.00	0.00	0.00
Total	11.04	11.03	11.04	11.04	11.02	11.03	11.03	11.03	11.04	11.04	11.02	11.04
X_{Fe}	0.13	0.16	0.13	0.14	0.16	0.16	0.15	0.16	0.17	0.17	0.12	0.11

Table 2.5c: Representative mineral analyses SK6C

	Biotite											
Spot	#108	#111	#118	#102	#110	#113	#98	#100	#109	#114	#115	#106
Mineral	Bt (core)	Bt (core)	Bt (core)	Bt (int)	Bt (int)	Bt (int)	Bt (rim)	Bt (rim)	Bt (rim)	Bt (rim)	Bt (rim)	Bt (rim)
SiO_2	36.65	36.80	37.31	36.89	37.30	36.53	36.61	36.28	36.22	36.40	36.69	37.83
TiO_2	5.49	6.11	5.07	5.71	6.30	6.04	5.68	5.39	5.25	5.66	5.43	5.11
Al_2O_3	15.35	14.96	15.13	15.09	15.43	14.84	15.14	15.58	17.06	15.27	15.27	14.53
Cr_2O_3	0.81	0.84	0.88	0.86	0.86	0.78	0.86	0.79	0.80	0.83	0.91	0.45
Fe_2O_3	0.00	0.00	0.00	0.00	0.00	0.00	0.00	0.00	0.00	0.00	0.00	0.00
FeO	9.98	9.37	10.81	11.11	9.19	9.63	11.78	11.40	11.06	12.26	11.96	13.15
MnO	0.05	0.00	0.03	0.01	0.00	0.03	0.05	0.02	0.06	0.03	0.04	0.02
MgO	16.56	16.66	16.20	15.92	16.07	15.79	15.39	14.58	14.74	15.09	15.38	15.50
CaO	0.00	0.01	0.00	0.01	0.00	0.01	0.00	0.00	0.03	0.03	0.00	0.00
Na_2O	0.20	0.13	0.12	0.15	0.10	0.10	0.17	0.19	0.08	0.13	0.17	0.16
K_2O	9.80	9.82	9.82	9.64	9.52	9.69	9.75	9.38	8.50	9.64	9.69	9.52
Total	94.90	94.71	95.38	95.40	94.78	93.45	95.44	93.62	93.81	95.35	95.55	96.28
Oxygens	11.00	11.00	11.00	11.00	11.00	11.00	11.00	11.00	11.00	11.00	11.00	11.00
Si	2.70	2.71	2.74	2.72	2.73	2.73	2.71	2.72	2.69	2.70	2.71	2.78
Ti	0.30	0.34	0.28	0.32	0.35	0.34	0.32	0.30	0.29	0.32	0.30	0.28
Al	1.33	1.30	1.31	1.31	1.33	1.31	1.32	1.38	1.49	1.34	1.33	1.26
Cr	0.05	0.05	0.05	0.05	0.05	0.05	0.05	0.05	0.05	0.05	0.05	0.03
Fe^{3+}	0.00	0.00	0.00	0.00	0.00	0.00	0.00	0.00	0.00	0.00	0.00	0.00
Fe^{2+}	0.62	0.58	0.67	0.68	0.56	0.60	0.73	0.72	0.69	0.76	0.74	0.81
Mn	0.00	0.00	0.00	0.00	0.00	0.00	0.00	0.00	0.00	0.00	0.00	0.00
Mg	1.82	1.83	1.78	1.75	1.75	1.76	1.70	1.63	1.63	1.67	1.69	1.70
Ca	0.00	0.00	0.00	0.00	0.00	0.00	0.00	0.00	0.00	0.00	0.00	0.00
Na	0.03	0.02	0.02	0.02	0.01	0.01	0.02	0.03	0.01	0.02	0.02	0.02
K	0.92	0.92	0.92	0.91	0.89	0.92	0.92	0.90	0.81	0.91	0.91	0.89
Total	7.78	7.75	7.77	7.75	7.68	7.72	7.77	7.73	7.66	7.76	7.77	7.76
X_{Fe}	0.25	0.24	0.27	0.28	0.24	0.26	0.30	0.30	0.30	0.31	0.30	0.32

Table 2.5d: Representative mineral analyses SK6C

	Spinel						
Spot	spinel 1	spinel 2	spinel 3	spinel 4	spinel 5	spinel 6	spinel 7
Mineral	Spl (core)	Spl (core)	Spl (core)	Spl (core)	Spl (core)	Spl (core)	Spl (core)
SiO_2	0.03	0.08	0.03	0.06	0.02	0.05	0.07
TiO_2	0.02	0.02	0.02	0.01	0.06	0.09	0.03
V_2O_5	0.00	0.00	0.00	0.00	0.00	0.00	0.00
Al_2O_3	54.75	55.08	54.07	48.91	47.16	47.26	46.16
Cr_2O_3	3.86	3.89	4.79	8.47	8.99	9.00	12.42
Fe_2O_3	3.23	3.15	3.24	3.84	5.80	5.85	3.81
FeO	22.27	22.34	22.49	26.43	29.18	28.90	26.38
MnO	0.12	0.11	0.12	0.18	0.14	0.16	0.18
MgO	8.47	8.51	8.23	5.27	5.38	5.63	6.09
ZnO	5.00	5.09	5.20	4.78	1.47	1.43	3.12
CaO	0.00	0.00	0.00	0.00	0.00	0.00	0.00
Na_2O	0.00	0.00	0.00	0.00	0.00	0.00	0.00
K_2O	0.00	0.00	0.00	0.00	0.00	0.00	0.00
Total	97.75	98.28	98.18	97.94	98.20	98.38	98.26
Oxygens	4.00	4.00	4.00	4.00	4.00	4.00	4.00
Si	0.00	0.00	0.00	0.00	0.00	0.00	0.00
Ti	0.00	0.00	0.00	0.00	0.00	0.00	0.00
V	0.00	0.00	0.00	0.00	0.00	0.00	0.00
Al	1.84	1.84	1.82	1.71	1.66	1.65	1.62
Cr	0.09	0.09	0.11	0.20	0.21	0.21	0.29
Fe^{3+}	0.07	0.07	0.07	0.09	0.13	0.13	0.09
Fe^{2+}	0.53	0.53	0.54	0.66	0.73	0.72	0.66
Mn	0.00	0.00	0.00	0.00	0.00	0.00	0.00
Mg	0.36	0.36	0.35	0.23	0.24	0.25	0.27
Zn	0.11	0.11	0.11	0.10	0.03	0.03	0.07
Ca	0.00	0.00	0.00	0.00	0.00	0.00	0.00
Na	0.00	0.00	0.00	0.00	0.00	0.00	0.00
K	0.00	0.00	0.00	0.00	0.00	0.00	0.00
Total	3.00	3.00	3.00	3.00	3.00	3.00	3.00

Table 2.6a: Representative mineral analyses SK4A

	Garnet											
Spot	#31	#19	#40	#100	#18	#48	#106	#4	#28	#57	#94	#112
Mineral	Grt (core)	Grt (core)	Grt (core)	Grt (core)	Grt (int)	Grt (int)	Grt (int)	Grt (rim)	Grt (rim)	Grt (rim)	Grt (rim)	Grt (rim)
SiO_2	38.11	38.35	38.18	38.38	39.91	38.46	38.40	37.65	38.10	38.08	38.20	38.17
TiO_2	0.00	0.02	0.04	0.00	0.02	0.10	0.00	0.03	0.06	0.02	0.02	0.02
Al_2O_3	22.28	22.28	22.24	22.25	22.26	22.01	22.35	21.93	22.33	22.21	22.25	22.26
Cr_2O_3	0.25	0.11	0.10	0.15	0.11	0.14	0.11	0.18	0.14	0.20	0.16	0.12
Fe_2O_3	1.32	1.42	1.26	1.11	1.01	0.28	1.15	1.78	1.33	1.03	1.35	0.76
FeO	28.19	29.41	28.84	28.92	26.86	29.50	28.78	29.51	29.38	29.67	28.87	30.16
MnO	0.74	0.78	0.73	0.80	0.69	0.74	0.73	0.79	0.77	0.82	0.80	0.80
MgO	8.52	8.06	8.18	8.25	7.03	8.06	8.36	7.50	7.92	7.52	8.15	7.46
CaO	1.02	0.99	1.16	1.10	1.41	1.07	1.10	1.03	1.04	1.11	1.09	1.09
Na_2O	0.03	0.01	0.01	0.01	1.26	0.02	0.02	0.01	0.00	0.05	0.02	0.00
K_2O	0.00	0.00	0.00	0.00	0.00	0.00	0.00	0.00	0.00	0.00	0.00	0.00
Total	100.33	101.28	100.61	100.86	100.46	100.35	100.88	100.24	100.94	100.60	100.78	100.76
Oxygens	12.00	12.00	12.00	12.00	12.00	12.00	12.00	12.00	12.00	12.00	12.00	12.00
Si	2.94	2.95	2.95	2.95	3.06	2.98	2.95	2.93	2.94	2.95	2.95	2.96
Ti	0.00	0.00	0.00	0.00	0.00	0.01	0.00	0.00	0.00	0.00	0.00	0.00
Al	2.03	2.02	2.02	2.02	2.01	2.01	2.03	2.02	2.03	2.03	2.02	2.03
Cr	0.02	0.01	0.01	0.01	0.01	0.01	0.01	0.01	0.01	0.01	0.01	0.01
Fe^{3+}	0.08	0.08	0.07	0.06	0.06	0.02	0.07	0.11	0.08	0.06	0.08	0.04
Fe^{2+}	1.82	1.89	1.86	1.86	1.72	1.91	1.85	1.92	1.90	1.92	1.86	1.95
Mn	0.05	0.05	0.05	0.05	0.05	0.05	0.05	0.05	0.05	0.05	0.05	0.05
Mg	0.98	0.92	0.94	0.95	0.80	0.93	0.96	0.87	0.91	0.87	0.94	0.86
Ca	0.08	0.08	0.10	0.09	0.12	0.09	0.09	0.09	0.09	0.09	0.09	0.09
Na	0.00	0.00	0.00	0.00	0.19	0.00	0.00	0.00	0.00	0.01	0.00	0.00
K	0.00	0.00	0.00	0.00	0.00	0.00	0.00	0.00	0.00	0.00	0.00	0.00
Total	8.00	8.00	8.00	8.00	8.00	8.00	8.00	8.00	8.00	8.00	8.00	8.00
X_{Fe}	0.65	0.67	0.66	0.66	0.68	0.67	0.66	0.69	0.68	0.69	0.67	0.69
X_{Alm}	0.62	0.64	0.63	0.63	0.64	0.64	0.63	0.66	0.64	0.65	0.63	0.66
X_{Grs}	0.03	0.03	0.03	0.03	0.04	0.03	0.03	0.03	0.03	0.03	0.03	0.03
X_{Prp}	0.33	0.31	0.32	0.32	0.30	0.31	0.33	0.30	0.31	0.30	0.32	0.29
X_{Sps}	0.02	0.02	0.02	0.02	0.02	0.02	0.02	0.02	0.02	0.02	0.02	0.02

Table 2.6b: Representative mineral analyses SK4A

	Orthopyroxene											
Spot	#5	#35	#77	#104	#67	#112	#1	#8	#14	#56	#59	#87
Mineral	Opx (core)	Opx (core)	Opx (core)	Opx (core)	Opx (int)	Opx (int)	Opx (rim)	Opx (rim)	Opx (rim)	Opx (rim)	Opx (rim)	Opx (rim)
SiO_2	48.93	48.89	48.82	49.26	49.39	48.78	49.41	49.51	48.99	48.91	49.87	49.16
TiO_2	0.10	0.30	0.11	0.78	0.03	0.21	0.09	0.05	0.15	0.14	0.08	0.14
Al_2O_3	4.56	5.08	5.65	3.97	4.64	5.14	4.17	3.92	5.16	5.03	4.66	4.80
Cr_2O_3	0.23	0.30	0.32	0.15	0.26	0.21	0.30	0.30	0.31	0.29	0.28	0.28
Fe_2O_3	2.39	3.32	2.59	1.16	2.69	2.57	2.33	3.22	3.09	2.87	1.77	1.86
FeO	24.28	22.64	22.79	24.31	23.16	23.50	24.23	23.02	22.61	22.39	22.92	23.64
MnO	0.22	0.21	0.19	0.19	0.22	0.21	0.22	0.19	0.15	0.20	0.21	0.20
MgO	19.09	20.08	19.73	19.61	19.91	19.45	19.45	20.19	20.11	20.07	20.50	19.58
CaO	0.06	0.04	0.08	0.05	0.05	0.04	0.04	0.04	0.03	0.10	0.03	0.04
Na_2O	0.00	0.01	0.03	0.02	0.02	0.02	0.00	0.00	0.01	0.02	0.00	0.02
K_2O	0.00	0.00	0.03	0.00	0.02	0.00	0.00	0.00	0.01	0.01	0.00	0.01
Total	99.62	100.53	100.08	99.38	100.12	99.87	100.00	100.12	100.31	99.74	100.14	99.54
Oxygens	6.00	6.00	6.00	6.00	6.00	6.00	6.00	6.00	6.00	6.00	6.00	6.00
Si	1.86	1.83	1.83	1.87	1.86	1.84	1.87	1.86	1.83	1.84	1.87	1.86
Ti	0.00	0.01	0.00	0.02	0.00	0.01	0.00	0.00	0.00	0.00	0.00	0.00
Al	0.20	0.22	0.25	0.18	0.21	0.23	0.19	0.17	0.23	0.22	0.21	0.21
Cr	0.01	0.01	0.01	0.01	0.01	0.01	0.01	0.01	0.01	0.01	0.01	0.01
Fe^{3+}	0.07	0.09	0.07	0.03	0.08	0.07	0.07	0.09	0.09	0.08	0.05	0.05
Fe^{2+}	0.77	0.71	0.72	0.77	0.73	0.74	0.77	0.72	0.71	0.71	0.72	0.75
Mn	0.01	0.01	0.01	0.01	0.01	0.01	0.01	0.01	0.01	0.01	0.01	0.01
Mg	1.08	1.12	1.10	1.11	1.12	1.09	1.10	1.13	1.12	1.13	1.14	1.10
Ca	0.00	0.00	0.00	0.00	0.00	0.00	0.00	0.00	0.00	0.00	0.00	0.00
Na	0.00	0.00	0.00	0.00	0.00	0.00	0.00	0.00	0.00	0.00	0.00	0.00
K	0.00	0.00	0.00	0.00	0.00	0.00	0.00	0.00	0.00	0.00	0.00	0.00
Total	4.00	4.00	4.00	4.00	4.00	4.00	4.00	4.00	4.00	4.00	4.00	4.00
X_{Fe}	0.42	0.39	0.39	0.41	0.40	0.40	0.41	0.39	0.39	0.39	0.39	0.40
$y(opx)_1$ $(Al_{tot}/2)$	0.10	0.11	0.13	0.09	0.10	0.11	0.09	0.09	0.11	0.11	0.10	0.11
$y(opx)_2$ $(Si_{tot}+Al_{tot}-2)$	0.06	0.05	0.08	0.05	0.06	0.07	0.05	0.04	0.06	0.06	0.07	0.07

Table 2.6c: Representative mineral analyses SK4A

	Biotite											
Spot	#89	#90	#1	#2	#4	#58	#92	#93	#5	#91	#94	#56
Mineral	Bt (core)	Bt (core)	Bt (int)	Bt (int)	Bt (int)	Bt (int)	Bt (int)	Bt (int)	Bt (rim)	Bt (rim)	Bt (rim)	Bt (rim)
SiO_2	36.99	37.13	36.31	36.49	36.91	36.24	36.76	36.77	37.01	37.13	36.99	35.56
TiO_2	5.43	5.44	5.22	5.37	5.37	5.19	5.67	5.50	5.45	5.38	5.54	5.28
Al_2O_3	14.68	14.77	14.37	14.28	14.68	14.72	14.58	14.43	14.77	14.44	14.46	13.95
Cr_2O_3	0.44	0.43	0.44	0.46	0.47	0.41	0.50	0.46	0.35	0.48	0.43	0.35
Fe_2O_3	0.00	0.00	0.00	0.00	0.00	0.00	0.00	0.00	0.00	0.00	0.00	0.00
FeO	13.55	13.96	13.38	13.57	13.10	14.82	14.10	14.14	15.04	14.37	13.97	15.11
MnO	0.00	0.01	0.02	0.00	0.05	0.05	0.02	0.04	0.04	0.00	0.01	0.02
MgO	15.12	15.02	14.56	14.42	14.88	13.94	14.42	14.46	14.03	14.30	14.47	12.61
CaO	0.00	0.00	0.00	0.00	0.00	0.00	0.00	0.00	0.02	0.01	0.00	0.01
Na_2O	0.15	0.14	0.20	0.15	0.24	0.14	0.20	0.18	0.18	0.19	0.18	0.17
K_2O	9.63	9.76	9.50	9.66	9.53	9.49	9.65	9.64	9.59	9.32	9.68	9.49
Total	96.00	96.67	94.01	94.41	95.24	95.01	95.91	95.63	96.49	95.63	95.74	92.56
Oxygens	11.00	11.00	11.00	11.00	11.00	11.00	11.00	11.00	11.00	11.00	11.00	11.00
Si	2.74	2.73	2.74	2.75	2.75	2.73	2.73	2.74	2.74	2.76	2.75	2.76
Ti	0.30	0.30	0.30	0.30	0.30	0.29	0.32	0.31	0.30	0.30	0.31	0.31
Al	1.28	1.28	1.28	1.27	1.29	1.31	1.28	1.27	1.29	1.27	1.27	1.28
Cr	0.03	0.03	0.03	0.03	0.03	0.02	0.03	0.03	0.02	0.03	0.03	0.02
Fe^{3+}	0.00	0.00	0.00	0.00	0.00	0.00	0.00	0.00	0.00	0.00	0.00	0.00
Fe^{2+}	0.84	0.86	0.85	0.86	0.82	0.93	0.88	0.88	0.93	0.89	0.87	0.98
Mn	0.00	0.00	0.00	0.00	0.00	0.00	0.00	0.00	0.00	0.00	0.00	0.00
Mg	1.67	1.65	1.64	1.62	1.65	1.56	1.60	1.61	1.55	1.59	1.60	1.46
Ca	0.00	0.00	0.00	0.00	0.00	0.00	0.00	0.00	0.00	0.00	0.00	0.00
Na	0.02	0.02	0.03	0.02	0.04	0.02	0.03	0.03	0.03	0.03	0.03	0.03
K	0.91	0.92	0.92	0.93	0.90	0.91	0.92	0.92	0.91	0.88	0.92	0.94
Total	7.78	7.78	7.78	7.77	7.77	7.78	7.77	7.78	7.77	7.75	7.77	7.77
X_{Fe}	0.33	0.34	0.34	0.35	0.33	0.37	0.35	0.35	0.38	0.36	0.35	0.40

2.6 Thermobarometry and *P-T* path constraints

Thermobarometry is predicated on the assumption that the modes and compositions of the minerals in an assemblage represent a preserved equilibrium attained at some point on the *P-T* path. Two thermobarometric approaches have evolved in the last twenty years with the inception of rigorous equilibria modelling afforded by software such as THERMOCALC, namely, conventional thermobarometry (e.g., the avPT method in THERMOCALC) and pseudosection thermobarometry (Powell and Holland, 1998; White and Powell 2002; Boger et al., 2003; White et al., 2003; Johnson et al., 2003; Kelsey et al., 2003a; Kelsey et al., 2003b; Johnson et al., 2004; Zeh et al., 2004; Baldwin et al., 2005; White et al., 2005; Hollis et al., 2006; Diener et al., 2007; Halpin et al., 2007). Developments in both these thermobarometric methods have been coupled with major improvements in the thermodynamic data sets of mineral end-members (Holland and Powell, 1996; Berman, 1988; Holland and Powell, 1998; upgrade November 2003) and *a–x* relationships for minerals, silicate liquid and fluid (e.g., Holland and Powell, 1992; Powell and Holland, 1993; Holland and Powell, 1996; Powell and Holland, 1999; Dale et al., 2000; White et al., 2000; Holland and Powell, 2001; White et al., 2001; Holland and Powell, 2003; Dale et al., 2005; Diener et al., 2007). Intrinsic to both thermobarometric techniques is the concept of equilibration volume, i.e., the volume within which the minerals selected for thermobarometry are considered to have been in equilibrium. Constraining the equilibration volume requires a consideration of different length-scales of diffusion for components, the sequestration of components within the cores of growth-zoned porphyroblasts and the extent to which retrograde replacement and chemical zoning unrelated to the peak assemblage has occurred (e.g., White et al., 2008).

Conventional thermobarometric techniques are based on independent balanced reactions between mineral end-members of phases comprising the equilibration volume. For each end-member reaction, an equilibrium relationship of the form $0 = \Delta G° + RT\ln K$ applies, which governs *P*, *T* and phase composition (e.g., Spear and Cheney, 1989; Powell and Holland, 1990; Connolly, 1990; Holland and Powell, 1998). For an assumed equilibrium assemblage, given uncertainties in the compositions and thermodynamic descriptions of the phases, an optimal

thermobarometric estimate of equilibration conditions is given by the *P* and *T* at which the *P–T* lines for the equilibria intersect (Powell & Holland, 1988; Powell & Holland, 1994; Powell et al., 2002; Powell and Holland, 2008). No information regarding the modes of the equilibrium assemblage is available through this method and compositional resetting along the retrograde path commonly obscures peak conditions (Harley, 1989; Fitzsimons and Harley, 1994; Pattison and Begin, 1994; Pattison et al., 2003; Harley, 2008). Moreover, since conventional thermobarometry relies entirely on mineral compositions for *P-T* estimation, results are very sensitive to uncertainties in the probe data and thermodynamic descriptions of the phases considered (Powell and Holland, 2008).

In the last ten years, there has been a gradual shift toward the use of calculated pseudosections for thermobarometry (e.g., Powell and Holland, 1998; White et al., 2002; Boger et al., 2003; White et al., 2003; Johnson et al., 2003; Kelsey et al., 2003a; Kelsey et al., 2003b; Johnson et al., 2004; Zeh et al., 2004; Baldwin et al., 2005; White et al., 2005; Hollis et al., 2006; Diener et al., 2007; Halpin et al., 2007). Pseudosection thermobarometry is a forward modelling approach. A pseudosection quantitatively maps out the stability range of mineral assemblages in *P-T-X* space. For a given composition of the equilibration volume, the position in *P–T* space of the field that corresponds to the equilibrium mineral assemblage, and the proportions and compositions of the minerals in that field, can be modelled (Powell and Holland, 1998; Connolly, 1990; Spear and Cheney, 1989). Since pseudosections do not depend on establishing original mineral compositions (as required for conventional thermobarometers), compositional resetting along the retrograde path does not obscure peak conditions. Unlike conventional petrogenetic grids, the pseudosections are not restricted to only univariant and invariant equilibria, but also constrain multivariant phase equilibria for a unique bulk rock or effective domainal composition. Pseudosections allow the textural evolution of a rock to be assessed by comparing changing mineral modes and compositions predicted in the pseudosection with reaction textures preserved in the rock, thereby allowing sections of the *P-T* path to be deduced (Powell and Holland, 2008).

The difficulty in applying pseudosections to real rocks lies in the selection of the appropriate bulk composition of the equilibration volume. When growth-zoned

minerals such as garnet are present in the rock, a certain proportion of the whole-rock composition is sequestered in the core of the garnet and unavailable for participation in the reactions at higher grades. In this case, the whole-rock composition is different from the composition of the equilibration volume and the components sequestered in garnet cores need to be excluded from the bulk composition for a realistic pseudosection to be constructed (e.g., Marmo et al., 2002). Similarly, during cooling along the retrograde path, the equilibration volume will shrink as diffusion length-scales become shorter at lower temperatures. The equilibration volume composition evolves continuously throughout the metamorphic history of a rock, such that separate pseudosections of unique bulk compositions characterize different portions of the *P*-*T* path.

Mismatch between the modelled assemblages in a pseudosection and the observed assemblage may indicate a slightly inappropriate bulk composition has been used for construction of the pseudosection (Powell and Holland, 2008). A *T*-*X* pseudosection covering the range of plausible bulk compositions may be used to constrain the real equilibration volume composition more accurately. Another cause of inconsistency between modelled and observed equilibria relates to inaccuracies in the thermodynamic models for the phases considered (Powell and Holland, 2008). Thermodynamic models are constantly being refined (e.g., Diener et al., 2007; Green et al., 2007), however inadequacies in current models may cause the failure of models to reproduce the real rock assemblage. Finally, the failure of a pseudosection to accommodate real observations in the rock may be because the model system (e.g., NCKFMASH) does not account for all the components influencing the equilibria (Powell and Holland, 2008). Currently, we are able to model in MnNCKFMASHTO (MnO-Na_2O-CaO-K_2O-FeO-MgO-Al_2O_3-SiO_2-H_2O-TiO_2-Fe_2O_3) as the most complex system, although almost certainly the addition of Zn to the model system will allow more accurate prediction of spinel and staurolite stability in the future. Given these caveats, pseudosection modelling remains the most effective thermobarometric method in constraining not only the *P*-*T* conditions prevailing during equilibration, but also in yielding petrogenetic information embedded in the textural relationships between phases in a rock related to changes in the composition of the equilibration volume, pressure and temperature during the

metamorphic history (e.g., Kelsey et al., 2003; White and Powell, 2002; Stipska et al., 2006).

Previous thermobarometric estimates for peak metamorphism in the Steynskraal-Jagers Vrede rocks employed the use of directly calibrated thermobarometers (Schreyer and Abraham, 1978; Schreyer, 1983; Perchuk et al., 2002) and average *P-T* conventional thermobarometry in THERMOCALC (Stevens et al., 1997b). Schreyer and Abraham (1978) used experimental data from Hensen and Green (1971, 1972, 1973) to constrain conditions of symplectite formation, which they inferred to have occurred late in the granulite event, at 5 kbar and 700 °C. Perchuk et al. (2002) obtained a peak *P-T* estimate for the M_1 assemblage of 700 °C and 5 kbar. Higher temperature estimates of at least 850 °C and potentially in excess of 920 °C were obtained by Stevens et al. (1997b) based on the upper stability limit of biotite, quartz and dry granite melt (Stevens et al., 1997a). Core compositions of garnet, biotite and cordierite gave peak temperatures and pressures between 800 °C, 4.8 ± 0.13 kbar and 900 °C, 5.1 ± 0.16 kbar (Stevens et al., 1997b). The sensitivity of the conventional thermobarometry approach to post-peak compositional re-equilibration has almost certainly resulted in an underestimation of peak temperature and pressure in the case of Schreyer and Abraham (1978) and Perchuk et al. (2002), and poorly constrained temperature estimates of Stevens et al. (1997b). The application of a pseudosection modelling approach, which addresses this problem, is thus likely to yield more rigorous constraints on *P-T* estimates and optimally constrain the *P-T* path through correlation of observed mineral textures with model phase equilibria in *P-T-X* space.

Pseudosection modelling was performed in THERMOCALC 3.25 (Powell and Holland, 1988, update April 2007) and an updated internally consistent dataset of Holland and Powell (data set tcds55, 22 November 2003). The chemical system adopted for phase equilibria modelling of the rocks in this study is Na_2O-CaO–K_2O–FeO–MgO–Al_2O_3–SiO_2–H_2O–TiO_2–Fe_2O_3, i.e., NCKFMASHTO. This is considered to be a good approximation of a natural pelitic rock composition (Powell and Holland, 2008). The *a-x* relationships for solid solution phases are those used by White et al. (2007; new biotite, garnet and liquid models). The omission of Mn from the system raises the garnet-in boundary by 15 - 20 ºC (White et al., 2004). The

absence of Zn in the model chemical system means that the Zn-rich spinel phase in SK6C and SK9-CLM and, potentially, staurolite stability estimates in the model composition, will be compromised. Specifically, the high proportion of gahnite in spinel may well stabilise spinel in a real rock composition that otherwise would be spinel-absent in NCKFMASHTO. The pseudosection modelling was also performed prior to the release of *a-x* models for orthoamphibole and, as such, the low-temperature portions of the pseudosections for the K_2O-depleted compositions modelled are likely to be metastable with respect to orthoamphibole (J. Diener, pers. comm. 2006).

Pseudosection modelling was undertaken on 3 samples: SK4A is a metagreywacke and SK9-CLM and SK6C are metapelites. For each sample, two pseudosections were constructed with different bulk compositions (in mol%). The first pseudosection presented for each sample is based on a bulk composition most appropriate for modelling peak conditions. This was obtained from a representative XRF analysis of the bulk rock with H_2O molar % estimated such that the peak assemblage could be modelled with the observed mineral modes and only a tiny proportion of melt. This working assumption is based on the premise that melt-loss must occur continuously on the prograde path following crossing of the wet solidus in order for the rock to maintain cohesion (White et al., 2005). Since the bulk composition used to construct the peak pseudosection for each sample is, thus, a melt-depleted, restitic one, it is inappropriate to use the same composition to model the prograde path. Unfortunately, there is no unequivocal low-grade analogue down the metamorphic field gradient that can be used to estimate the protolith composition. Despite this, it is still possible to estimate an approximate protolith composition by sequentially reintegrating melt of the appropriate bulk composition back into the peak composition following the method developed by White et al. (2004). Basically, melt reintegration involves adding liquid to the peak bulk composition until the low-temperature boundary of the phase field becomes a peritectic phase-out and not liquid-out point. The peritectic phase-absent, liquid-out point is then calculated and a new predicted bulk composition is obtained. More liquid is added to this new bulk composition until another peritectic phase disappears before liquid, thereby yielding a new bulk composition. This process proceeds until the rock is fluid-saturated at the wet solidus. The second

pseudosection presented for each sample is based upon melt-reintegrated bulk compositions obtained in this manner.

2.6.1 Estimation of peak metamorphic conditions

Melt loss from the equilibration volume plays a crucial role in the preservation of the peak granulite facies assemblage (White and Powell, 2002). White and Powell (2002) quantitatively demonstrated that the loss of a silicate melt into which H_2O has partitioned during dehydration melting effectively removes H_2O from the equilibration volume, thereby preventing re-equilibration of the anhydrous, refractory granulite facies residuum during retrogression. As a consequence, the solidus is substantially elevated in the refractory bulk composition. The coarse-grained textural evolution of the granulite facies assemblage continues until the new elevated solidus is crossed on cooling (White and Powell, 2002). With rapid cooling rates and/or melt loss, diffusion rates may diminish along the suprasolidus retrograde *P-T* path to the extent that intergranular diffusion becomes rate-limiting and corona textures evolve (Chapter 3). This is typical of highly restitic bulk compositions with extreme melt loss. In contrast, more melt-rich granulites will continue to equilibrate both texturally and compositionally until reaction cessation at the solidus (White and Powell, 2002). Below the solidus, in the absence of deformation or melt or water ingression, diffusion rates are too sluggish to effect reaction and the peak assemblage present at the solidus persists metastably to lower temperatures (Diener et al., 2008; White and Powell, 2002).

Estimation of peak metamorphic conditions in granulites is commonly hindered by compositional re-equilibration of minerals during the high-temperature retrograde path (Harley, 1989; Fitzsimons and Harley, 1994; Pattison and Begin, 1994; Pattison et al., 2003; Harley, 2008). This precludes the use of conventional exchange thermobarometers for modelling the peak conditions. Fortunately, mineral modes attained during peak *P-T* conditions are more easily preserved than the mineral compositions such that, with consideration of their textural relationships, it is possible to infer peak conditions directly from a pseudosection calculated for a bulk composition appropriate for those peak conditions (e.g., Hollis et al., 2007).

Moreover, overlapping peak assemblage fields from different pseudosections calculated for a range of compositions may be used to further constrain peak conditions, assuming all samples experienced the same peak pressure and temperature (e.g., Clarke et al., 2007). The contrasting bulk compositions in pelitic and greywacke samples are amenable to this modelling method, particularly where they can be sampled in close proximity to one another, such as is the case for SK6C and SK4A. It is important to appreciate that the peak conditions interpreted from modelled pseudosections represent the point in *P-T* space at which the coarse-grained textural evolution of the rock ceased. The actual peak conditions may well be higher, particularly for melt-rich granulites, but are now obscured by reaction under suprasolidus conditions along the high-temperature portion of the retrograde path. The peak estimates thus represent minimum pressure and temperature constraints for peak (M_1) metamorphism (e.g., Clarke et al., 2007).

SK6C peak conditions

A pseudosection based on a bulk composition appropriate for modelling peak conditions for the metapelitic Sample SK6C is presented in Figure 2.24. According to this, the peak metamorphic assemblage of garnet, cordierite, biotite, plagioclase, K-feldspar, quartz, liquid, ilmenite and rutile is stable from 870 to 890 ºC and 7.1 - 7.9 kbar. The Zn-rich spinel was omitted from the modelled assemblages since this is a minor phase present only as inclusions in cordierite (see Figure 2.7a). Stevens et al. (1997b) identified spinel in contact with quartz included in garnet consistent with the breakdown of spinel-cordierite-quartz assemblages to garnet-sillimanite-quartz assemblages in pelitic bulk compositions at low pressures in FMASH (Figure 1.10; Waters, 1991). The inclusion of these phases in garnet suggested the reaction must have been crossed on the prograde path prior to peak conditions and, accordingly, they inferred an anti-clockwise *P-T* path based on this texture. However, detailed petrographic examination of over 50 thin sections in this study conclusively established the absence of spinel in contact with quartz and inclusion exclusively in cordierite. Increasingly, limited petrological significance is attached to spinel inclusions in cordierite (pers. comm. J. Diener, 2007). They may have formed when staurolite was included along the prograde path within cordierite (demonstrated in

prograde pseudosections, Figure 2.34). This would have created a locally silica-undersaturated compositional enclave in a rock otherwise containing free quartz. As a consequence, with increasing T, the staurolite would have then reacted with the cordierite to form spinel independently of the silica-saturated equilibria prevailing in the bulk of the rock. Evidence for this scenario would be the measured elevated Zn levels in the spinel (Tables 2.4d, 2.5d), as Zn is preferentially sequestered in staurolite as it reaches its upper stability limit (e.g., Stoddard, 1979).

The peak assemblage phase field in the SK6C pseudosection is contoured for X_{Fe} for garnet, biotite and cordierite in Figure 2.25. Measured garnet X_{Fe} values in the sample range from 0.53 to 0.67; cordierite X_{Fe} ranges from 0.11 to 0.17 and biotite X_{Fe} ranges from 0.24 to 0.32 (Section 2.5). The region in *P*-*T* space of compositional overlap between garnet and biotite X_{Fe} is from 870 - 880 ºC and 7.1 - 7.6 kbar. Cordierite is more Fe-rich in the modelled pseudosection (0.17 to 0.21) than observed in the rock. More magnesian cordierite compositions are predicted in the pseudosection (0.17 - 0.18) toward the higher-temperature, higher-pressure margin of the peak phase field, matching observed cordierite rim compositions; however, measured cordierite core compositions are too magnesian for this phase field (0.11 - 0.14). Potentially, the magnesian compositions of the cordierite cores could imply that marginally higher peak temperatures and pressures may have been attained in this rock but that these have been largely obscured by re-equilibration and back-reaction with melt immediately post-peak along the high-temperature retrograde path.

More reliable constraints on peak conditions for Sample SK6C are rendered by a pseudosection contoured for mineral mol% of garnet, biotite and cordierite (Figure 2.26). Mineral modal analysis of thin sections from SK6C yielded a mineral modal proportion estimate of garnet of 0.25 - 0.35, biotite of 0.10 - 0.15 and cordierite of < 0.05, consistent with a range of modelled mineral modes from 870 - 880 ºC and 7.1 - 7.9 kbar. Probable minimum peak conditions based on correlated measured and modelled mineral modes within the peak phase field are at 875 °C and 7.4 kbar, indicated by the black circle in Figure 2.26.

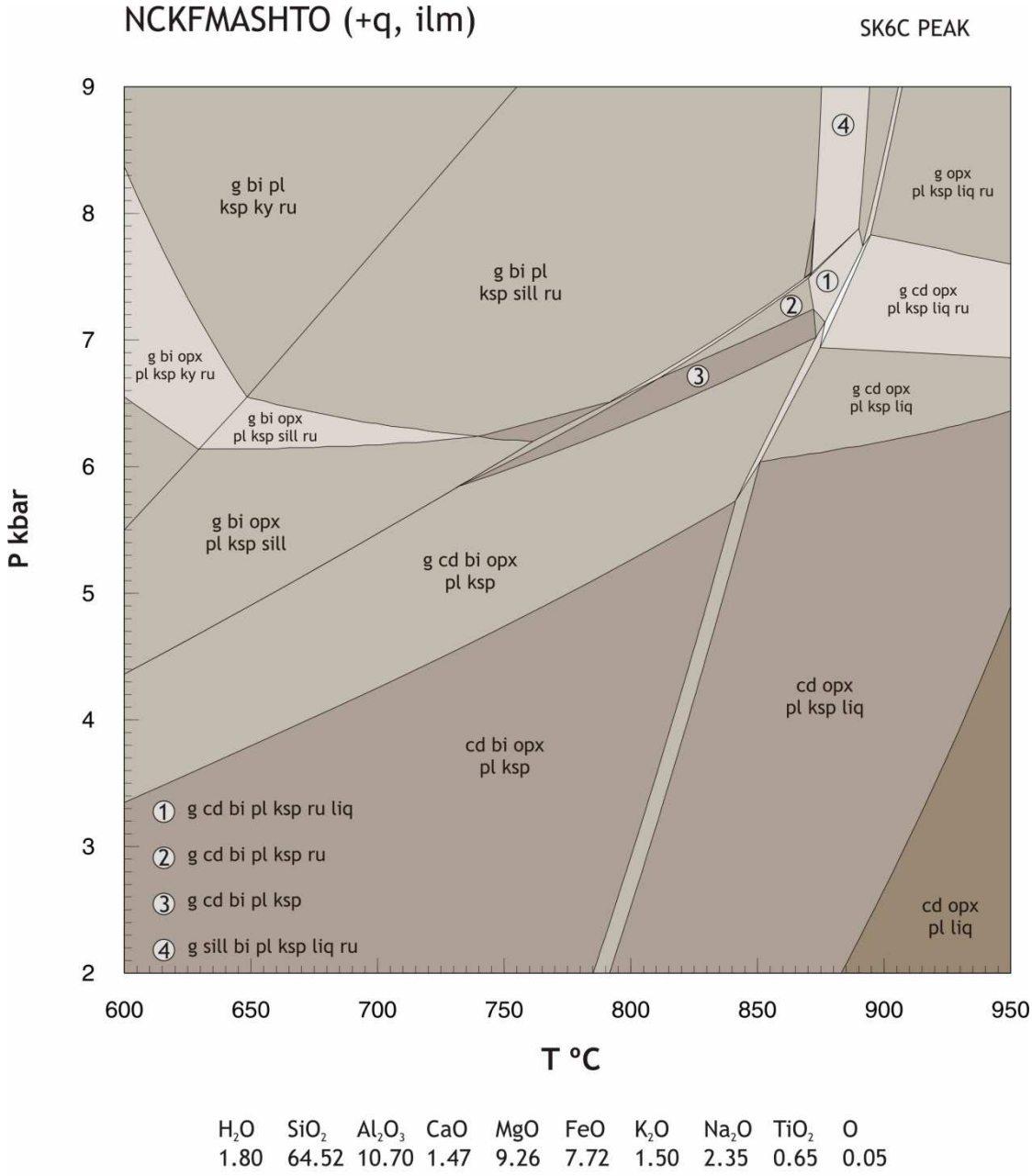

Figure 2.24: P-T pseudosection constructed for SK6C peak metamorphic conditions. Mineral abbreviations are those used conventionally in THERMOCALC. The peak metamorphic assemblage of garnet, cordierite, biotite, plagioclase, K- feldspar, quartz, liquid, ilmenite and rutile is stable from 870 to 890 ºC and 7.1 - 7.9 kbar (Field 1).

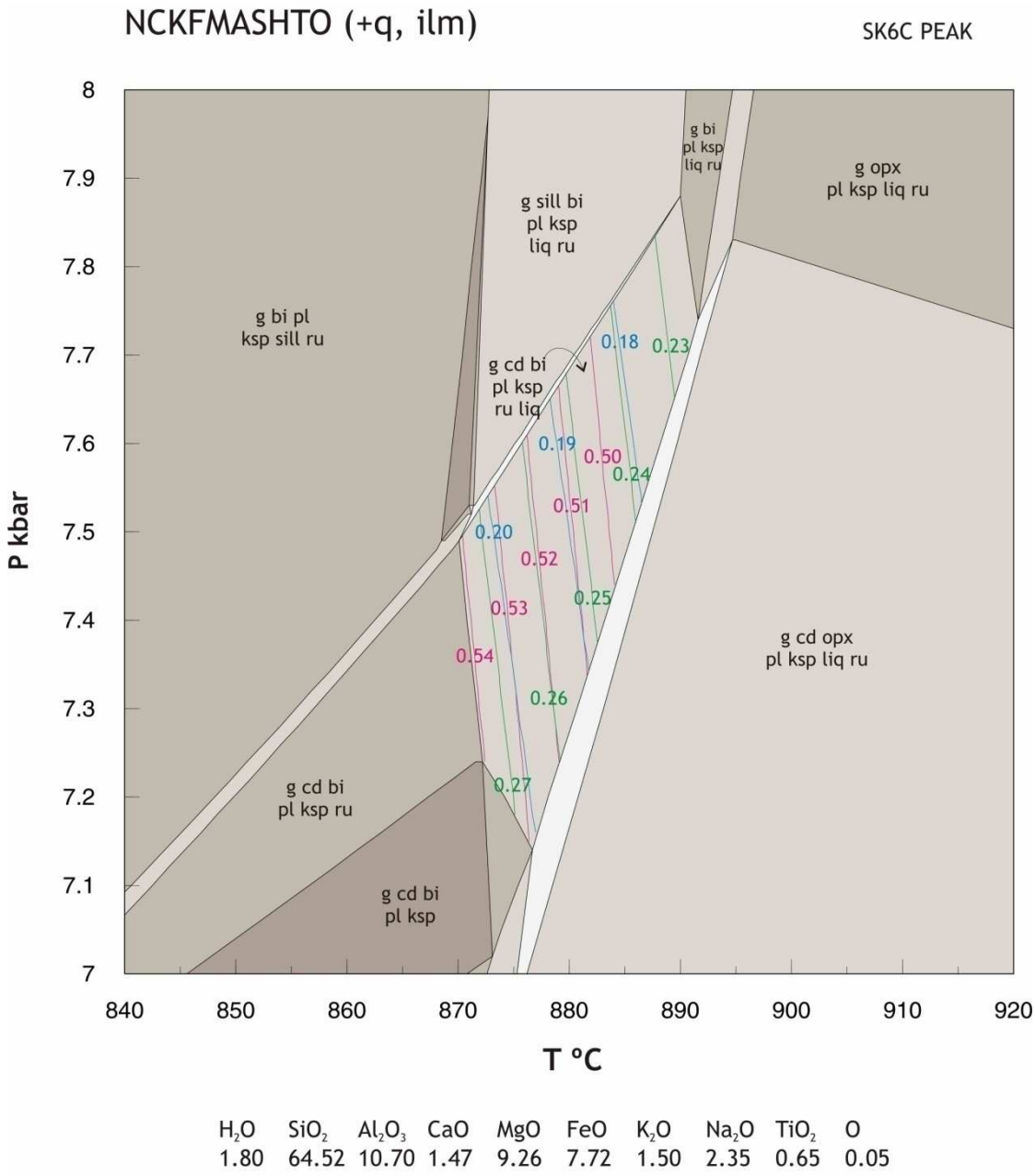

Figure 2.25: P-T pseudosection constructed for SK6C peak metamorphic conditions, contoured for X_{Fe} of garnet (red isopleths), biotite (green isopleths) and cordierite (blue isopleths). Mineral abbreviations are those used conventionally in THERMOCALC.

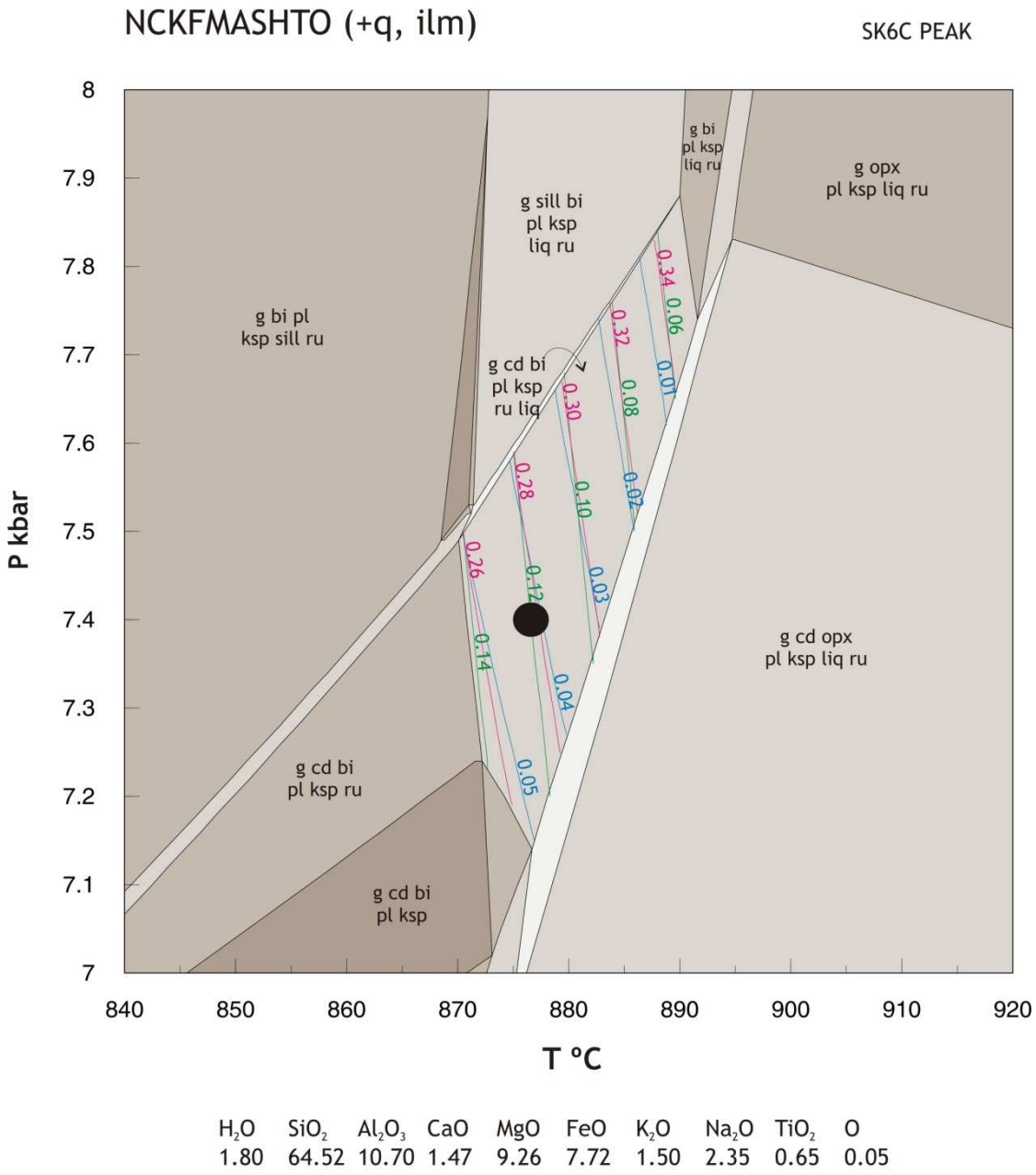

Figure 2.26: P-T pseudosection constructed for SK6C peak metamorphic conditions, contoured for mineral modes of garnet (red), biotite (green) and cordierite (blue). Mineral abbreviations are those used conventionally in THERMOCALC. Observed mineral modal proportions of garnet (0.25 - 0.35), biotite (0.10 - 0.15) and cordierite (< 0.05) are consistent with a range of modelled mineral modes from 870 - 880 ºC and 7.1 - 7.9 kbar. Probable minimum peak conditions based on correlated measured and modelled mineral modes within the peak phase field are at 875 °C and 7.4 kbar, indicated by the black circle.

SK9-CLM peak conditions

Peak conditions for Sample SK9-CLM have been modelled in a pseudosection with a peak bulk composition shown in Figure 2.27. This bulk composition is more calcic and sodic compared to SK6C, manifesting as higher modelled modes of plagioclase in all phase fields. SK9-CLM is slightly more Fe-rich (X_{Mg} = 0.52) than SK6C (X_{Mg} = 0.55). Molar oxygen is higher in SK9-CLM (0.12) compared to SK6C (0.05), as required to stabilize ilmenite without rutile in the peak assemblage (White et al., 2000). The solidus is around 5 °C higher in SK6C compared to SK9-CLM for all pressures modelled. Near-coincident solidi in *P-T* space imply that retrogression for both SK6C and SK9-CLM would have ceased at the solidi within the same *T* range (White et al., 2002).

In Sample SK9-CLM the peak assemblage of garnet, cordierite, biotite, plagioclase, K-feldspar, quartz, liquid, and ilmenite is stable from 865 to 885ºC and 7.0 - 7.7 kbar (Figure 2.27). Figures 2.28 and 2.29 are magnified views of the peak assemblage field contoured for X_{Fe} and modes of garnet, cordierite and biotite, respectively. The measured compositions of garnet (X_{Fe} = 0.68 - 0.83), cordierite (X_{Fe} = 0.19 - 0.27) and biotite (X_{Fe} = 0.38 - 0.54) reported in Section 2.5 are significantly more Fe-rich than the predicted compositions for garnet (X_{Fe} = 0.50 - 0.55), cordierite (X_{Fe} = 0.19 - 0.21) and biotite (X_{Fe} = 0.25 - 0.28). This disparity in mineral compositions demonstrates the problem in using compositional data to constrain peak conditions. Since the difference in solidus temperatures for SK9-CLM and SK6C across the pressure range modelled is within 5 - 10 °C (compare Figures 2.24 and 2.26), arrested reaction for the post-impact event will occur at essentially the same temperature (see Chapter 6), eliminating bulk composition as a control on extent of post-impact reaction. Rather, a greater degree of reaction overstepping closer to the core of the Dome at higher post-impact temperatures must be invoked to explain the more extensive replacement of garnet by symplectite in SK9-CLM and consequent re-equilibration to higher X_{Fe} post-impact phase compositions. By comparison, corona development in SK6C is negligible owing to post-impact temperatures having been lower and re-equilibration at post-impact conditions more inhibited. Thus, mineral modes in SK9-CLM, once corrected for post-impact pseudomorphic replacement, are considered to be more definitive of

peak conditions than mineral compositions. Mineral modal analysis of thin sections from SK9-CLM yielded a mineral modal proportion estimate of garnet of 0.30 - 0.40, biotite of 0.10 - 0.15 and cordierite < 0.05, consistent with a range of modelled mineral modes from 870 - 880 ºC and 6.9 - 7.6 kbar (Figure 2.29). Probable minimum peak conditions are at 878 °C and 7.45 kbar, indicated by the black circle in Figure 2.29.

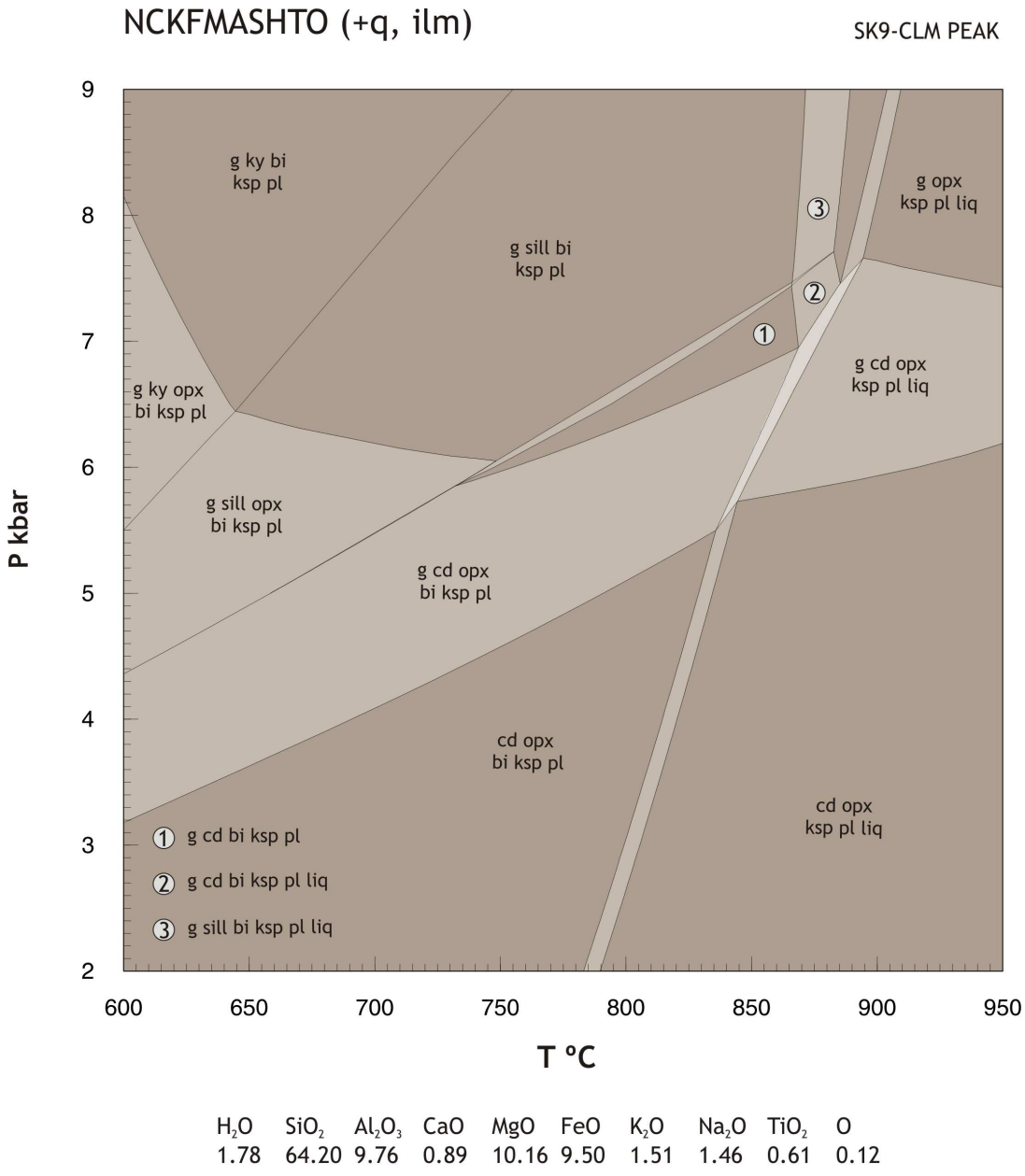

Figure 2.27: P-T pseudosection constructed for SK9-CLM peak metamorphic conditions. Mineral abbreviations are those used conventionally in THERMOCALC. The peak assemblage of garnet, cordierite, biotite, plagioclase, K-feldspar, quartz, liquid, and ilmenite is stable from 865 to 885ºC and 7.0 - 7.7 kbar (Field 2).

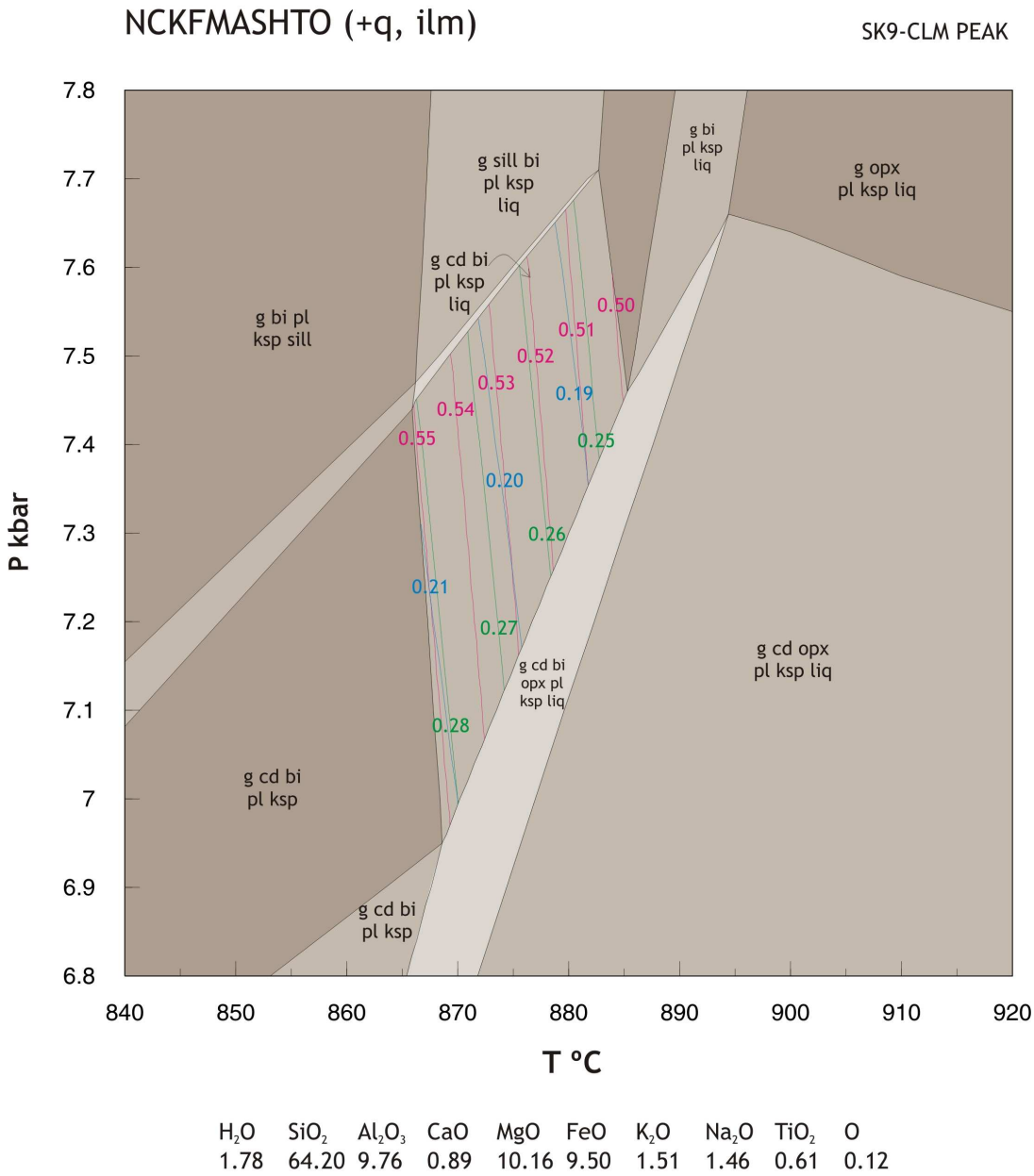

Figure 2.28: P-T pseudosection constructed for SK9-CLM peak metamorphic conditions, contoured for X_{Fe} of garnet (red isopleths), biotite (green isopleths) and cordierite (blue isopleths). Mineral abbreviations are those used conventionally in THERMOCALC.

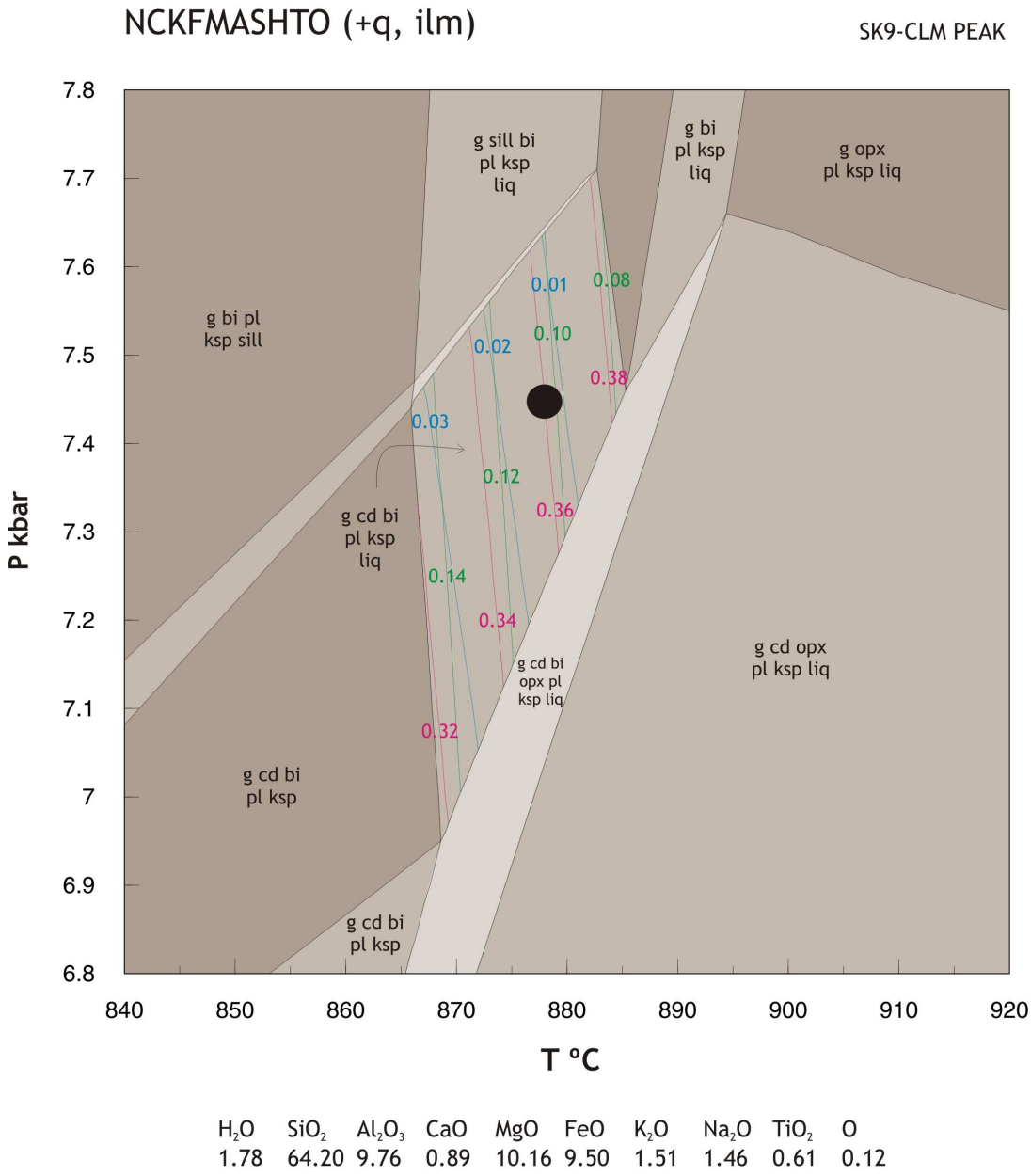

Figure 2.29: P-T pseudosection constructed for SK9-CLM peak metamorphic conditions, contoured for mineral modes of garnet (red), biotite (green) and cordierite (blue). Mineral abbreviations are those used conventionally in THERMOCALC. Observed mineral modal proportions of garnet (0.30 - 0.40), biotite (0.10 - 0.15) and cordierite (< 0.05) are consistent with a range of modelled mineral modes from 870 - 880 ºC and 6.9 - 7.6 kbar. Probable minimum peak conditions are at 878 °C and 7.45 kbar, indicated by the black circle.

SK4A peak conditions

The pseudosection for the metagreywacke Sample SK4A is presented in Figure 2.30. The association of matrix biotite mantling orthopyroxene in this sample suggests biotite replaces orthopyroxene during back-reaction with a melt on the high temperature retrograde path before reaction is arrested at the solidus. Johnson et al. (2008) modelled melt loss and retrograde evolution of metagreywackes and similarly attributed the occurrence of biotite after orthopyroxene to limited retrogression and back-reaction with 10 mol% of the melt initially generated at peak conditions. Accordingly, the observed assemblage in SK4A is representative of the *minimum* peak conditions attained, i.e., the conditions under which the coarse-grained evolution of the rock ceased. Actual peak conditions are likely to have been higher, approaching the *P-T* conditions of SK6C sampled in close proximity to SK4A. If biotite is omitted from the assemblage, the inferred peak phase field comprising garnet-orthopyroxene-K-feldspar-plagioclase-ilmenite-melt-quartz is a high variance field with a broad *P-T* range.

Figures 2.31 and 2.32 are magnified views of suprasolidus assemblage fields contoured for X_{Fe} in garnet, orthopyroxene and biotite, y(Opx) and mineral modes, respectively. The observed mineral modes and X_{Fe} of garnet and biotite are consistent with equilibration in the garnet-biotite-orthopyroxene-plagioclase-K-feldspar-liquid-ilmenite-quartz field. Compositions and modes are consistent with extensive re-equilibration on the high-temperature retrograde path and back-reaction with a melt, such that the coarse-grained assemblage evolution persisted under post-peak conditions. The observed mineral assemblage equilibrated at a lower temperature than the SK6C and SK9-CLM assemblages. The closely spaced isopleths encountered on the retrograde *P-T* path in the garnet-biotite-orthopyroxene-K-feldspar-plagioclase-liquid-ilmenite field (Figure 2.32) suggest biotite grew rapidly over a short interval on the *P-T* path, consistent with the high proportion of coarse-grained retrograde biotite observed. Mineral modal analysis of thin sections from SK4A yielded a mineral modal proportion estimate of garnet of ~ 0.25, biotite of 0.05 - 0.10 and orthopyroxene of ~ 0.15, consistent with probable minimum peak conditions of 858 °C and 7.1 kbar, indicated by the black circle in Figure 2.32. Notably, the absence of cordierite in the assemblage means that the *P-T*

path did not involve significant suprasolidus decompression below 6 kbar (Figure 2.32).

Disparity exists between the predicted X_{Fe} and y(Opx) of orthopyroxene and the observed values from microprobe analysis. In essence, orthopyroxene is more magnesian ($X_{Fe} \sim 0.4$) than the predicted X_{Fe} of orthopyroxene ($X_{Fe} \sim 0.45$), and less aluminous ($0.09 < y(Opx)_1 < 0.13$) than predicted orthopyroxene compositions ($0.15 < y(Opx) < 0.22$) derived from the pseudosection. This difference is too large to be accounted for by error in the microprobe analysis. Moreover, any attempt to modify the bulk composition of the rock to produce the modelled orthopyroxene compositions has failed to reproduce both the modes and the garnet and biotite compositions. Three possible sources of error may account for the discrepancy (Harley, 2008; Kelsey et al., 2003b). Firstly, ferric iron in orthopyroxene may have been over-estimated though recalculation. The presence of Fe^{3+} decreases the amount of Al attributed to the Tschermaks' component and increases the X_{Mg} of the orthopyroxene (Harley, 2008). Secondly, uncertainty may arise because of the different formulations of y(Opx) from probe analyses. Two methods are commonly applied (Pattison et al., 2003): $y(Opx)_1 = c_{Al,total}(Opx)/2$ and $y(Opx)_2 = c_{Si,total}(Opx) + c_{Al,total}(Opx) - 2$, where c_i is cations of component i. The former assumes equipartitioning of Al between octahedral and tetrahedral sites and commonly results in higher values. The latter is thought to better account for the possible presence of Fe^{3+}. The final source of error may arise in the predicted compositions in THERMOCALC owing to uncertainties in the thermodynamic data set (Holland and Powell, Nov 2003). The calculated uncertainties for y(Opx) for the peak pseudosection for SK4A are ± 0.02 (2σ) for y(Opx) and 0.03 for X_{Mg}, bringing the predicted and observed closer to agreement. These are minimum uncertainties based only on the uncertainty for enthalpy propagated through the calculations (Richard White, pers. comm. 2008). Actual uncertainties in the THERMOCALC predicted compositions may well be higher.

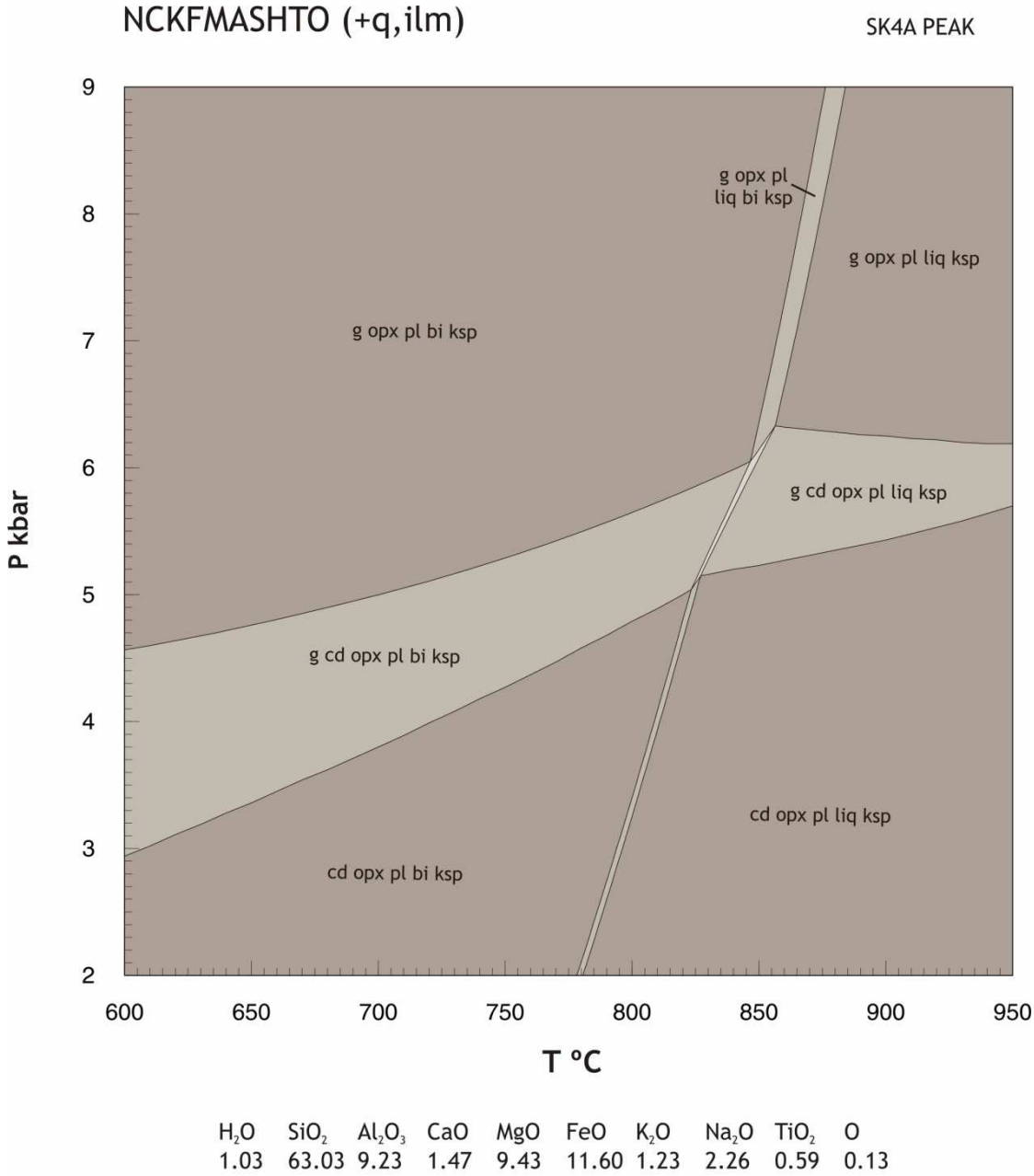

Figure 2.30: P-T pseudosection constructed for SK4A peak metamorphic conditions. Mineral abbreviations are those used conventionally in THERMOCALC.

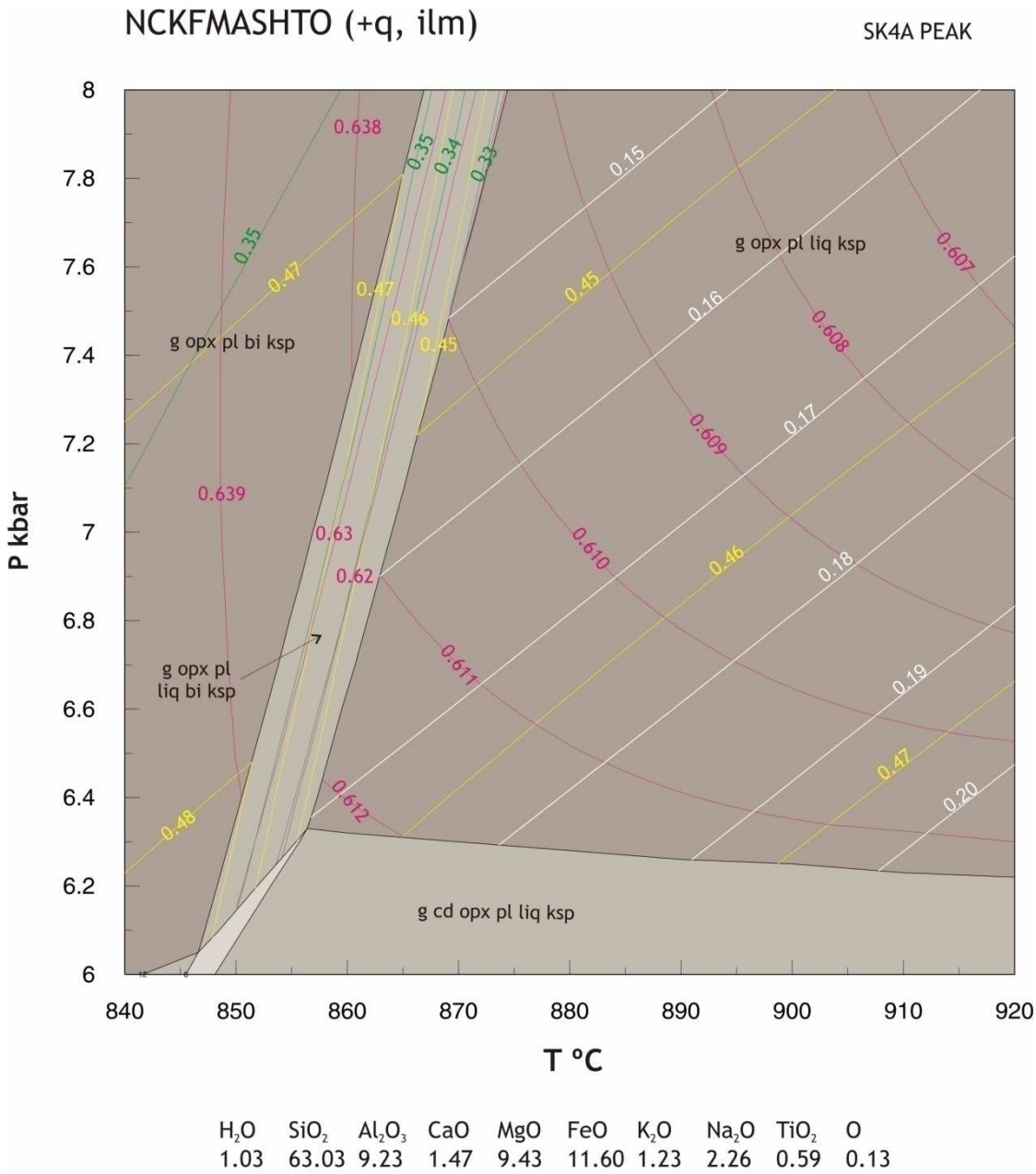

Figure 2.31: P-T pseudosection constructed for SK4A peak metamorphic conditions, contoured for X_{Fe} of garnet (red isopleths), biotite (green isopleths) and orthopyroxene (yellow isopleths). White isopleths represent y(Opx) of orthopyroxene. O in the bulk composition corresponds to 0.006 Fe^{3+} cations in orthopyroxene in the g-opx-pl-liq-ksp-ilm-q assemblage. Mineral abbreviations are those used conventionally in THERMOCALC.

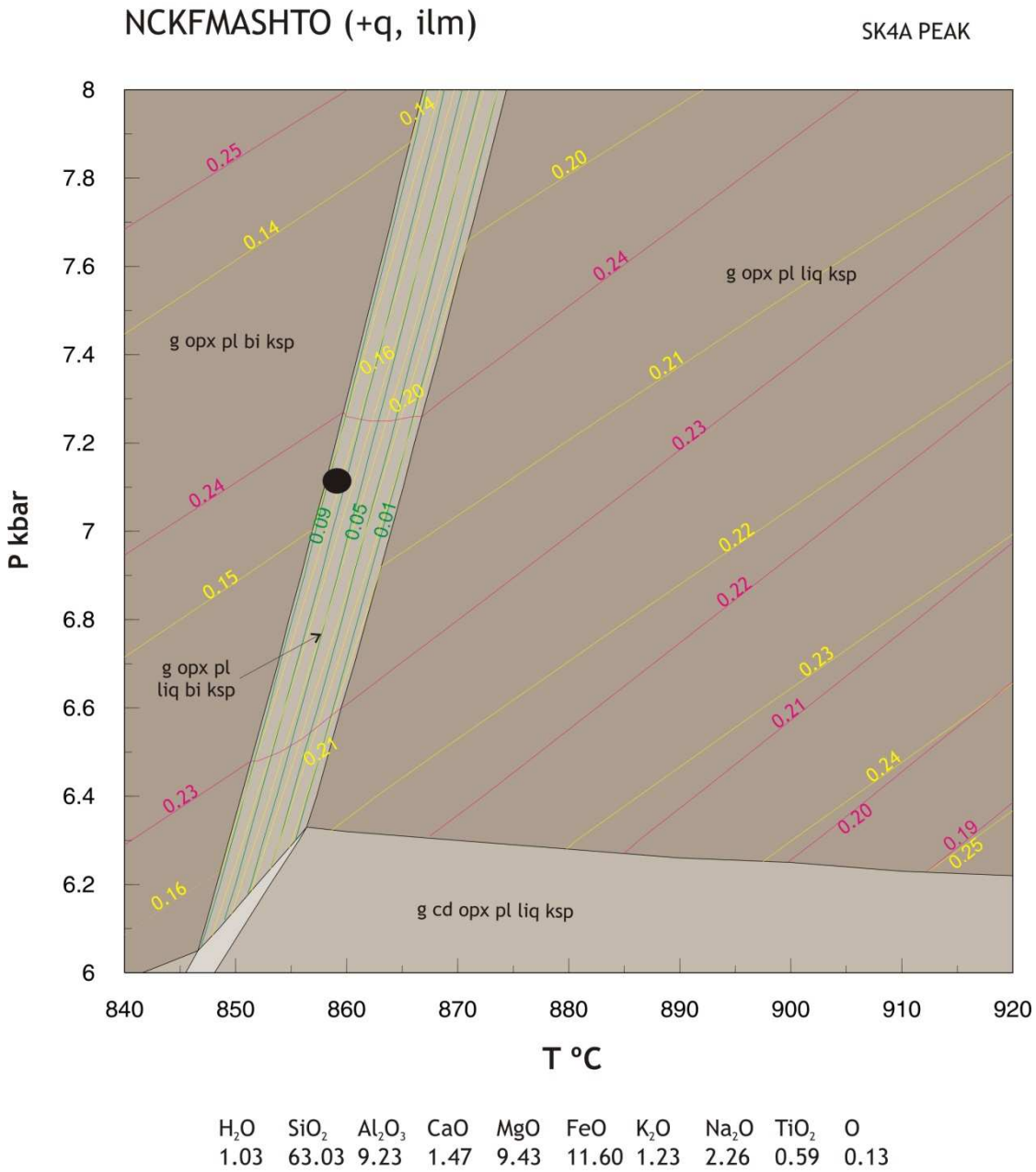

Figure 2.32: P-T pseudosection constructed for SK4A peak metamorphic conditions, contoured for mineral modes of garnet (red), biotite (green) and orthopyroxene (yellow). Mineral abbreviations are those used conventionally in THERMOCALC. Observed mineral modal proportions of garnet (0.25), biotite (0.05 - 0.10) and orthopyroxene (0.15), consistent with probable minimum peak conditions of 858 °C and 7.1 kbar, are indicated by the black circle.

Peak conditions for the Steynskraal traverse

In Figure 2.33, the peak assemblage fields from the 3 pseudosections described above are combined. Minimum peak conditions for SK9-CLM, SK6C and SK4A are represented by red, blue and green circles, respectively, in Figure 2.33. Samples SK6C and SK9-CLM are separated spatially by 3 km along the Steynskraal traverse, suggesting a maximum of ~1 kbar difference in true peak pressures if the section exposed in the Steynskraal traverse is a vertical section through the crust prior to doming, i.e., an on-end section. In reality, the Steynskraal traverse represents an oblique section though the crust given the gradual reduction in rotation of Archaean fabrics observed by Lana et al. (2003b) toward the centre of the Dome. The fact that we do not see higher pressures and temperatures in SK9-CLM compared to SK6C may be because the pressure and temperature difference between the two samples prior to doming along the oblique crustal section was not significant.

Another reason for the lack of distinction between SK6C and SK9-CLM *P-T* conditions may relate to the capacity of a rock to preserve the peak assemblage if melt is not completely lost from the equilibration volume. If melt is present, the textural evolution of these rocks does not cease at the true peak conditions and reaction continues under suprasolidus conditions along the high temperature retrograde *P-T* path until the solidus is crossed. Solidi for SK9-CLM and SK6C are near-coincident in *P-T* space. Hence, the retrograde textural evolution for both samples would have ceased at similar *P-T* conditions, even though actual peak conditions may well have been higher for SK9-CLM. However, given the restitic nature of the pelitic rock bulk compositions, corona textures around garnet would likely have formed on the suprasolidus retrograde path if actual peak conditions were much higher (e.g., Hollis et al., 2007; Chapter 3). The absence of these M_1 coronas suggests that, despite the limited capacity for SK9-CLM and SK6C to preserve distinct maximum peak assemblages, owing to near-coincident solidi in *P-T* space, it is unlikely that the actual *P-T* path proceeded to significantly higher *P-T* conditions than those indicated by the preserved minimum peak assemblage in SK6C and SK9-CLM at present. The region in *P-T* space where peak phase fields for SK6C and SK9-CLM overlap (grey area, Figure 2.33), constrains the minimum peak conditions attained for the entire traverse between 870 - 885 ºC and 7.1 - 7.7

kbar. This supports the notion that the difference in depth of burial at the time of metamorphism was negligible, i.e., the Steynskraal traverse represents a very oblique section thought the crust, in which peak *P-T* differences between SK4A, SK6C and SK9-CLM are negligible.

The lateral separation of SK4A and SK6C (~ 500 m) along the Steynskraal traverse would equate to a maximum pressure difference prior to doming of < 0.2 kbar if the Steynskraal traverse is a vertical section through the crust. Given the likelihood of an oblique section through the crust (Lana et al., 2003b), the difference in peak pressure estimates between SK6C and SK4A are confidently ascribed to variation in melt loss and capacity to preserve the peak assemblage. Since melt loss was not as extensive in SK4A compared to SK6C or SK9-CLM (Section 2.6.2), the solidus is comparatively more depressed in *P-T* space (Figure 2.30). SK4A, thus, had a greater capacity to record conditions on the retrograde path, since reaction would have ceased at lower temperatures for a given pressure on crossing the solidus compared to SK6C and SK9-CLM. Post-peak equilibration occurred for a protracted portion of the immediate retrograde path in SK4A to lower pressures (7.1 kbar) and temperatures (~ 860 °C) with the development of biotite after peak garnet and orthopyroxene, indicating a decompression-cooling path.

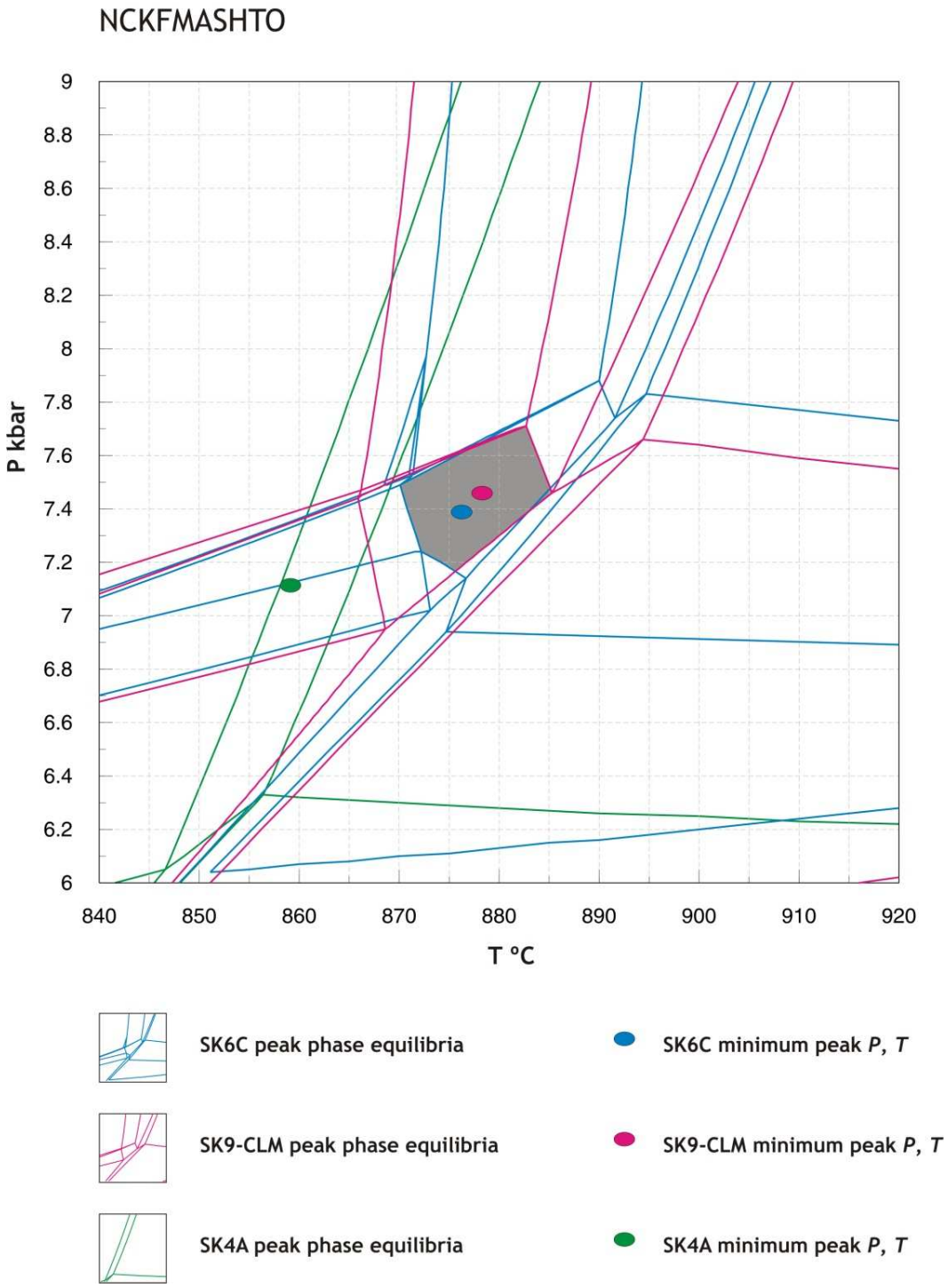

Figure 2.33: Combined reaction equilibria from peak pseudosections for SK4A, SK6C and SK9-CLM. Overlap between phase fields in which the minimum peak assemblages of SK6C and SK9-CLM are produced defines the minimum peak conditions attained for the entire traverse. The absence of M_1 corona textures in SK9-CLM and SK6C suggests the P-T path did not significantly exceed these minimum P-T conditions.

2.6.2 Prograde metamorphic evolution

Pseudosections based on melt-reintegrated bulk compositions using the technique of White et al. (2004) were used to characterise the prograde *P-T* path for samples SK6C, SK9-CLM and SK4A. Melt reintegration for SK6C and SK9-CLM required, respectively, the reintegration of 19 modal melt % and 21 modal melt % of appropriate composition to the measured whole-rock compositions to yield the estimated protolith compositions at the wet granite solidus. In SK4A, 16 modal melt % of appropriate composition was reintegrated back into the measured peak bulk composition. The modal melt % lost from the equilibration volumes was compared with predicted melt modes in the melt-reintegrated bulk composition at peak conditions. Accordingly, melt loss is estimated at ~ 78% in SK9-CLM, ~ 82% in SK6C and ~ 52% in SK4A. The lower proportion of melt loss in SK4A compared with SK6C and SK9-CLM is consistent with textural evidence of a greater extent of retrograde suprasolidus re-equilibration in SK4A. Pseudosections for the estimated protolith compositions for SK6C, SK9-CLM and SK4A are in Figures 2.34, 2.35, and 2.37, respectively.

Prograde reaction textures are best developed in the metapelites, SK6C and SK9-CLM. In these samples, biotite, cordierite (usually with spinel) and sillimanite are included in garnet. Aggregates of spinel and Fe-rich cordierite now pseudomorph sillimanite inclusions within peak cordierite-biotite seams. Although sillimanite is completely pseudomorphed by spinel and cordierite, its presence may be inferred from the extreme elongation of the aggregates and the presence of sillimanite inclusions in garnet, some of which show partial replacement by similar aggregates. A pseudosection for an estimated SK6C protolith composition was constructed (Figure 2.34). Similarly, a melt-reintegrated pseudosection for SK9-CLM is presented in Figure 2.35. Unlike the peak pseudosections, in melt-reintegrated pseudosections melt-bearing fields are stable to the wet solidus. The sillimanite-out line has a flat topology above the wet solidus, and restricts the prograde sillimanite-cordierite-biotite-bearing prograde assemblages to a thin field between 6.5 and 7.5 kbar from 700 to 850 ºC in both SK6C (Figure 2.34) and SK9-CLM (Figure 2.35). A prograde *P-T* path dominated by heating with little or no change in pressure is

inferred from these inclusion relationships and is indicated by the dot-dashed lines in Figure 2.34 and 2.35.

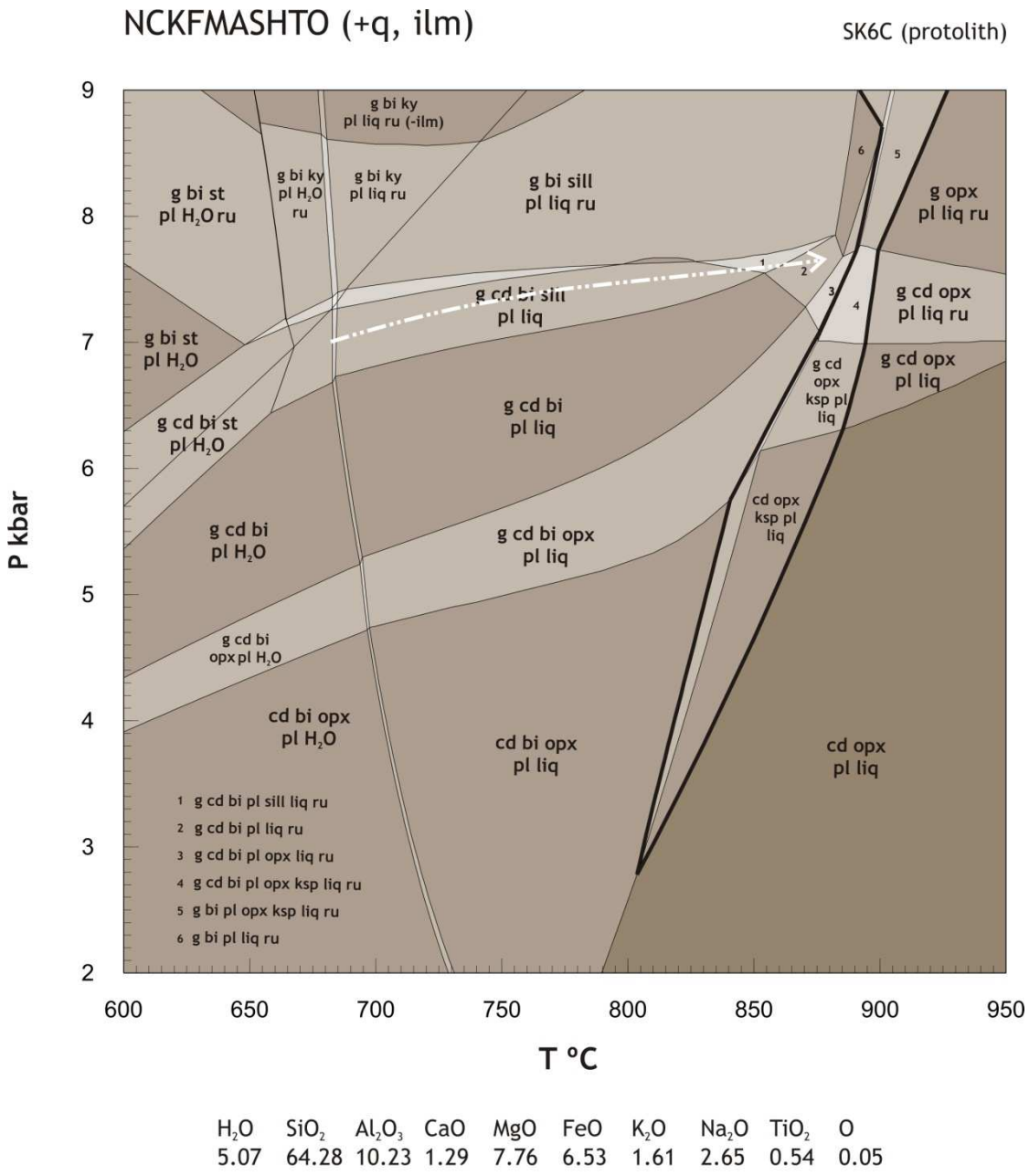

Figure 2.34: P-T pseudosection constructed for SK6C prograde metamorphic evolution based on an estimated protolith composition. The presence of sillimanite and cordierite inclusions in garnet restricts the prograde evolution to a narrow multivariant field comprising garnet-cordierite-biotite-sillimanite-ilmenite-quartz-liquid. A potential prograde path is indicated by the white, dot-dashed line. The K-feldspar-in line is delineated by the bold line. Mineral abbreviations are those used conventionally in THERMOCALC.

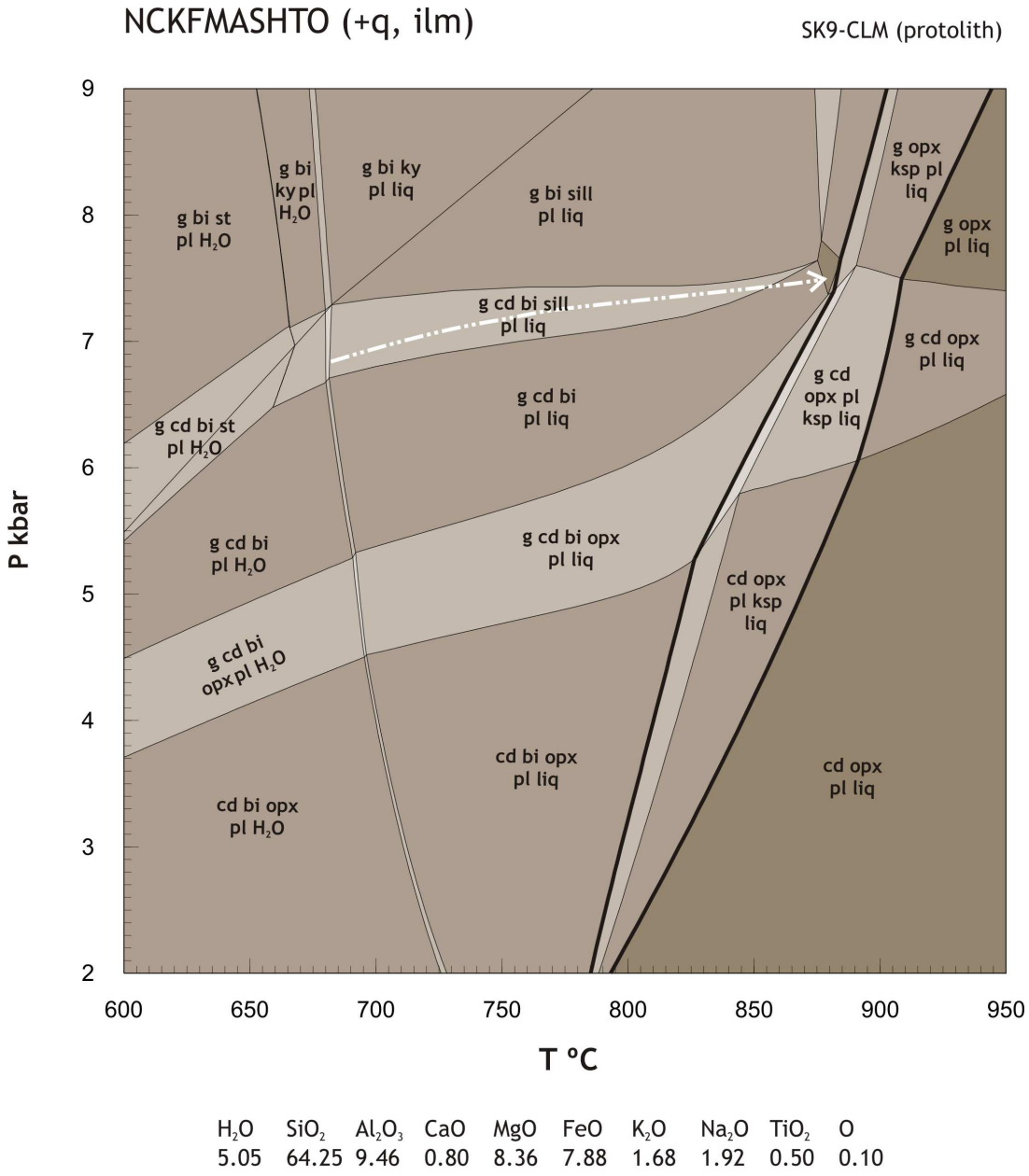

Figure 2.35: P-T pseudosection constructed for SK9-CLM prograde metamorphic evolution based on an estimated protolith composition. A potential prograde path is indicated by the white, dot-dashed line. The K-feldspar-in line is delineated by the bold line. Mineral abbreviations are those used conventionally in THERMOCALC.

The peak assemblage for both SK6C and SK9-CLM cannot be accommodated in the melt-reintegrated pseudosections, i.e., a peak assemblage comprising garnet, cordierite, biotite, K-feldspar, plagioclase, ilmenite, quartz and liquid does not constitute an equilibrium phase field in the prograde pseudosections (Figures 2.34, 2.35). K-feldspar is not stable along the prograde path in *P*-*T*-*X* space for both SK6C and SK9-CLM protolith compositions and only occurs in orthopyroxene-bearing rocks of these compositions at temperatures in excess of 850 °C (Figures 2.34, 2.35). The K-feldspar-in line for both SK6C and SK9-CLM pseudosections is indicated by a bold solid line (Figures 2.34, 2.35). Since K-feldspar is, in fact, present in the peak assemblage for both SK6C and SK9-CLM, the protolith composition is not appropriate to model the high-temperature portion of the *P*-*T* path. This is because the protolith composition evolves to a more restitic bulk composition as melt is progressively lost along the prograde path. Melt reintegration for SK6C reveals that 14 modal melt % must have been lost from the protolith composition to stabilize K-feldspar at 857 ºC and 7.3 kbar in a drier, more restitic, bulk composition.

A *T*-*X* pseudosection was constructed for SK9-CLM (Figure 2.36) to demonstrate the effect of melt loss on the prograde assemblage along a prograde path at 7 kbar. The *X*-axis tracks from a melt-reintegrated protolith composition at $X = 0.0$ to the peak, restitic, bulk composition at $X = 1.0$. The compositional range corresponds to a total melt loss of 78%. The K-feldspar-in line is the black bold line in Figure 2.36. K-feldspar is not stable in the protolith bulk composition below the solidus at $X < 0.80$ (i.e., 63 % melt loss). The dot-dashed line in Figure 2.36 represents a potential prograde path for SK9-CLM through *T*-*X* space, assuming continuous melt loss. Sillimanite is included in garnet during the low-temperature portion of the prograde path, but is unstable as temperature increases and melt loss proceeds, such that sillimanite is preserved only as inclusions in cordierite and garnet and not as part of the peak assemblage. During the high-temperature segment of the prograde path (dot-dash line), greater than 55% melt must be lost from the equilibration volume ($X > 0.69$) to stabilise K-feldspar in the melt-depleted assemblage above the solidus in SK9-CLM. The presence of K-feldspar in SK6C and SK9-CLM is, thus, indicative of melt loss.

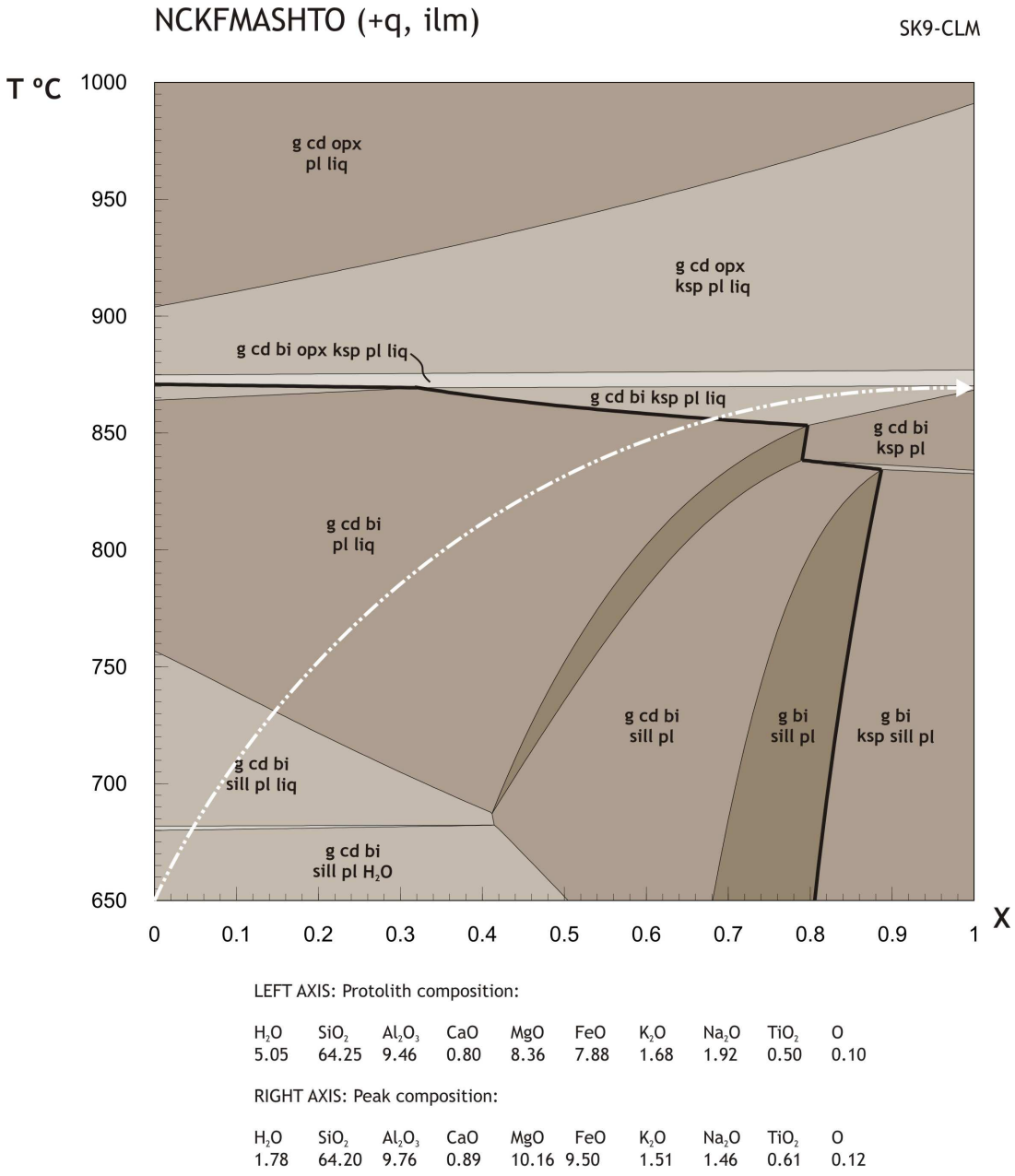

Figure 2.36: T-X pseudosection for SK9-CLM demonstrating the effect of melt loss on the equilibrium phase assemblage. The K-feldspar-in line is indicated by the black bold solid line. A potential prograde path is indicated by the white dot-dashed line. Sillimanite is included in garnet during the low-temperature portion of the prograde path. K-feldspar is only stable in the assemblage at suprasolidus conditions, with melt loss in excess of X = 0.69 (55%) and temperature > 850 °C. Mineral abbreviations are those used conventionally in THERMOCALC.

In the metagreywacke SK4A, garnet is partly enclosed by orthopyroxene, but never the other way around. This is consistent with a prograde *P-T* path constrained by the pelitic rocks SK6C and SK9-CLM, tracking through the multivariant phase field

where both garnet and orthopyroxene are stable on a trajectory that ensures that the orthopyroxene mode increases whilst garnet mode decreases (Figure 2.37).

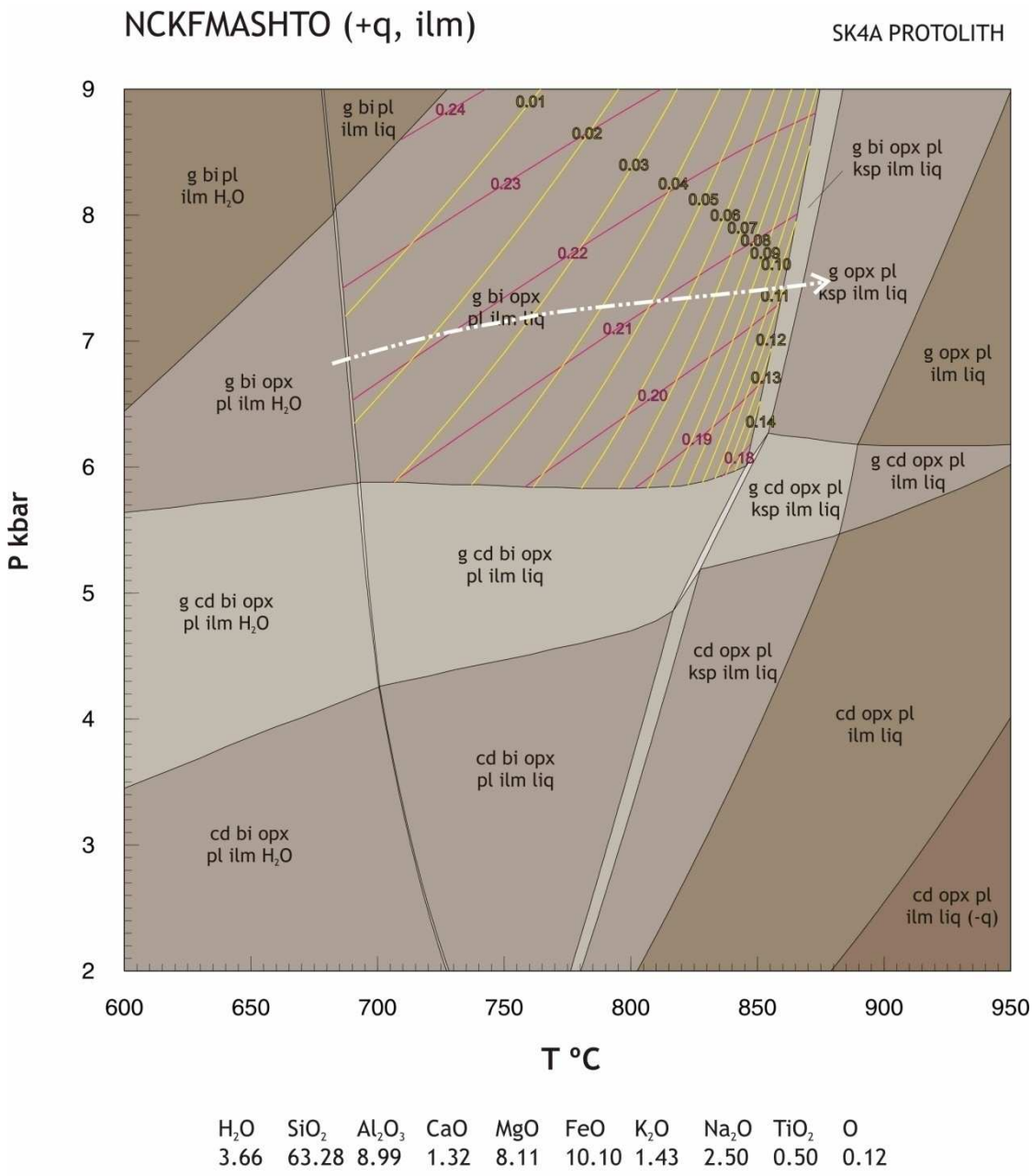

Figure 2.37: P-T pseudosection constructed for SK4A prograde metamorphic evolution based on an estimated protolith composition and contoured for mineral modes of garnet (red) and orthopyroxene (yellow). The potential prograde path for metapelites (SK6C and SK9-CLM) is superimposed on the grid (white dot-dashed line). The mode of orthopyroxene increases whilst garnet decreases, consistent with the texture observed in SK4A, where orthopyroxene mantles garnet (see Figure 2.11).

2.6.3 Retrograde metamorphic evolution

The large volumes of melt lost from the Steynskraal granulites means that they remained essentially inert for the most of the retrograde evolution and the subsolidus retrograde *P-T* path is largely obscured. Nevertheless, it is still possible to glean some information about the high-temperature suprasolidus portion of the retrograde path from observed textures developed in both the metapelites and metagreywackes. The peak pseudosections for SK9-CLM and SK6C and SK4A are appropriate for constraining the initial suprasolidus retrograde evolution.

Two potential *P-T* paths accommodating both the prograde *P-T* trajectory and minimum peak assemblage for SK6C and SK9-CLM are demonstrated in Figure 2.38a and b, respectively. Path 1 for both SK6C and SK9-CLM represents a potential *P-T* path to hypothetical maximum *P-T* conditions by extrapolation of the prograde path to intersect a suprasolidus retrograde path oriented in *P-T* space such that the minimum peak phase assemblage is reproduced above the solidus (black circle). Given a prograde trajectory from 6.5 to 7.5 kbar and 700 to 850 °C, the stability of cordierite in the peak assemblage of SK6C and SK9-CLM suggests the suprasolidus *P-T* evolution following attainment of potential maximum peak conditions could not have involved an increase in pressure, i.e., the retrograde path must have been decompressive and dominated by cooling. The absence of orthopyroxene in the peak assemblage suggests suprasolidus decompression following attainment of maximum peak conditions did not occur at pressures below 7 kbar. Given the highly restitic nature of SK6C and SK9-CLM bulk compositions (78 and 82 % melt loss, Section 2.6.2), the absence of M_1 coronas around garnet suggests that *P-T* path 1 is unlikely (Section 2.6.1), i.e., the actual *P-T* path did not proceed to significantly higher *P-T* conditions than those indicated by the preserved minimum peak assemblage in SK6C and SK9-CLM at present (Section 2.6.1). Thus, a more likely *P-T* path accommodating the absence of M_1 corona textures around garnet is *P-T* path 2 (Figure 2.38a, b).

The retrograde evolution of SK4A is demonstrated in Figure 2.39. SK4A is a useful sample, since its proximity to SK6C means that any difference in minimum peak *P-T* conditions inferred from pseudosections reflects varying capacity of bulk compositions to preserve the peak assemblage owing to back-reaction with the melt,

rather than actual differences in peak conditions (Section 2.6.1). SK4A has undergone a greater degree of retrograde re-equilibration compared to SK6C and SK9-CLM, since the solidus in SK4A is depressed (owing to the presence of retained melt) by 15 - 20 °C at 7 - 7.5 kbar compared to the metapelitic solidus at the same pressure. Retrograde biotite mantles both garnet and orthopyroxene in SK4A (Figure 2.11). Figure 2.39 is a pseudosection for SK4A peak conditions, onto which minimum peak conditions inferred from SK6C and SK9-CLM are superimposed. The solid black line is the prograde path inferred from reaction textures and inclusions in garnet from SK6C and SK9-CLM. The dot-dash line represents a potential retrograde path involving decompression from minimum peak pressures attained in SK6C to minimum peak conditions preserved in SK4A (7.1 kbar, 858 °C). Biotite mantling orthopyroxene and garnet grows once the biotite-in line is crossed (solid square). The coarse-grained evolution of SK4A ends as the solidus is crossed (green circle).

Stevens et al. (1997b) described a retrograde reaction texture where peak-metamorphic cordierite reacts with melt to form an aggregate of biotite, sillimanite and quartz. This is the texture shown in Figures 2.7 and 2.9. According to them, the biotite-sillimanite intergrowth was subsequently overgrown during post-shock metamorphism by cryptocrystalline spinel and orthopyroxene. In addition, they suggested that, apart from the post-impact replacement of garnet, there is no other evidence to suggest pressure-dependent breakdown of garnet and, as such, the pre-impact retrograde M_1 *P-T* path was inferred by them to have been isobaric. Based on the observation of coarse-grained prograde sillimanite included in garnet and attendant phase equilibria modelling of the prograde path presented in this chapter, it is more likely that relict sillimanite was included within cordierite and biotite seams on the prograde path. The sillimanite was then pseudomorphed by fine-grained spinel and cordierite aggregates following the impact event (Sections 4.2.6, 4.3.6). The inclusion of sillimanite within cordierite along a prograde path has been described for metapelites previously (Boger and White, 2003) and the lack of pressure-sensitive garnet breakdown in the stromatic migmatites is in accord with large volumes of melt loss revealed by the melt reintegration modelling, such that these rocks become chemically inert.

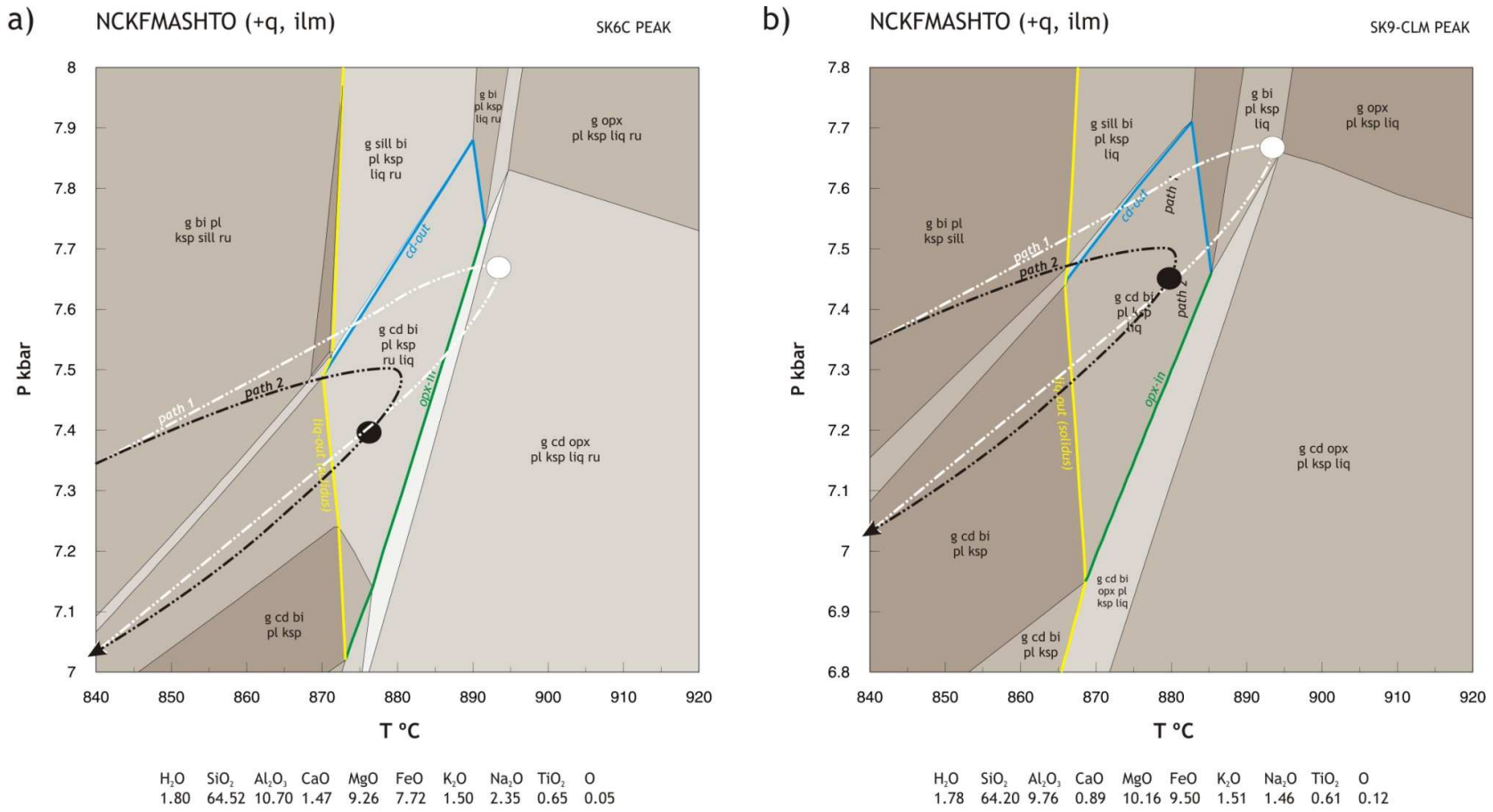

Figure 2.38: Supra-solidus retrograde P-T evolution derived from peak pseudosections for (a) SK6C and (b) SK9-CLM. The cordierite-out line for both SK6C and SK9-CLM is blue and the orthopyroxene-in line is green. Minimum peak conditions are indicated by the black circles and potential maximum peak conditions based on topological constraints discussed in the text are indicated by the white circles. The initial prograde trajectory for both path 1 and 2 is constrained from protolith pseudosections and inclusion relationships in garnet and cordierite. A possible P-T path to potential maximum conditions accommodating both the prograde trajectory and minimum peak assemblage is represented by the white hatched line (path 1). Another P-T path to minimum peak conditions is delineated by the black hatched line path 2.

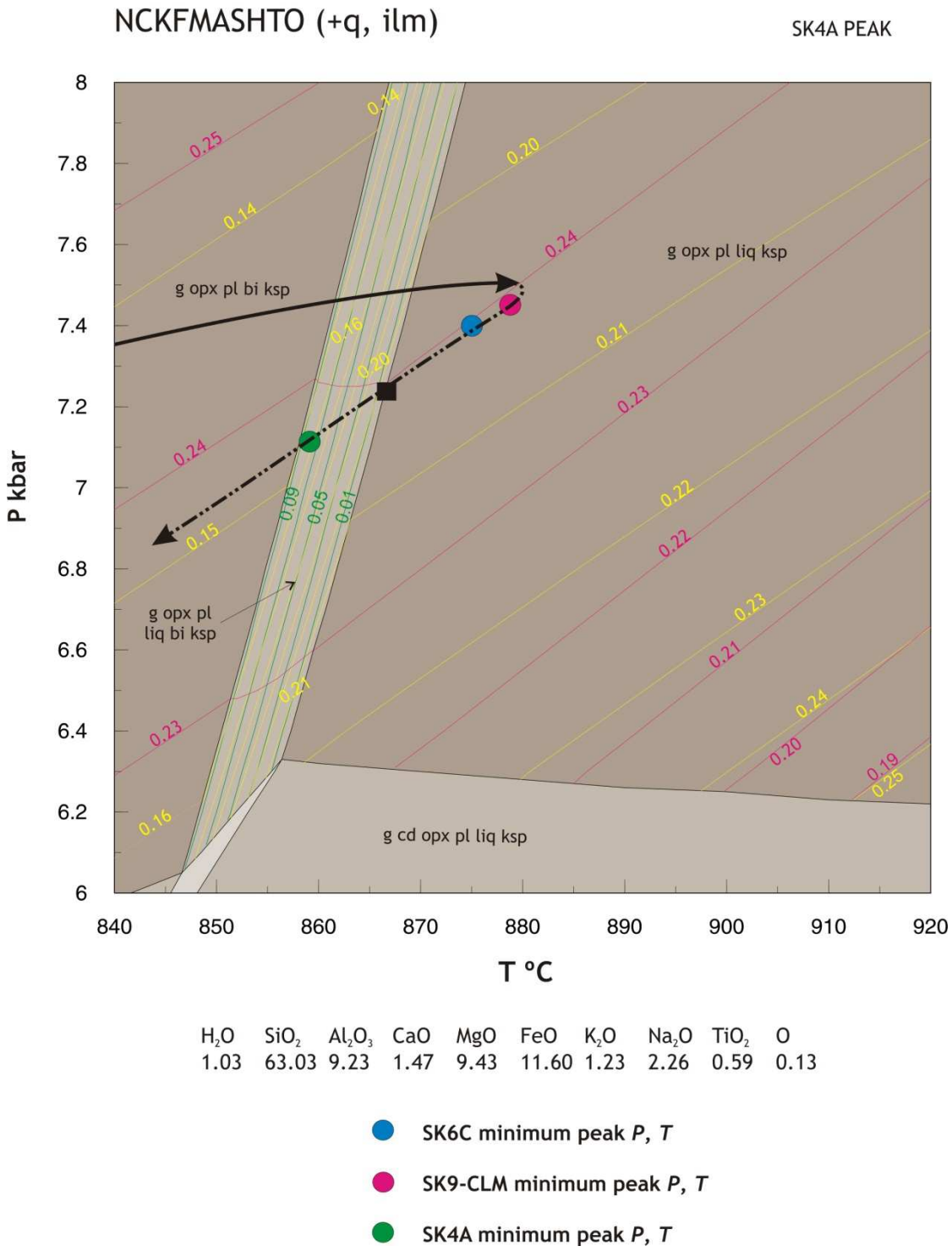

Figure 2.39: P-T pseudosection constructed for SK4A peak metamorphic conditions, contoured for mineral modes of garnet (red), biotite (green) and orthopyroxene (yellow), with superimposed peak conditions and proposed P-T path. The black square indicates the region in P-T space where P-T path crosses the biotite-in line. The green circle represents the P-T conditions where the P-T path crosses the solidus and the peak assemblage is preserved.

2.7 Discussion

Recent structural and geochronological data from the Vredefort Dome (Hart et al., 1999; Lana et al., 2006; Armstrong et al., 2006) has led to a reappraisal of the tectonic and metamorphic history of the Archaean Basement Complex rocks exposed in the core of the Dome. Archaean ages for peak metamorphism of 3.10 - 3.08 Ga (Armstrong et al., 2006) and 3.107 Ga (Hart et al., 1999), conclusively ruled out the possibility that the high-grade event was related to intraplating of magmas at 2.06 Ga, as suggested by Stevens et al. (1997b). Similarly, Schreyer's endogenic model (Schreyer, 1983) and Perchuk's (2002) model seeking to relate the M1 event to Dome formation at 2.02 Ga are no longer tenable.

An alternative heat source for the peak event needed to be coupled with a tectonic model which allowed exhumation of granulites in 10 - 25 Myr to within 12 km of surface upon which the Dominion lavas were extruded at 3.074 Ga. Lana et al. (2004, 2006) proposed a tectonic model for the evolution of the Archaean Basement Complex of the Vredefort Dome based on geochemical, geochronological and structural data from the core of the Dome. They favoured a model involving tectonomagmatic thickening of the crust during easterly- to northeasterly-directed subduction of an oceanic slab beneath the Kaapvaal craton between 3.12 Ga and 3.08 Ga (Armstrong et al., 2006; Lana et al., 2003a; Lana et al., 2006). At the time Lana et al. (2006) proposed their model, an anticlockwise path (Stevens et al., 1997b) was favoured for the metamorphic evolution of the Steynskraal metapelites. Lana et al. (2006) suggested that the pressure increase on the anticlockwise prograde path might be explained by considering the Steynskraal rocks as greenstone xenoliths sinking through a molten mush of TTG magmas. However, their model struggled to accommodate an isobaric cooling retrograde path, proposed by Stevens et al. (1997b) on the basis of an apparent lack of garnet breakdown and the apparent replacement of cordierite by sillimanite and biotite. An isobaric cooling path, in contrast to isothermal decompression paths more typical of orogenic terranes, indicated that the crust could not have been significantly overthickened (Lana et al., 2006). Without overthickened crust these workers could not easily explain the rapid exhumation rates required during extensional unroofing implied by age data. An alternative *P-T* path was proposed by Perchuk et al. (2002) in which a post-peak

(700 °C, 5 kbar) decompressive cooling path was proposed (Figure 2.40) based on zonation of peak phases. This would complement Lana's model better, unfortunately the zonation documented by Perchuk et al. (2002) could not be verified in this study – any zonation is related to M_3 symplectite formation (Section 2.5) and not post-M_1 decompression.

In this chapter, the M_1 event is revisited, employing quantitative phase equilibria modelling capacity in THERMOCALC to re-evaluate the metamorphic textures, bringing congruence between structural, geochronological and metamorphic models for the Archaean Basement Complex in the Vredefort Dome.

2.7.1 Towards a new model

Conventional thermobarometry applied by both Schreyer and Abraham (1978) and Perchuk et al. (2002) led to peak *P* and *T* estimates of 5 kbar at 700 °C in both studies, whereas Stevens et al. (1997b) suggested temperatures ranged from between 850 °C to > 920 °C at 5 kbar. Based on inclusion relationships in garnet, Stevens et al. (1997b) constrained an anti-clockwise *P-T* path for the M_1 event characterized by post-peak isobaric cooling. Perchuk et al. (2002) deduced a weakly decompressive cooling path based on zonation in Archaean phases. The three alternative metamorphic scenarios are illustrated in Figure 2.40. A problem common to all three estimates, and an issue that typically compromises the application of conventional thermobarometry in metamorphic studies, is the retrograde compositional resetting of Fe-Mg thermometers on cooling. This commonly leads to an underestimation of peak conditions. A more pressing problem, however, is the large uncertainties intrinsic to *P-T* estimates derived from conventional thermobarometers. Uncertainties in conventional thermobarometry arise due to error in the probe analyses, uncertainties in the thermodynamic dataset and *a-x* relationships between mineral end-members, particularly when ferric iron is present. If uncertainties are not quantified realistically, the estimated *P-T* conditions that they constrain can be very misleading (e.g., Powell and Holland, 2008). In contrast, in pseudosections, the boundaries between fields of alternative mineral assemblages constrain *P* and *T*, and not uncertainties (Powell and Holland, 2008). Pseudosections also allow

reconstruction of the *P-T* path through comparison of the observed assemblage with corresponding mineral modes and compositions in assemblages that could have developed given a range of potential *P-T* conditions in the pseudosection. Most importantly, however, unlike conventional thermobarometers, pseudosections are able to constrain *P-T* conditions of formation for an assemblage without requiring knowledge of the original peak mineral compositions. This is particularly useful in complex, polymetamorphic terranes that are susceptible to diffusional resetting of components in phases, as is the case in the Vredefort Dome granulites.

Phase equilibria modelling of metapelitic and metagreywacke garnet granulites from the Steynskraal traverse constrains new minimum peak conditions of 870 - 885 ºC and 7.1 - 7.7 kbar during the 3.10 – 3.08 Ga M_1 Archaean metamorphic event in the core of the Vredefort Dome (Figure 2.40). Actual peak conditions may have been marginally higher, but no longer manifest in the rock since the coarse-grained suprasolidus evolution of granulites probably continued after peak conditions were attained, such that the assemblage observed in the rock at present reflects the final equilibrium assemblage attained upon freezing at the solidus. The absence of evidence for corona formation related to M_1 suprasolidus retrogression in melt-depleted SK6C and SK9-CLM suggests actual peak conditions were not significantly higher than the minimum peak estimates obtained from the assemblage in the rock at present. Previous thermobarometric estimates using conventional thermobarometers appear to have underestimated peak *P* conditions owing to compositional re-equilibration of minerals to lower temperatures and pressures during the high-temperature part of the retrograde history, and underestimation of the extent of post-impact re-equilibration. Inclusion relationships in garnet and cordierite constrain a prograde up-pressure trajectory dominated by heating from 6.5 kbar, 700 °C to 7.5 kbar, 850 °C (Figure 2.40). The absence of cordierite in the metagreywackes and orthopyroxene in the pelitic peak assemblages suggests a suprasolidus retrograde path dominated initially by cooling through the pelitic solidi and then minor decompression to > 7 kbar at ~ 858 °C prior to cessation of the coarse-grained evolution of the melt-rich metagreywacke, SK4A, as the solidus is crossed (Figure 2.40). Thereafter no retrograde textural information is recorded in the rocks.

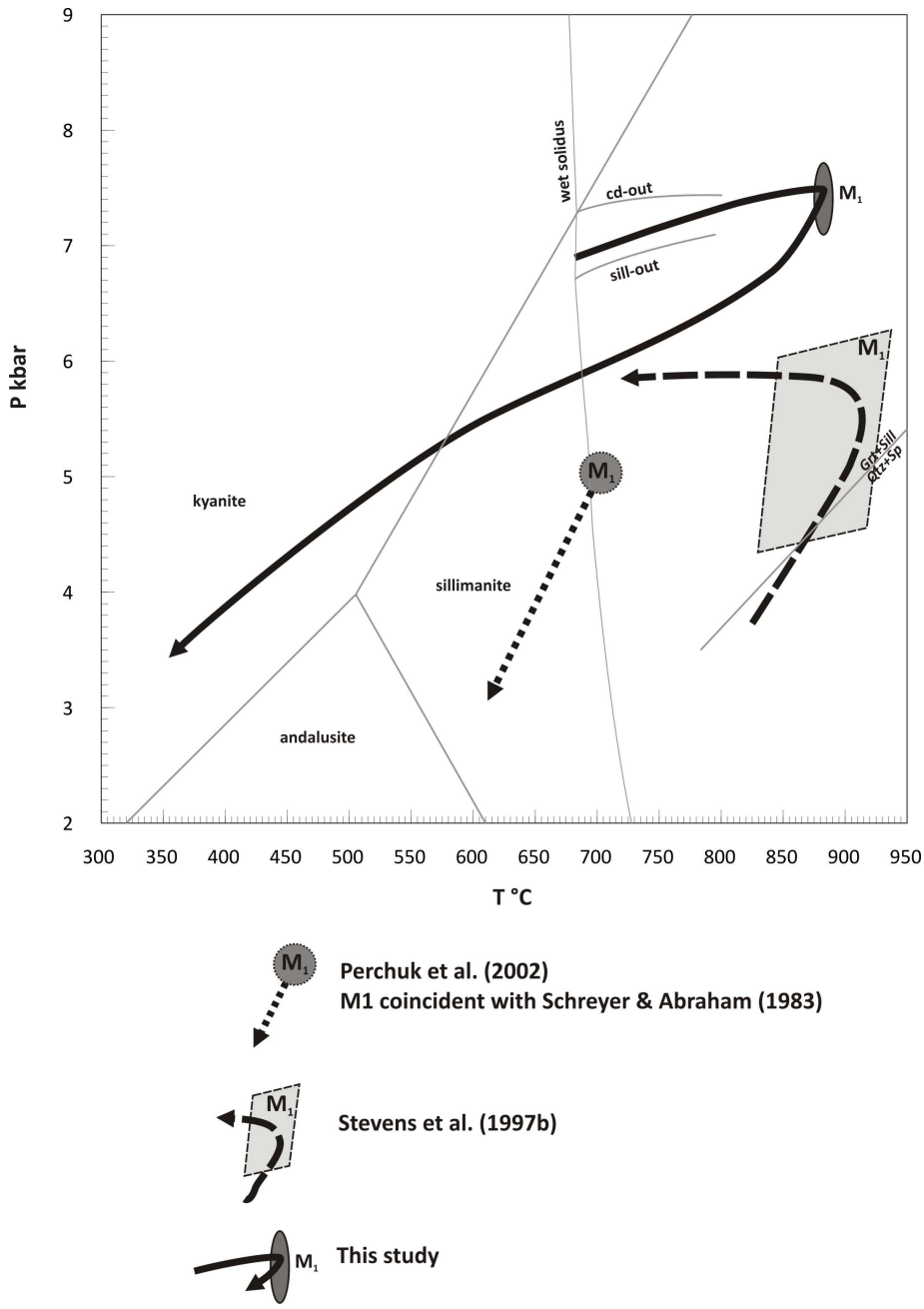

Figure 2.40: Comparison of P-T estimates from previous studies and those attained in this study. The steeper subsolidus retrograde path corresponds to estimates of the burial depth of the Steynskraal rocks at 3.074 Ga.

Phase equilibria constraints on the prograde and suprasolidus retrograde evolution suggest a clockwise *P-T* path for the Archaean granulite event. This is consistent with field and structural evidence from the enclosing TTG rocks (Lana et al., 2006; Armstrong et al., 2006). The prograde pressure increase from 6.5 kbar, 700 ºC to 7.5 kbar, 850 ºC could potentially still be accommodated by denser greenstone xenoliths

gravitationally sinking within molten crust dominated by cooling semi-crystalline TTG magmas, however, such a scenario has implications for crustal rheology that cannot be easily tested. The path is more likely to be the product of more conventional burial during D_3 tectonic thickening with a component of magmatic thickening caused by TTG intrusions at shallower crustal levels leading to overthickening of the crust and subsequent exhumation. The latter model has the advantage of not requiring a potentially gravitationally unstable situation in which the crust is molten enough to allow xenolith subsidence. Furthermore, the rapid, extensional collapse of the thickened crust to expose the amphibolite facies rocks at surface within 10 - 25 Ma after the peak event to form the substrate upon which the Dominion lavas were extruded is more readily reconciled with a clockwise *P-T* path, although such extension may have only commenced after an initial phase of cooling (Figure 2.40). The > 500m-wide northeast-trending, mylonitic Broodkop shear zone in the south-east of the Dome (Figure 1.5; Lana et al., 2006; Armstrong et al., 2006), which now juxtaposes upper amphibolite facies gneisses against mid-greenschist facies greenstones, supports this retrograde evolution.

The new *P-T* path presented here and the tectonic model of Lana et al. (2006) are in accord with tectonic models of subduction-driven tectonics inferred from low geothermal gradients (12 - 15 °C/km) determined from recent work on the Barberton greenstone belt at ca. 3.23 Ga (Moyen et al., 2006; Dziggel et al., 2002; Diener et al., 2005, 2006). These workers invoke a similar clockwise *P-T* path during accretion of two island-arc terranes during the main, D2 phase of collisional tectonics at 3.23 Ga in an arc-trench setting (Moyen, 2006). However, the Barberton terrane is characterised by much lower peak temperatures and higher pressures than the rocks in the Vredefort terrane. Peak conditions for the Onverwacht Group were constrained at 8 - 11 kbar and 650 - 700 °C (Dziggel et al., 2002). In the southern Barberton greenstone belt, work by Diener et al. (2005, 2006) yielded peak estimates of 9 - 12 kbar and 650 - 700 °C. Moyen et al. (2006) characterised still higher *P, T* conditions of 12 - 15 kbar and 600 - 650 °C for an amphibolite from the Inyoni shear zone. The higher peak temperatures and lower pressures determined for the Steynskraal rocks suggest a greater component of magmatic heating than in the Barberton terrane, in agreement with voluminous TTG magmatism coincident with D_3 deformation in the Vredefort Dome.